Production and Characterization of Novel Nanostructure Materials

by

Olivier L. GUISE

B.S. in Chemistry and B.S. in Chemical Engineering,
Ecole Supérieure de Chimie Physique Electronique de Lyon – France - 1999

Submitted to the Graduate Faculty of

Arts and Sciences in partial fulfillment

of the requirements for the degree of

Doctor of Philosophy

University of Pittsburgh

2005

UNIVERSITY OF PITTSBURGH

FACULTY OF ARTS AND SCIENCES

This dissertation was presented

by

Olivier GUISE

It was defended on

04-18-2005

and approved by

Prof. Stéphane Petoud

Prof. Gilbert Walker

Prof. Jeremy Levy

Prof. John T. Yates, Jr.
Dissertation Director

ABSTRACT

Production and Characterization of Novel Nanostructure Materials

Olivier GUISE, PhD

University of Pittsburgh, 2005

The research presented here was conducted in the Department of Chemistry at the University of Pittsburgh, in the Surface Science Center, under the supervision of Prof. John T. Yates, Jr. The work described can be divided into two main parts.

As the size of materials decreases, they experience confinement. The electronic properties of materials are strongly correlated to the confinement experienced by the material or device being studied. New tools and experimental techniques need to be developed in order to probe the properties of such objects at sub-micrometer scales in a non-interfering way. The development of such an instrument and its usefulness in measuring electronic properties of confined objects is the topic of the first part of this dissertation, covering sections 1, 5 and 6. The Nanoworkbench is a unique multiple-probe instrument operating under ultrahigh vacuum conditions. It combines a molecular-beam epitaxy chamber for nucleation of quantum dots or the growth of thin films, a preparation and analysis chamber equipped with standard surface science tools such as Auger electron spectroscopy, X-ray photoelectron spectroscopy and mass spectrometry. The core of the system is the multiple-probe STM chamber combined with a scanning electron microscope, allowing precise controlled motion of the probes and the realization of sub-micrometer scale four-point probe measurements. This instrument was fully conceived, designed and assembled in the Department of Chemistry, at the University of

Pittsburgh. The application of the Nanoworkbench to sub-micrometer four-point probe conductivity measurements and the formation of a roaming field-effect transistor on a silicon-on-insulator surface is demonstrated in section 5. Additionally the Nanoworkbench was used to electrically sense the normal motion of the interface between a metal (Al(111)) and its oxide coating, and a semiconductor (Si(100)) during oxidation, finding that Al(111) oxidizes in conformance with the Mott-Cabrera model. Here Al^{3+} ions move away from the Al/Al_2O_3 interface to the outer Al_2O_3 surface when oxide film growth occurs. In contrast, oxygen penetration into covalent Si(100) occurs during oxide film formation.

The second part of this dissertation – sections 7 to 10 – deals with the formation of dense arrays of sub-10nm Ge islands on Si(100). Upon deposition of Ge on Si(100), Ge islands are randomly nucleated on the surface by self-assembly after the formation of a wetting layer, whose thickness depends on the experimental conditions. These islands have rather large diameters and a broad size distribution and are therefore not suitable for application in quantum computing architecture for instance. The object of this study is the formation of arrays of Ge islands with control over both the island diameter (10nm, ± 2nm) and the islands spacing (as small as 35nm, ± 1nm). We will show that the pre-adsorption of small islands of carbon on Si(100) and their thermal conversion to SiC leads to the formation of Ge islands that are smaller than Ge islands nucleated on a clean Si(100) substrate. We can use this carbon effect" by creating a carbon template on the Si(100) surface by electron-beam-induced deposition. These carbon deposits transform into SiC after annealing under UHV conditions. Upon subsequent Ge deposition, ultra-small Ge islands will nucleate by directed self-assembly on the surface in perfect registry with the carbon template.

Conceptual ideas will be provided as a background for the research described in sections 5 to 10. These conceptual ideas include a description of the four-point probe measurement technique, the framework of the Mott-Cabrera theory for oxide film growth on metal surfaces, a description of heteroepitaxy, and finally the description of the formation of Ge islands in Si/Ge and Si/C/Ge system along with the attempts at ordering these islands.

TABLE OF CONTENTS

LIST OF TABLES

LIST OF FIGURES

PREFACE

First of all, I would like to thank Professor John T. Yates, Jr., Director of the Surface Science Center at the University of Pittsburgh for having me in his research group. His dedication, thorough knowledge of science, pedagogy and integrity has been a constant source of inspiration and motivation.

This work would not have been possible without the input, energy and enthusiasm of Professor Joachim Ahner. His contribution to the first years of the Nanoworkbench was very important.

Professor Jeremy Levy from the Department of Physics and Astronomy at the University of Pittsburgh was involved with both the Nanoworkbench project and the Ge islands project. I would like to express my gratitude for his contribution to the success of both projects.

Moon-Chul Jung and Dr. Hubertus Marbach also contributed to the Nanoworkbench project. I would like to thank them here.

The machine shop and electronic shop from the Department of Chemistry played an important role. I am very grateful for their help and I feel very indebted in particular to Mr. Thomas Gasmire for his wonderful craftsmanship and friendship.

All the people working with me in this group contributed to create a motivating working and friendly atmosphere.

Last but not least, I would like to acknowledge the constant moral support provided by my parents, my sister Agnès, and my wife Estelle.

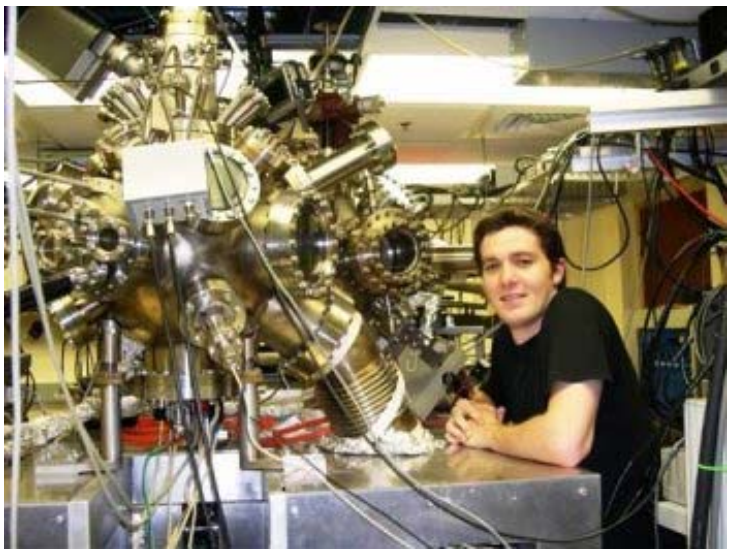

Oft, wenn es erst durch Jahre durchgedrungen
Erscheint es in Vollendeter Gestalt
Was glänzt, ist für den Augenblick geboren
Das Echte bleibt der Nachwelt unverloren.

Often, after years of perseverance,
It emerges in a completed form.
What glitters is born for the moment
The genuine lives on to the afterworld

(Faust, Vorspiel aus demTheater)

1. Four-Point Probe Measurements

1.1. Four-Point Probe

In order to study the electrical resistivity of confined structures or sub-micrometer scale devices, new instruments are needed that can precisely and selectively address these structures to probe their specific contributions in a non-interfering way.

1.1.1. Four-Point Probe Background

We can distinguish two main techniques used to perform conductivity measurements on samples: macroscopic-scale measurements using four contacts in UHV[1,2] or ex-situ[3,4] and microscopic or sub-micrometer-scale measurements using lithographically patterned electrodes on the substrate[5]. Millimeter and micrometer scale arrays of electrodes have been used for a long time by the microelectronics industry for fast automated testing of microelectronic devices. These probes systems are not necessarily intended for four-point measurements and are designed to match a particular device geometry[6]. The electrode spacing on such electrodes arrays is typically larger than 100μm. Recently, a micrometer scale in-situ four-point probe apparatus has been designed[7]. The spacing achieved of less than 10μm marks a strong improvement but the four probes are still dependent from each other (i.e. all four probes are physically connected to each other) and only pre-determined configurations are accessible, depending on the probe array geometry.

The real question behind this type of measurement is the following: how can one make accurate measurements and ensure good electrical contacts to surfaces? Using permanent

contacts on the surface before transfer to UHV can rapidly become a problem since one typically needs to anneal a sample to high temperatures to prepare a clean surface. Contamination problems might then arise from the permanent contacts. It is then obvious that the contacts need to be performed after UHV processing and cleaning of the sample. But as can be seen on the schematic of Figure 1-1, the spacing between the probes determines the depth of sensitivity of the measurement, i.e. at larger probe spacing, the contribution of the surface will be diluted by the contribution of the bulk. When the spacing between the probes is larger, the current penetrates deeper in the crystal[8]. One needs to space the probes as closely as possible to really measure intrinsic properties of surface conductivity. So far mostly systems with millimeter or sub-millimeter spacing have been performed. The surface sensitivity of such measurements would increase dramatically with reduced probe spacing to micrometer or sub-micrometer levels. Besides, independent motion of the probes would allow various types of four-point measurements to be performed, with various configurations.

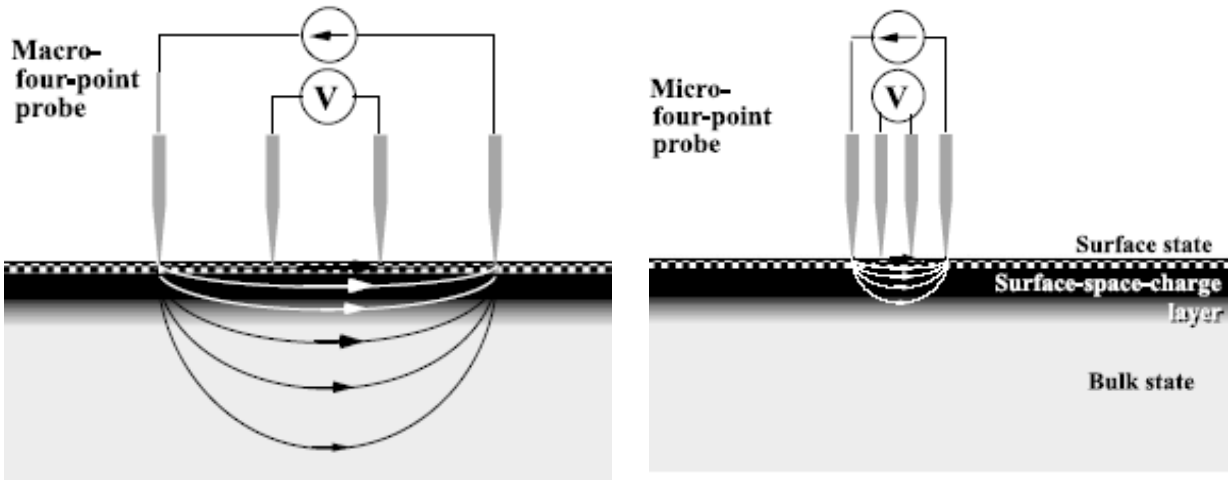

Figure 1-1: Schematic of collinear four-point probe measurement showing the importance of probes spacing. The spacing of the probes determines the depth of sensitivity of the measurement: the smaller the spacing between the probes, the smaller the contribution of the bulk to the measurement. When the spacing between the probes is larger, the current penetrates deeper in the crystal[8].

1.1.2. Theory – two probes vs. four probes

Unlike general-purpose measurements and I-V curve generation on macro- and micro-scale components and materials, measurements on sub-micrometer-scale devices require special care and techniques. General-purpose resistance measurements and I-V curve generation are often performed using a two-point electrical measurement technique. However, when the resistance to be measured is relatively low or when the resistance of the probes or the contacts is relatively high, a four-point probe is necessary to measure resistance accurately.

In order to determine a resistance, Ohm's law is used: R=V/I. A known current is sourced and flows through the unknown resistance. The voltage that develops across the resistance is measured and then the resistance is determined by dividing the measured voltage by the source current. A problem that occurs when using a two-probe setup is that the voltage is measured not only across the resistance in question, but includes the resistance of the leads as well, as shown schematically in Figure 1-2. When using an ohmmeter to measure resistances greater than a few ohms, this added resistance is usually not a problem. However, when measuring low resistances on sub-micrometer-scale materials or devices, or when contact resistance may be high, obtaining accurate results with a two-probe measurement may be a problem.

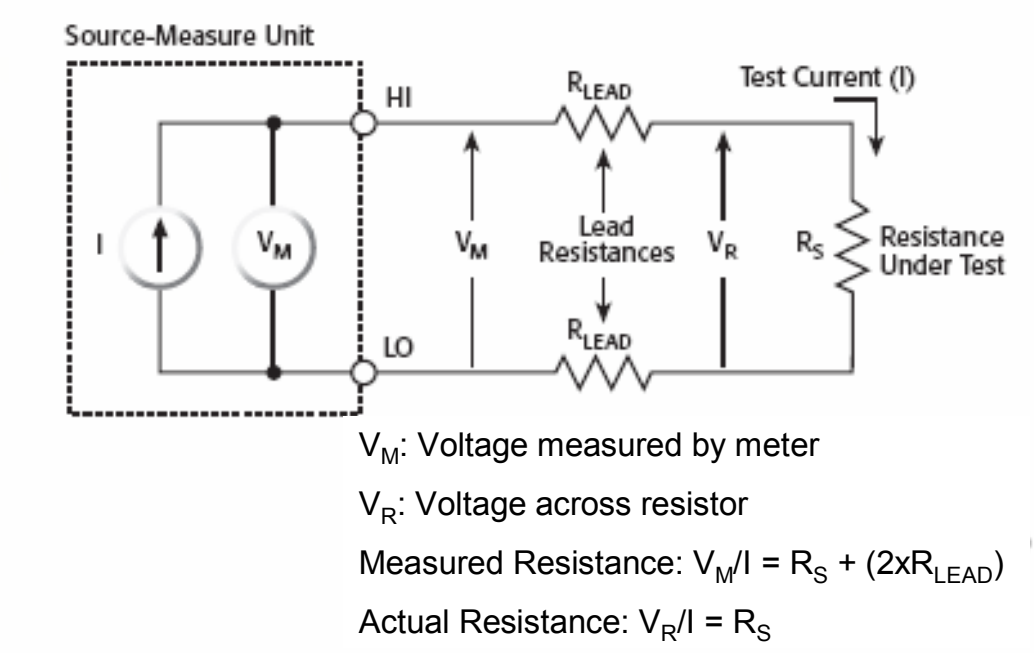

Figure 1-2: Two-Probe Measurement

A solution to the problem of two-probe measurements that measure the lead and contact resistance along with that of the device under test is the four-probe measurement. In this type of measurement, a second set of probes is used for sensing. Negligible current flows in these probes (a very high impedance voltmeter is used); therefore only the voltage drop across the device is measured as is shown schematically in Figure 1-3. As a result, resistance measurement is more accurate.

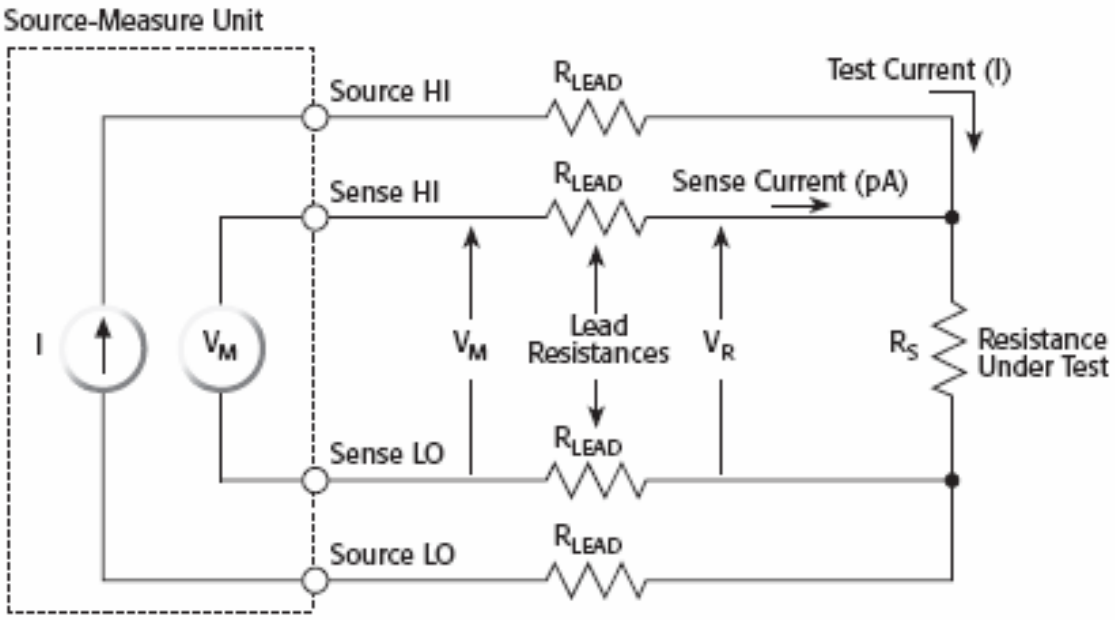

V_M: Voltage measured by meter

V_R: Voltage across resistor

Because sense current is negligible: $V_M = V_R$

And Measured Resistance: $V_M/I = V_R/I$

Figure 1-3: Four-Point Measurement

1.1.3. Collinear Probe Method

The most common way of measuring the resistivity of a material or device is by using a four-point collinear probe system as shown in Figure 1-4. This technique involves bringing four probes in contact with a material or device of unknown resistance.

The two outer probes are used for sourcing current and the two inner probes are used for measuring the resulting voltage drop across the surface of the sample. The volume resistivity is calculated as follows (see schematic in Figure 1-4):

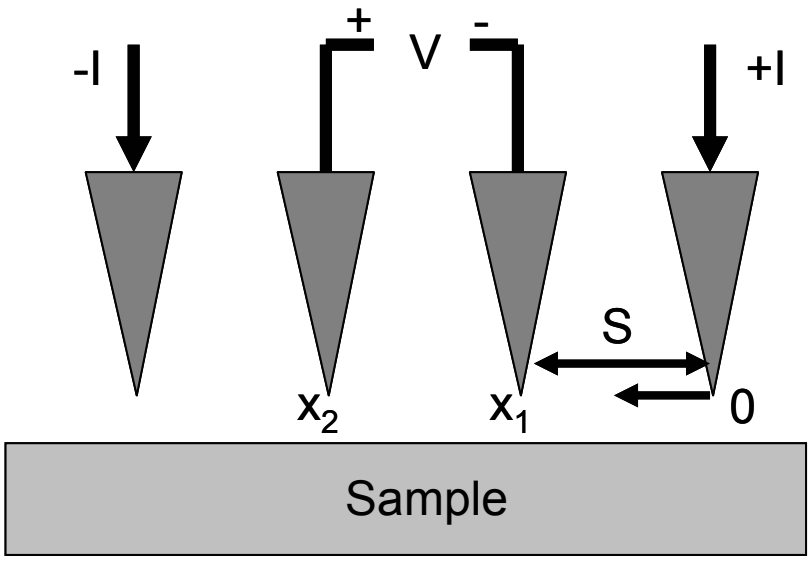

Figure 1-4: Schematic of four-point probe configuration for calculation of the resistivity.

For the derivations, we assume that the tip is infinite and that the sample is semi-infinite in lateral dimension. When the sample thickness t is much greater than the probe spacing s, one can assume a spherical protrusion of current emanating from the outer probes (see Figure 1-5). The expression for the electric field along the line of the probes is:

$$E(x) = \rho I\left(\frac{1}{2\pi x^2} - \frac{1}{2\pi(3s-x)^2}\right), \qquad \textbf{1-1}$$

In this equation, $2\pi x^2$ corresponds to the surface area of a half sphere since we assume a spherical protrusion of current emanating from the outer probes as shown in Figure 1-5 (left).

The voltage being measured between the inner probes, the integration has to be carried out between s and 2s and thus after integration:

$$V = \frac{\rho I}{2\pi}\frac{1}{s} \qquad \textbf{1-2}$$

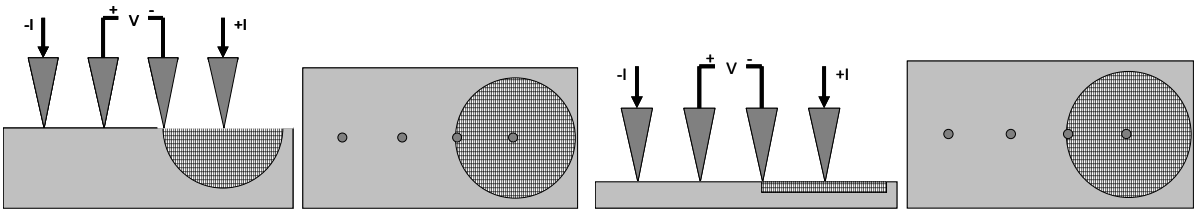

Figure 1-5: Schematic of the path of current lines for the two domains. Left two images: the thickness t of the sample is much larger than the separation between the probes. We assume a spherical protrusion for the current emanating from the outer probes. Right two images: the thickness t of the sample is much lower than the separation between the probes. We assume a ring-like protrusion of the current emanating from the outer probes.

And therefore:

$$\rho = 2\pi s\left(\frac{V}{I}\right) \qquad \textbf{1-3}$$

where: ρ = volume resistivity (Ω.cm)

V = measured voltage (V)

I = source current (A)

s = probe spacing (cm)

For a very thin layer (thickness t < < spacing s between the probes), the assumption of a spherical protrusion of current emanating from the outer probes no longer holds. Instead, because of the thinness of the layer, one can assume current rings instead of spheres (see Figure 1-5 right). Therefore the expression for the area A becomes $A=2\pi xt$, where t is the thickness of the layer and $2\pi x$ defines the perimeter of the current ring.

$$E(x) = \rho I\left(\frac{1}{2\pi xt} - \frac{1}{2\pi(3s - x)t}\right) \qquad \textbf{1-4}$$

And therefore, after integration between s and 2s:

$$V = \frac{\rho I}{\pi t} \ln 2 \qquad \textbf{1-5}$$

And finally:

$$\rho = \frac{\pi t}{\ln 2}\left(\frac{V}{I}\right) \qquad \textbf{1-6}$$

where: ρ = volume resistivity (Ω.cm)

V = measured voltage (V)

I = source current (A)

t = film thickness (cm)

2. Mott-Cabrera Theory related to Interface Growth

2.1. Introduction

The study of the oxidation of metals is a very important topic, and has been extensively studied theoretically and experimentally. The initial oxidation to produce an atomically thin oxide film is the first step for heavy oxide film formation in the atmosphere.

The processes that occur when a clean metal surface is exposed to oxygen can be summarized as follows:

1. Oxygen is adsorbed on the clean metal surface to form a chemisorbed layer of monolayer thickness.
2. At the very early stages, oxygen islands typically nucleate on the surface, and the chemisorbed layer converts to an oxide compound layer.
3. Further growth of the oxide layer takes place. As we will see, the kinetics of oxidation will depend on how atom transport occurs.

The kinetics for the first two steps usually follows a growth law with first-order dependence on time while the third process was described by Mott and Cabrera to be non-linear in time, and is the topic of the Mott-Cabrera theory related to oxide interface growth on a metal surface.

Oxygen adsorbed on a metal or on a stable oxide surface at room temperature converts to several sub-species. On the oxide surface, both neutral O_2 and O as well as ionic species O^- and O^{2-} may exist, alone or in equilibrium with one another[9].

2.2. The Mott-Cabrera Theory for Oxide Film Growth on Metals

The first theory of the growth rate of the oxidation of metals was devised by Mott and Cabrera in 1949 [10]. Since then this theory has been experimentally tested and theoretically modified or adapted. One can distinguish two domains:

- Thin oxide film – low temperature regime
- Thick oxide film – high temperature regime

As described by Roberts[11], there are two limiting cases during oxide growth as shown in Figure 2-1. These two growth modes would be expected for metal oxidation or for non-metal oxidation, respectively.

1. Positively charged cations and electrons migrate in the same direction from the metal-oxide interface to the outer surface (metal oxidation);
2. Negatively charged anions migrate inwards and electron movement occurs in the opposite direction (non-metal oxidation).

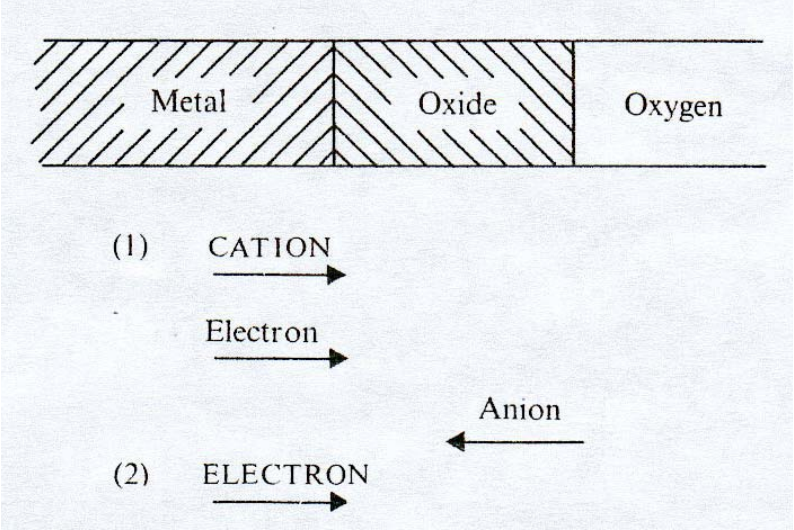

Figure 2-1: Model of oxide growth[11]

2.2.1. Thin Film – Low Temperature Regime

This is not the scope of this dissertation to reproduce in detail the calculation of the Mott-Cabrera theory. Instead I will present the conceptual framework of their theory and its application range.

Experimentally, it was observed that all metals behave in a similar way for low temperature oxidation: when exposed to oxygen they show an initial very rapid oxide film growth, followed by a strong slow down and at some critical oxide thickness the growth nearly completely stops. This was observed for copper, for aluminum and for silver by Cabrera et al.[12,13]. The following assumptions were made by Mott and Cabrera:

- The first monolayer of oxide is formed on the metal. The layer is assumed to consist of atomic oxygen. It is also assumed that electrons can pass through the oxide layer from the metal to oxygen molecules arriving at the outer surface of the growing oxide film by

some mechanism. Finally it is assumed that the electronic motion is rapid compared with the ionic motion across the oxide film.

- The slow step in oxide growth is at the metal-oxide interface and involves entry of the metal 'ion' from the metal into the oxide lattice (See Figure 2-1, first mechanism). There are N special sites at this interface and their vibrational frequency is υ. The barrier to entry, W, is the activation energy of the oxidation process.
- Oxygen molecules from the gas phase dissociate at the oxide surface giving rise to chemisorbed oxygen adatoms. These adatoms become negatively charged, leading to a surface potential V across the oxide thickness X. Consequently, a field F=V/X is created across the oxide.
- The field F lowers the barrier W to a value W-qaF/2, where q is the charge of the ion and a/2 is the jump distance for the metal ion, a being the interatomic spacing. Figure 2-2 shows the lowering of the energy barrier as a function of the oxide thickness.

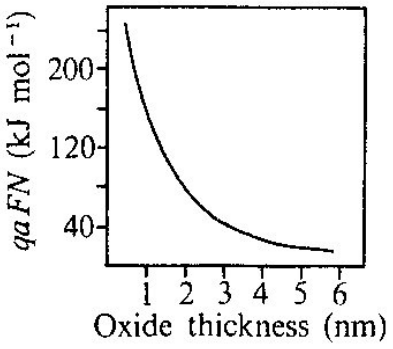

Figure 2-2: The field effect as a function of thickness. N is the Avogadro constant[11]. N.B.: it should be noted that the author incorrectly stated the ordinate qaFN in kJ.mol^{-1}. Instead the ordinate qaFN should be in J.mol^{-1}.

The growth rate has the form[9,10]:

$$\frac{dX}{dt} = N \cdot \Omega \cdot \upsilon \cdot \exp\left\{-\frac{W - q \cdot a \cdot V/2X}{RT}\right\} \qquad \textbf{2-1}$$

where:

N	=	number of mobile metal ions per unit surface area
Ω	=	volume of oxide per metal ion
ν	=	phonon frequency

which leads after integration[9] to:

$$\frac{1}{X} = A^* - B^* \ln t \qquad \textbf{2-2}$$

which is an inverse logarithmic law.

Details of the mathematics connecting equation 2-1 and to equation 2-2 are provided in Appendix. A.5.

It should be mentioned that many models have been extracted from modifications of this law to fit experimental observations. For instance, Fehlner and Mott found that the activation energy (W - qaF/2) is better described as (W - qaF/2 + βX) where βX reflects a structural change in the oxide film during growth[14].

2.2.2. Thick Film – High Temperature Regime

In the high temperature regime, the evolution of the thickness of the oxide interface film can no longer be described by the inverse logarithmic law. The assumptions from Mott and Cabrera for this regime are the following:

- Either metal or oxygen is soluble in the oxide
- Local thermodynamic equilibrium exists at the metal-oxide interface and at the oxide-air interface.
- The concentrations of the metal (or oxygen) at the two faces are therefore different.
- Metal or oxygen thus diffuses through the oxide layer under a concentration gradient which is proportional to 1/X.

Therefore the growth rate dX/dt can be described by:

$$\frac{dX}{dt} = A \cdot \frac{1}{X} \qquad \textbf{2-3}$$

And by integration:

$$X^2 = 2At + B \qquad \textbf{2-4}$$

which is known as the Mott-Cabrera parabolic law.

2.3. Verification of the Mott-Cabrera Theory Assumptions for the Formation of a Thin Oxide Film at Room Temperature

The first experiments of this kind have been performed by Ritchie and Tandon[15] and Hunt and Ritchie[16], respectively to test the enhancement of the oxidation rate of zinc and aluminum by adding trace impurities of iodine to the oxygen gas phase. In the second case for instance the oxidation rate is measured by measuring the resistance R of a thin evaporated aluminum film as a function of time during oxidation. As the metal was thinned by oxidation, the resistance increased and provided a measure of the extent of oxidation. The authors observed that the addition of traces of iodine increased the oxidation rate by a factor of up to 7. As can be seen in Figure 2-3, the addition of iodine resulted in an immediate increase of the reaction rate. The authors concluded that iodine was chemisorbed as anions on the growing oxide films and as such the electric field – originally due only to the presence of oxygen – was increased when both oxygen ions and iodide ions were adsorbed. The increase of the electric field resulted in an increase of the oxidation rate as theoretically predicted by Mott and Cabrera.

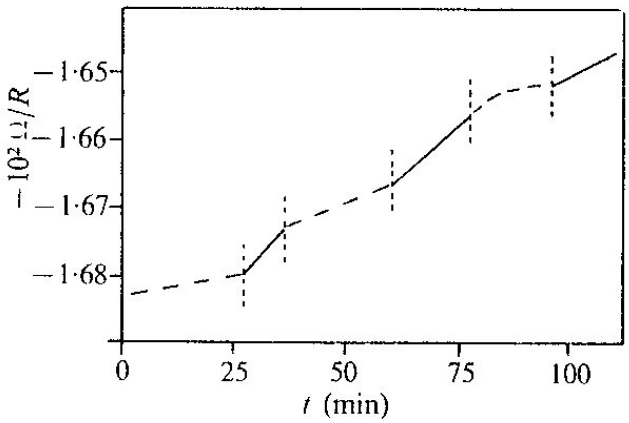

Figure 2-3: The effect of traces of iodine on the oxidation rate of aluminum at 373K: dashed lines represent oxidation in oxygen; solid lines represent oxidation in oxygen containing traces of iodine[16].

More recently, a refined experiment was performed by Popova et al. [17] to demonstrate the electrostatic field enhancement of Al(111) oxidation. In this study, an aluminum oxide film was electrostatically charged by electron-beam bombardment, which resulted in a greatly enhanced rate of Al(111) oxidation by molecular oxygen as can be seen in Figure 2-4 borrowed from this study. Again, this study correlates qualitatively with the Mott-Cabrera field-assisted model for oxide growth on metal surfaces.

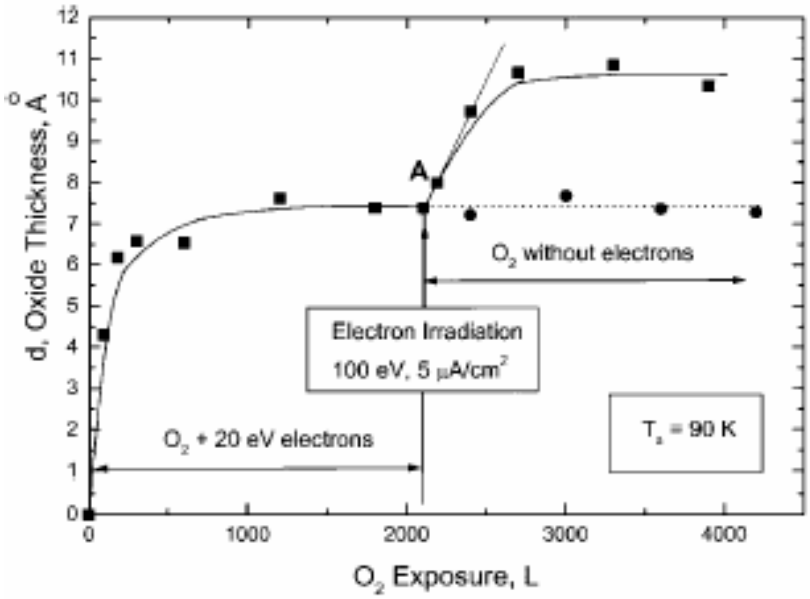

Figure 2-4: The uptake curve (oxide film thickness as a function of oxygen exposure). Electron assisted oxidation (20eV electrons) is used to grow the initial film. At point A the apparatus was evacuated and the oxide film was subjected to electron bombardment (100eV, 5μA/cm^2, 5 min). Subsequently, oxygen exposures were carried out at 90K. A dramatic increase of the oxidation rate for O_2 exposures following the electron irradiation is observed (squares). The additional oxidation of the sample beyond point A, carried out without the electron irradiation, does not result in any subsequent oxidation (circles)[17].

3. Growth Modes

The second part of this thesis deals with the formation of thin carbon films on Si(100) by CVD and by electron-beam-induced deposition (section 8), the application of this study to the creation of arrays of carbon dots on Si(100) (section 9) and the subsequent nucleation of Ge islands (section 10) by molecular-beam epitaxy. As we will see in section 7 these materials have great interest in the field of spintronics and quantum computing.

In this section, I review some important concepts related to the upcoming sections, such as hetero-epitaxy (by CVD or MBE) and heteroepitaxial growth modes.

3.1. Heteroepitaxy

Epitaxy comes from the Greek έπι (epi) which means 'on' and τάξι (taxy) which means 'arrangement'. Hence heteroepitaxy defines the epitaxial deposition process in which the chemical composition of the epi material is different than the chemical composition of the substrate.

3.1.1. Chemical Vapor Deposition vs. Molecular Beam Epitaxy

The two main techniques used for epitaxial deposition of a material B on a material A are the chemical vapor deposition (CVD) method and the molecular-beam epitaxy (MBE) method. In CVD, gases are introduced into the system at pressures ranging from UHV-conditions to atmospheric pressure. For example, to deposit Si or Ge, SiH_4 (silane) or GeH_4 (germane) would respectively be used, and dehydrogenation would be achieved at elevated temperatures.

Figure 3-1 shows a comparison between CVD and MBE. As can be seen, in CVD a gas containing the atoms of the deposited film is introduced into the system. Once the molecules hit the surface, they partially decompose and hydrogen desorbs from the surface. MBE is comparatively simpler with the generation of atomic beams of the film material which hit the surface. The atoms then diffuse over the surface until they finally bond at surface lattice sites. The typical base pressure for MBE is below 1.0 x 10^{-8} mbar, while it can vary from atmospheric pressure down to UHV-conditions for CVD.

Throughout this dissertation, Ge and Si are deposited on the substrate by solid-source MBE.

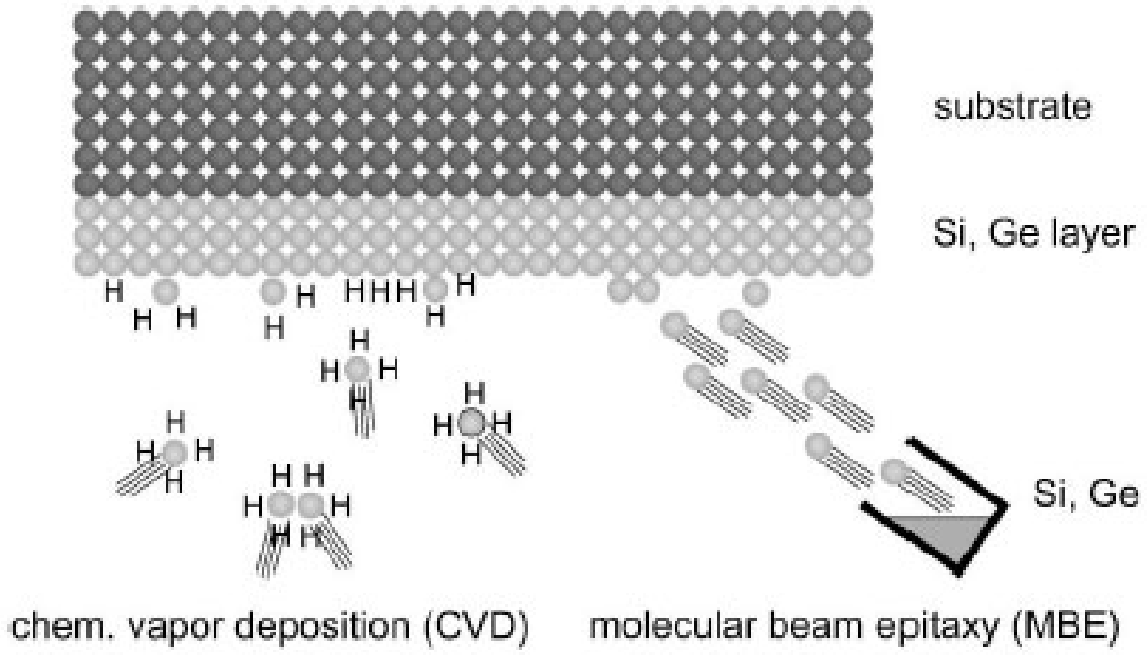

Figure 3-1: Principle of different deposition methods used in semiconductor epitaxy. In CVD, molecular gases (often hydrides) containing the atoms of the film are introduced. In MBE, atomic beams of the film material (generated by evaporation) hit the substrate surface[18].

3.1.2. Events at Surfaces

Let us now consider what happens upon deposition of a material B on a substrate A by MBE. Once the atoms of B hit the surface of A, many events can take place as shown in Figure 3-2. After the deposition of atoms on a terrace (process a), the atoms may diffuse on the terrace if the activation energy for diffusion is overcome (process b). In the event where two or more atoms meet, a nucleus can be formed (process c). If this nucleus is stable, more atoms will attach to it forming an island (process d). In the opposite case, atoms will detach from the island which will decay (process e). Additionally, atoms can attach to steps on the surface (process g) or might desorb from the terrace (process h).

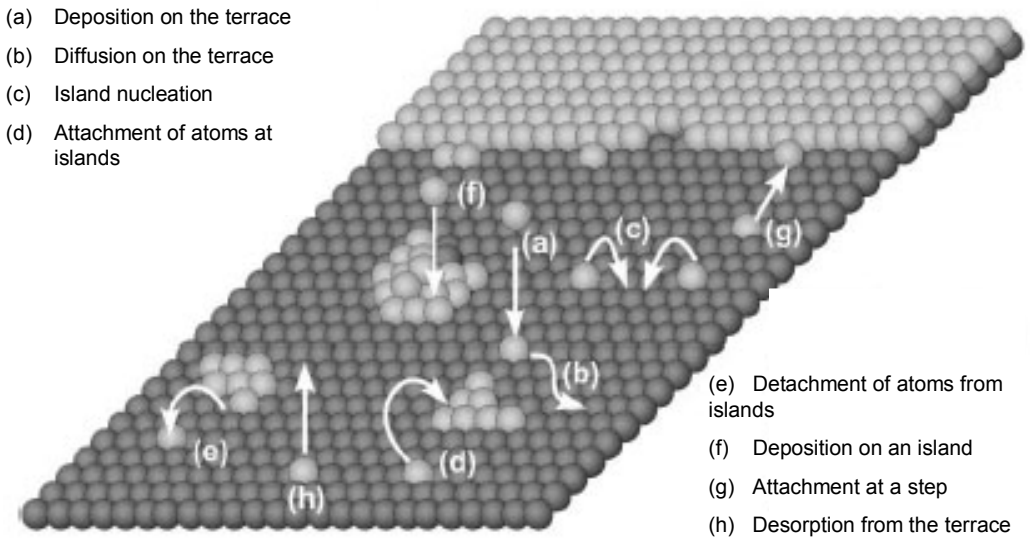

Figure 3-2: Schematic representation of different fundamental processes occurring in epitaxial growth: (a) deposition on the terrace; (b) diffusion on the terrace; (c) island nucleation; (d) attachment of atoms at islands; (e) detachment of atoms from islands; (f) deposition on an island; (g) attachment at a step; (h) desorption from the terrace[18].

3.2. Growth Modes in Heteroepitaxy

As illustrated in Figure 3-3 we can distinguish five growth modes (most frequently occurring) upon deposition of a material B on a substrate A [19-22]. These growth modes are: (a) Frank-van der Merve (FM) or layer by layer; (b) step-flow mode (SF); (c) Stranksi-Krastanow (SK) or layer + island; (d) Volmer-Weber (VW) or island growth mode; (e) columnar growth mode (CG). FM, SK and VW growth modes are the most important ones and will be detailed next.

The main factors contributing to the appearance of a growth mode over another one are the lattice mismatch between material A and material B, the growth temperature, the evaporation rate and the surface energies of both materials as well as the interface energy. The lattice mismatch between two materials is defined as the fractional difference between the atom spacing along a plane of the same crystallographic orientation as the interface plane in the respective bulk phase of the two materials.

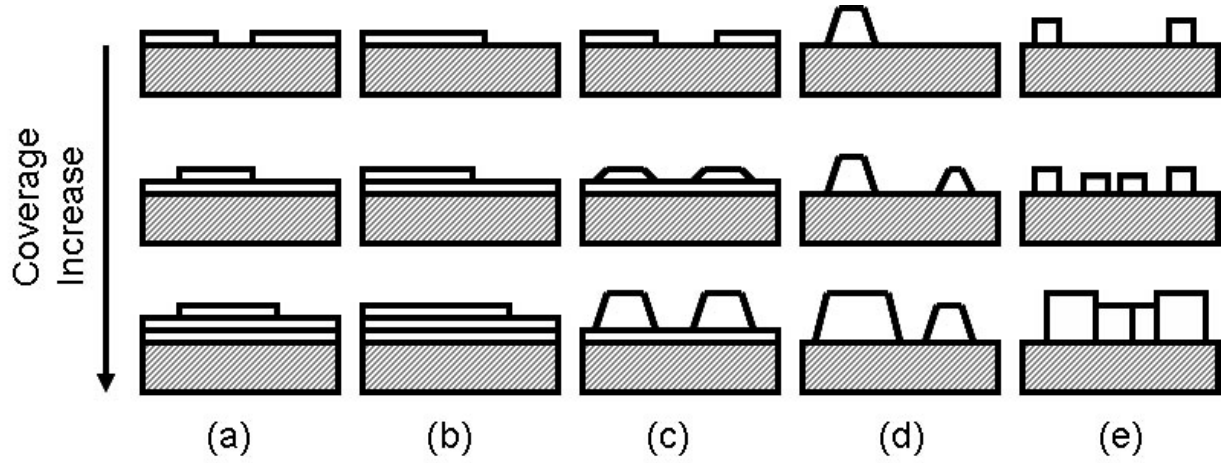

Figure 3-3: Schematic representation of the five crystal growth modes most frequently occurring on flat surfaces of substrate crystals. (a) Layer-by-layer or Frank-van der Merve (FM mode); (b) step flow (SF mode); (c) layer plus island or Stranski-Krastanov (SK mode); (d) island or Volmer-Weber (VW mode); (e) columnar growth mode (CG mode).

3.2.1. Frank-van der Merwe or Layer-by-Layer Growth Mode

This growth mode[23] will occur if, upon deposition of a material B on a substrate A, the atoms or molecules of B bound more strongly to A than to each other. After the formation of a monolayer, the substrate is covered with a second monolayer which is less tightly bound than the first one. From a simplified energetic standpoint, if the surface free energy of B is lower than the surface free energy of A, the interface energy between A and B being neglected, then the material B will wet the substrate A and layer-by-layer growth occurs.

In fact, the growth mode also depends on the elastic strain ε in the film which depends on the lattice mismatch between the substrate A (lattice constant a_A) and the film B (lattice constant a_B): $\varepsilon = (a_B - a_A)/a_A$. The lattice mismatch between A and B should be small for the FM growth mode to occur. The FM growth mode is often observed for adsorbed gases on graphite and on

several metals and when metals grow on metal substrates [24]. It is also very common in homo-epitaxy.

3.2.2. Volmer-Weber or Island Growth Mode

This growth mode[25] involves the direct nucleation of three-dimensional islands or clusters of material B on substrate A. The driving mechanism is opposite to the one for the FM mode: the atoms or molecules of B bound stronger to each other than to A. Again, from a simplified energetic standpoint, the surface free energy of B is larger than the surface free energy of A, the interface energy between A and B being neglected. Again, the growth mode also depends to some extent on the elastic strain ε in the film. This mode is often observed for the growth of metals on insulators, including metals on alkali halides and graphite. It was reviewed in details by Venables et al [20,26].

3.2.3. Stranski-Krastanow or Layer + Island

The Stranski-Krastanov growth mode[27] (SK) is an intermediate between FM and VW. After the formation of a few wetting layers of material B on substrate A, the subsequent layer growth becomes unfavorable and the growth mode converts to the formation of islands. The SK mode is the most widespread growth mode in hetero-epitaxy and what was once seen as the exception is in fact the rule.

Strain plays an important role. The energy responsible for the growth of islands increases considerably with strain. The driving mechanism is the very efficient strain energy relaxation possible with the formation of three-dimensional islands by lateral expansion or compression in

the direction of the free faces [28,29], because the material B conforms to the lattice of the substrate A for the first layers. Hence, because of the lattice mismatch between substrate A and deposited material B, the strain accumulated in the wetting layer of B on A linearly increases with the thickness of the wetting film. What is at stake is the balance between the energy that would be gained from relaxing with 3D-islands and the free surface energy building up. When the energy gained becomes larger than the increase in free surface energy, the formation of three-dimensional islands leads to a lowering of the total free energy of the system. Hence the existence of a critical size for the islands of material B formed on top of the wetting film. If we model the islands as cubes with edge lenghth = χ, the additional surface energy for a film in island morphology is proportional to the square of the island size χ^2. The gained elastic relaxation energy compared to that of a flat film is proportional to the volume of the island χ^3 . For the same total volume in the film, the energy difference between the three-dimensional island morphology and the flat morphology is:

$$\Delta E = E_{surf} - E_{relax} = \alpha\chi^2 - \beta\chi^3 \qquad \textbf{3-1}$$

with α and β constants.

This defines a critical size $\chi_{crit} = \alpha/\beta$ below which B-islands will not be stable on the surface[18]. For islands larger than the critical size, the formation of islands is energetically preferred over the flat morphology.

The SK mode was observed and studied in Si/Ge systems which will be the topic of the next part (section 4). It also occurs with III-V systems such as InAs/GaAs [30-32] and II-VI compounds for instance [33-35].

4. Si/Ge and Si/Ge/C Systems

In this section I review the present knowledge of Si/Ge and Si/C/Ge systems and, finally, I will discuss attempts to order Ge islands on Si(100) and their limitations.

4.1. Si/Ge System

The growth of Ge on Si(100) proceeds via the SK growth mode. After the formation of a Ge wetting film, whose thickness depends on the experimental conditions (substrate temperature and deposition rate), three-dimensional Ge islands nucleate randomly on the surface by self-assembly to relieve the strain accumulated in the Ge wetting layer (see section 3.2.3). Typically germanium is deposited by molecular-beam epitaxy or chemical vapor deposition on Si(100). A number of reviews have been written on this topic[18,36-44]. One can distinguish 3 regimes: below transition, after transition and formation of islands, and coalescence of islands.

4.1.1. Ge Wetting Layer

We consider the early stages of Ge deposition on Si(100), i.e. below the 2D/3D threshold, with the formation of a Ge wetting layer. For Ge epitaxy on Si(100) a (2 x N) reconstruction is observed on the two-dimensional strained wetting layer[45,46]. This reconstruction consists of a periodic array of missing dimers. Every Nth dimer of the (2 x 1) Ge reconstruction is missing as can be seen in the STM image in Figure 4-1. This regular array of missing dimers is an effective way to partially reduce the misfit strain by outward relaxation of Ge near the missing dimer. Conversely, the formation energy of the missing dimer leads to an increase of the film energy.

The balance between these two driving forces determines the periodicity N of the reconstruction. The second Ge atomic layer is affected by the (2xN) pattern. There is a competition between the need to lower the surface energy by forming a closed layer and the partial strain relief by dimer defect superstructures. Second layer dimer rows preferentially grow on top of the underlying dimer rows in the direction perpendicular to them (as is the case for Si(100)). The positions of the missing dimers in the first layer are thus not all filled up. Instead trenches of the width of at least one dimer row follow them. In addition, the second layer again contains missing dimer defects like the first layer at an angle of 90º to the trenches but with a smaller periodicity M=6-8. Effectively, the second layer is made up of Ge patches containing N x M lattice sites. Numerous STM studies[18,47-50] have addressed these issues, along with RHEED studies[51]. The formation of the Ge wetting layer on Si(100) is extremely important since its condition of formation will influence the size and shape of Ge self-assembled islands upon additional Ge deposition[52].

4.1.2. 3D-Nucleation and Coalescence

After deposition of a certain amount of Ge and the formation of a Ge wetting layer on Si(100), three-dimensional Ge islands randomly nucleate on the surface by self-assembly. Growth kinetics plays an important role in the 2D-3D transition so the substrate temperature can be used to tune the morphology of the resulting islands. At lower growth temperature the size of the 3D islands is reduced and their density increased, which is a result of the limited diffusion of the adatoms.

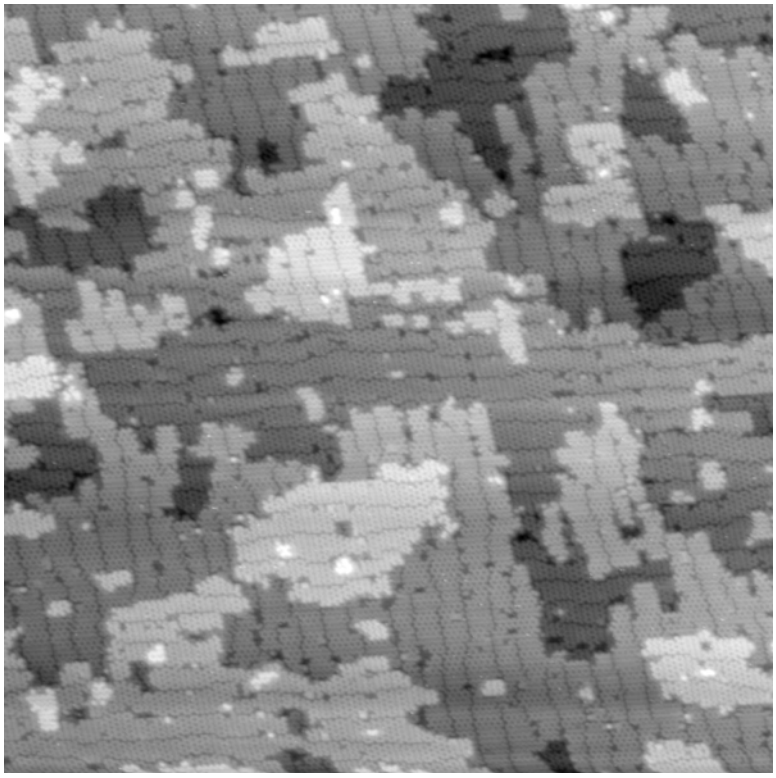

Figure 4-1: STM image showing the Ge wetting layer on top of Si(100)[53]. The 2xN reconstruction with every Nth dimer row missing is typical of the reconstruction of Ge on Si(100).

The formation of Ge nanostructures on Si(100) was first reported in 1991 by Mo et al[54] and soon followed by other experimental[50,55-60] and theoretical[61-64] reports. The formation of Ge islands is typically investigated in-situ by RHEED, which allows precise monitoring of the 2D/3D threshold[65-69] and by STM during deposition[18] or after deposition[70-72]. For ex-situ studies, AFM is the instrument of choice since it allows easy scanning over a large scale without additional sample preparation[59,65,66,68,69,73-87]. Other techniques such as TEM or cross-sectional TEM[66,74,77,84,86-88], energy dispersive x-ray analysis[86,87], x-ray diffraction[60,89], x-ray photoelectron spectroscopy[58,73,78,80,81,85], scanning electron microscopy[83], spectroscopic ellipsometry[73] or

medium-energy ion scattering[90] have also been used to investigate the morphology and properties of the Ge islands.

As shown in Figure 4-2 the size distribution of Ge islands on Si(100) is broad. This sample was prepared by depositing 6 ML of Ge on Si(100) at 870K, with a deposition rate of 0.16Å/s [91]. The density of 4.4 x 10^{+10} cm^{-2} corresponds to the typical density observed for this system.

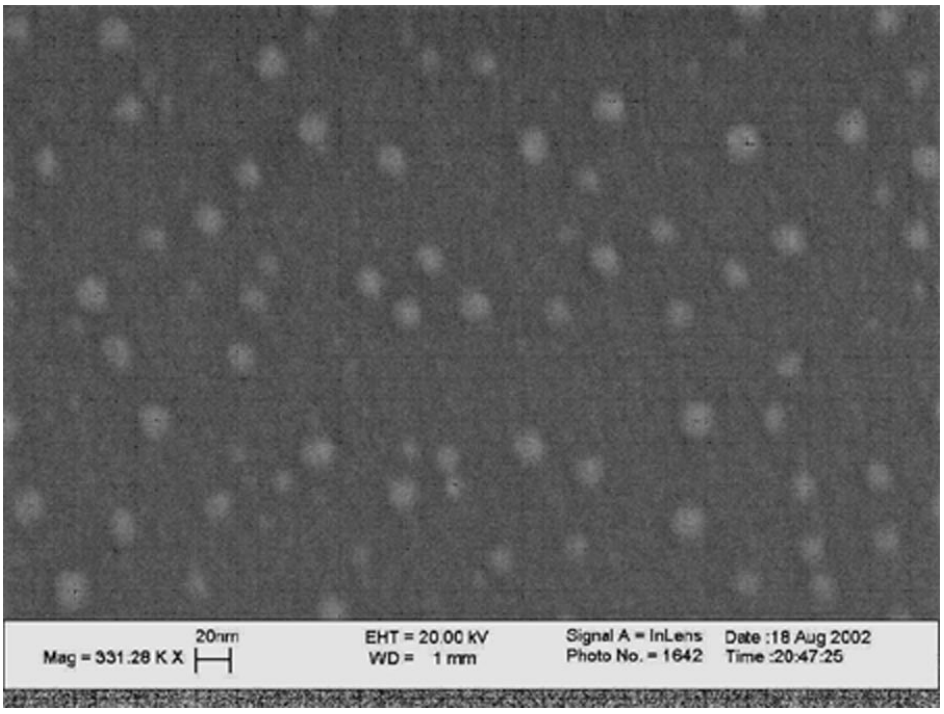

Figure 4-2: SEM image of Ge islands on Si(100)[91].

The size distribution and morphology of the Ge islands depend closely on the growth conditions. This explains the somewhat opposite results reported in the literature. Different morphologies for Ge islands have been reported. The transition between these morphologies was

also the topic of various studies. Mo et al. first reported the formation of elongated "huts" on Si(100) whose orientation matched the Si(100) axis[54]. Upon subsequent Ge deposition, square-based pyramids are formed which eventually turn into domes after additional deposition or long annealing time. The domes eventually coalesce and form "super-domes" at larger Ge coverage. AFM images showing the square-based pyramids and domes are shown in Figure 4-3 [91]. One can easily distinguish pyramids and domes by AFM by looking at the height of the structure: the height of a pyramid is typically a few nm while the height of a dome ranges from 10nm up to a few tens of nm. The "huts" are believed to be a metastable intermediate state[54] before a transition to larger "dome" clusters that show a more complicated mixture of various facets[47], and finally to macroscopic clusters "superdomes" [54]. STM images of a Ge pyramid, dome and superdome are shown in Figure 4-4 [71]. The transition shapes are temperature dependent[83]. In-situ STM by Medeiros-Ribeiro et al. revealed that the smaller square-based pyramids transform abruptly during growth to significantly larger multi-faceted domes. Both nanocrystals have size-dependent energy minima that result from the interplay between strain relaxation at the facets and stress concentration at the edges[70,75]. The coexistence of pyramids and domes under certain conditions results in a bimodal size distribution[65,68-70]. Much remains to be done in order to establish the relationship between the island-related luminescence energies and the island dimensions[68,69].

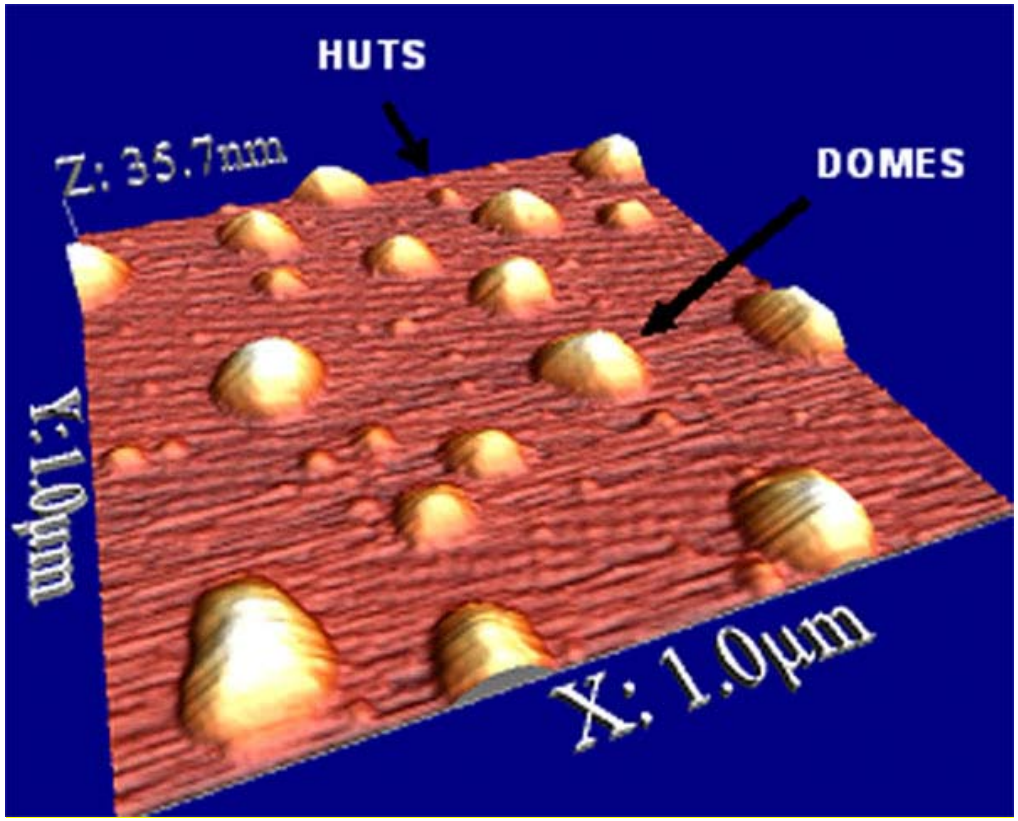

Figure 4-3: AFM image (contact mode) of Ge islands on Si(100). Scan area: 1μm x 1μm[91].

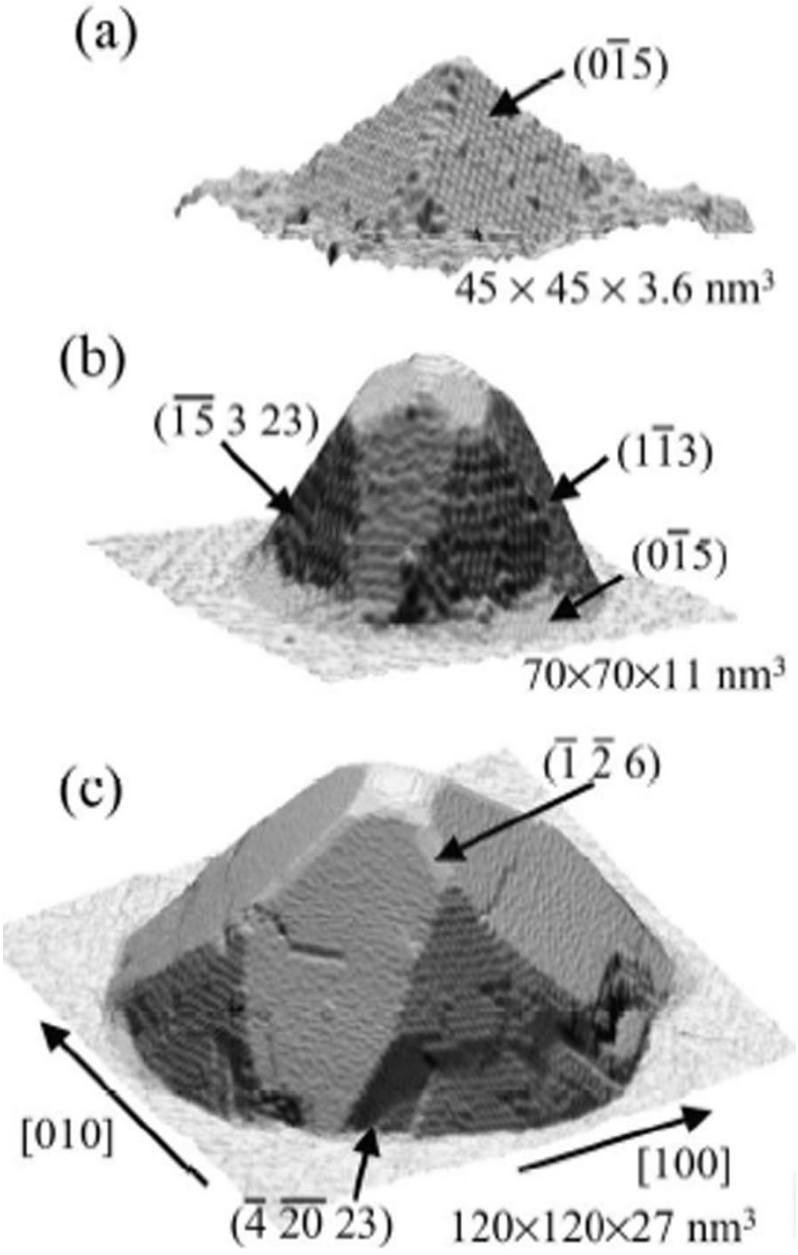

Figure 4-4: STM images of (a) a Ge pyramid, (b) a dome, and (c) a superdome[71].

4.2. Si/C/Ge Systems

As was discussed earlier, the deposition of Ge on clean Si(100) results in the nucleation of self-assembled Ge islands in a Stranski-Krastanov growth mode (because of the 4.2% lattice mismatch between Si and Ge). The smallest diameter observed for such islands is ~20nm and their size distribution is broad.

Recently, it was discovered that the pre-adsorption of carbon on Si(100) favors the nucleation of smaller Ge islands upon subsequent germanium deposition[92-94]. Typically 0.1ML to 0.3ML of carbon is deposited by MBE at a substrate temperature of 823K (which corresponds to the deposition temperature for germanium). It should be noted that at this temperature SiC is not formed on the surface. Carbon is randomly distributed on the Si(100) surface and STM studies of the surface after carbon deposition reveals the formation of elongated pairs of bright spots arranged into patches of c(4x4) superstructure[95] as can be seen in Figure 4-5. Si buckled dimers can be observed between the c(4x4) patches. STM imaging also reveals an enhancement of the surface roughness. The c(4x4) structure has been theoretically modeled[96,97] and it was showed that the short bond length of the C-C bond causes the carbon surface dimers to lie at the same height as the second-layer Si atoms to which they are bonded. The invisibility of the C-C dimers to STM when Si-Si dimers are present at the surface is due to lower geometric positions of the atoms and the lower energy of the bonding states of the C-C dimers. The Ge islands formed upon deposition of Ge on a C-precovered Si(100) surface have a diameter around 10nm and a height as small as 1nm, with a narrow size distribution as can be seen from the SEM image in Figure 4-6 [91].

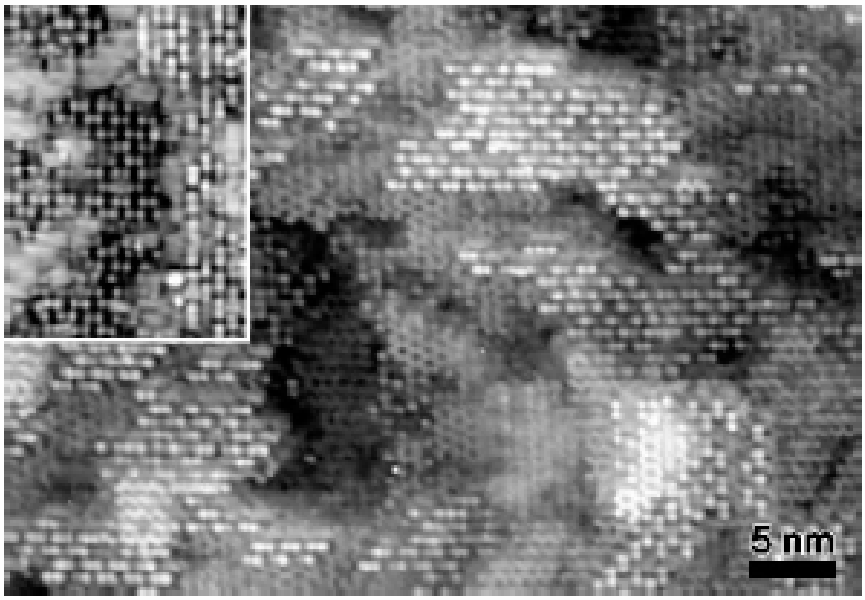

Figure 4-5: Filled state STM image (-2V, 0.2nA) after deposition of 0.11 ML C on Si(100) at a substrate temperature of 823K and a deposition rate of 2.3 10^{-4} ML/s. Areas covered with elongated pairs of bright spots lying in <110> directions exhibit a c(4x4) structure. The inset shows empty state data (+2V, 0.2nA), which exhibits essentially the same paired spot pattern[95].

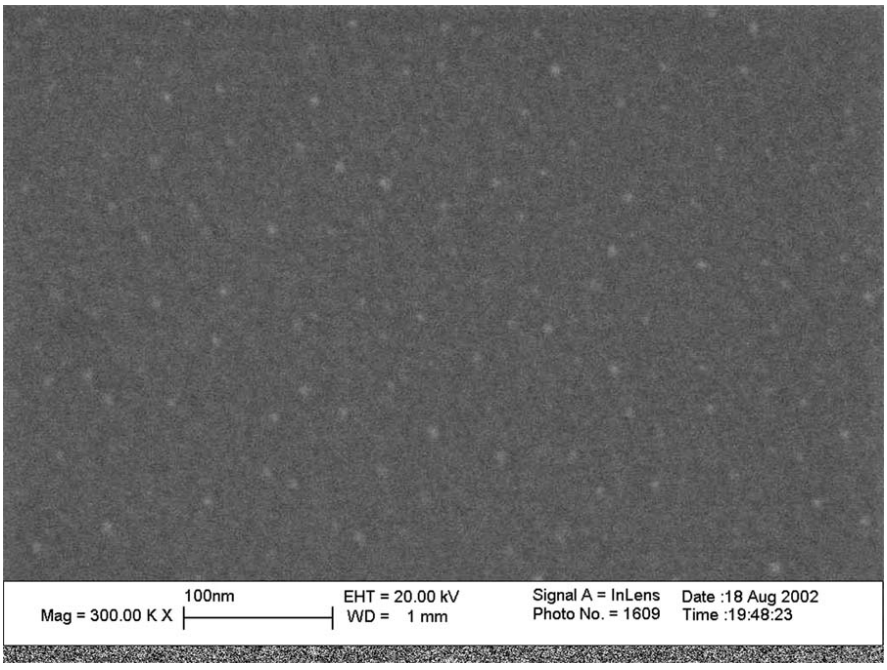

Figure 4-6: SEM image of Ge islands on Si(100) obtained by deposition of 0.1ML of carbon at 823K, followed by 3ML Ge at 823K [91].

Because of the 30% lattice mismatch between carbon and silicon, the pre-adsorption of carbon results in the creation of a very highly strained Si surface. This strain propagates to the Ge overlayer deposited on the C/Si surface. The strain experienced by the Ge overlayer is relieved by the formation of Ge islands upon Ge deposition in a Volmer-Weber fashion, i.e. direct nucleation of 3D-islands. Intense photoluminescence signal from these C-induced Ge islands can be observed as compared with photoluminescence of Ge islands on bare Si(100)[98-106].

The difference in growth mode between SiGe islands (Stranski-Krastanov) and SiCGe islands (Volmer-Weber) can be easily characterized by RHEED[107], X-ray scattering[108] or cross-sectional TEM[92,100,102].

As can be seen from Figure 4-7, the RHEED signal shows periodic oscillations for the Ge/Si system. Each period corresponds to the deposition of 1 ML wetting layer. The onset of formation of a new monolayer is marked by an increase of roughness and therefore a decrease of intensity. After the formation of half a monolayer, the roughness is maximum and the RHEED intensity reaches a minimum. The end of the oscillations marks the beginning of Ge island's nucleation (SK growth mode). For the Si/C/Ge system, oscillations are not observed, evidence for the direct nucleation of 3D Ge islands (VW mode).

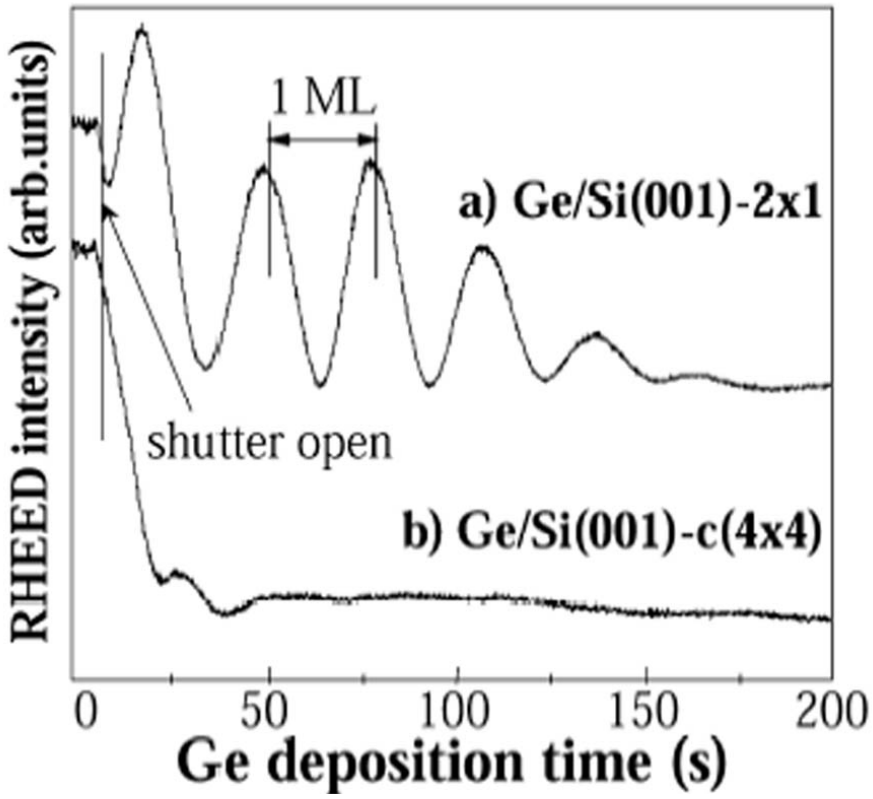

Figure 4-7: Comparison of the specular beam RHEED intensity evolution along the [110] azimuth during deposition of Ge at 400C on a clean Si(100)-2x1 surface (a) and on a clean Si(100)-c(4x4) surface obtained after 300L C_2H_4 exposure at 873K (b) [107].

4.3. Ordering Ge on Si(100)

4.3.1. Introduction

For optoelectronics applications[109-111], for use in quantum computing architecture[112-114], and quantum cellular automata[112,115], it is desirable to have control over two parameters: the diameter D of a Ge island, and the distance L between neighboring Ge islands (see Figure 7-2 section 7). The charge and optical coupling between regular arrays of Ge islands offer a range of potential applications in novel, quantum-dot electronic devices[116]. Control over the diameter of the dot

results in a narrow size distribution, which in turn results in homogeneous properties of the dots. The diameter of the Ge island determines how many electrons can be localized on the dot. Ideally one would like to have only one electron so the Ge islands have to be small. The spacing needs to be controlled in order to have controllable spin-spin interactions. Control over the distance between neighboring dots is also necessary to achieve any density required for quantum computing architectures.

Over the last 10 years, many attempts have been made to gain control over these two parameters, using various techniques.

In the following part, I will review the techniques used for ordering Ge islands on Si(100) substrates, the driving mechanism for the ordering of the islands along with the results obtained for D and L.

4.3.2. Ordering Techniques

4.3.2.1. Lithographically-patterned Si mesas

This technique was first reported for the InAs / GaAs system [117] and was later extended to the Ge/Si(100) system. Typically, thermally grown silicon dioxide is first formed on a Si(100) substrate and bare silicon lines or rectangles can be defined on the substrate by photolithography. After the formation of the SiO_2 layer a photoresist is applied to the surface as shown in Figure 4-8. At the end of the photolithography process the bare Si areas are surrounded by the oxide layer or an oxide layer is surrounded by bare Si. After processing of the wafer at high-temperature in a hydrogen atmosphere to clean the surface from contaminants such as solvents used in the photolithography process, a certain amount of Si is deposited on the crystal. The

deposition selectively occurs in the bare Si regions of the surface. After Ge deposition, one can observe the formation of Ge islands on the edge of the Si mesa plateaus [118-121]. As shown in Figure 4-9 Ge islands are ordered in a 1D- fashion, forming lines along the mesa edges. The average dot diameter is on the order of 100nm. The dot to dot spacing changes with the initial base width of the mesa and the smallest spacing reported is ~ 80nm [118]. This dot spacing dependence on the mesa width suggests that it is controlled by the strain distribution on the mesas. If the plateau on top of the Si mesa is replaced by a ridge – which can be achieved by reducing the dimension of the mesa base – Ge islands form a single line on top of the ridge [119,122,123]. Finally, one can also create a dense array of Si mesas whose lateral dimensions are so small – in the order of 140nm x 140nm – that only a single Ge island can nucleate on top of each mesa[124]. The use of many mesas opens up the route for real 2D-ordering of Ge islands as can be seen in Figure 4-10 [124]. This idea was also proposed by Jin et al [125].

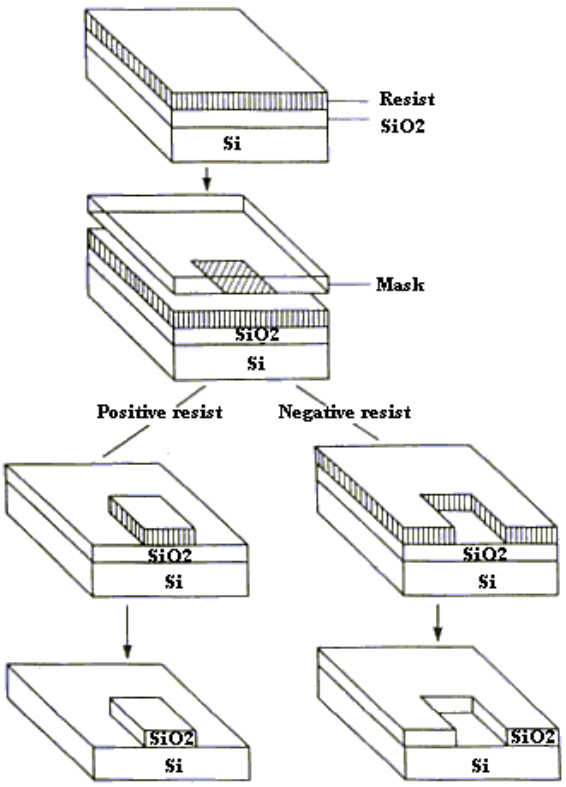

Figure 4-8: Schematic of the photolithography process. Two types of resist - positive or negative - can be used.

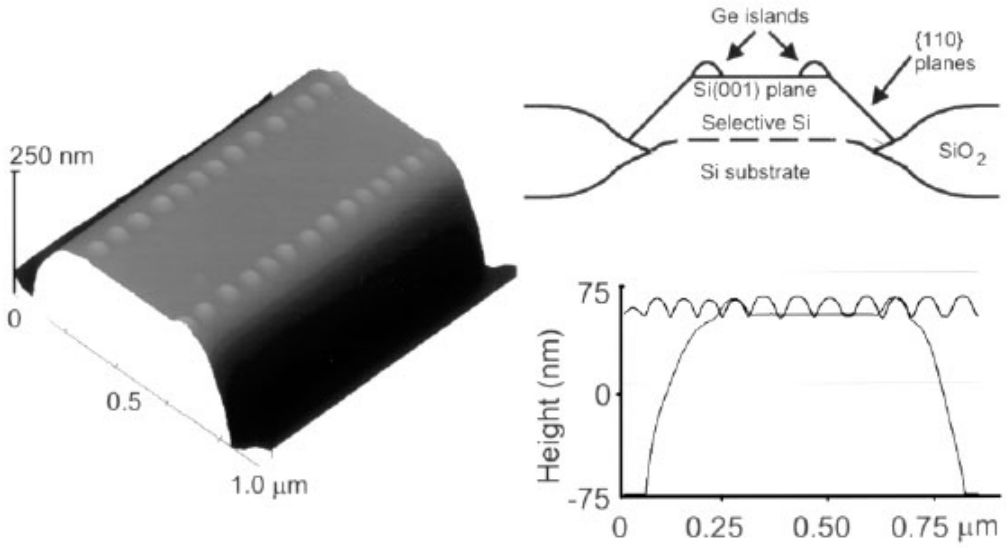

Figure 4-9: AFM and schematic cross section of Ge islands self-aligned along the edges of a Si mesa. Longitudinal sections along and orthogonal to the row of islands are also shown, illustrating the size uniformity and the fairly regular spacing within a row. From Ref. [119]

Two mechanisms can explain the observed nucleation of Ge islands along Si mesas edges or ridges. First, it can be explained by the easier distortion of the Si lattice at edges or ridges upon Ge deposition. Indeed, it has been shown by cross-sectional TEM that Ge islands tend to elastically deform the Si lattice to minimize the total free energy [55,126]. One should bear in mind that Ge and Si have a lattice mismatch of 4.2%, Ge being larger than Si. The easier strain relief at the edges or ridges provides a preferred nucleation of Ge islands at these positions. Second, it could be argued that the edges or ridges act as diffusion barriers for Ge and that the accumulation of Ge at these positions increases the probability of island nucleation[118].

The limitations of this technique are the relatively large island size and the absence of precise control over the island spacing. Although the formation of two-dimensional arrays can be achieved the relatively long time required for processing the wafer and for creating the Si mesas is a disadvantage.

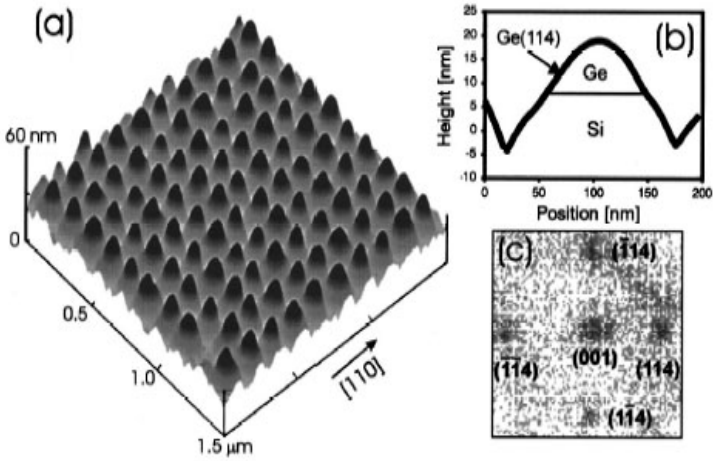

Figure 4-10: (a) AFM image of an array of Ge islands on prepatterned Si(100) surface. (b) Cross-section of the typical Ge island. (c) Normal view of a histogram of the statistics of the island surface normal vectors that are measured vertically with respect to the [001] direction and horizontally with respect to the [110] direction. From Ref. [124].

4.3.2.2. Vicinal Si(100) substrates

It is possible to increase the density of steps on a Si(100) substrate by increasing the cut angle of the crystal. If the miscut angle is sufficiently large, multi-atomic steps will be created on the surface[127]. Upon deposition of Ge, Ge islands nucleate at these multi-atomic steps, forming lines of Ge islands along the steps. This technique was again pioneered for the formation of lines of InGaAs quantum dots on a GaAs substrate [128]. The period between lines of Ge islands corresponds to the period between the steps and depends on the miscut angle [126,129-133]. Ge islands are still quite large, with diameters in the order of 100nm and island spacing around 140nm. Again, the inter-island spacing is mostly defined by the repulsive strain between neighbors. The preferred nucleation of Ge islands along the multi-atomic steps can be explained by the enlarged Si lattice which exists on the double-height steps and the resulting local strain field. Ge tends to accumulate at the steps and relaxes strain there, forming islands in a SK growth mode.

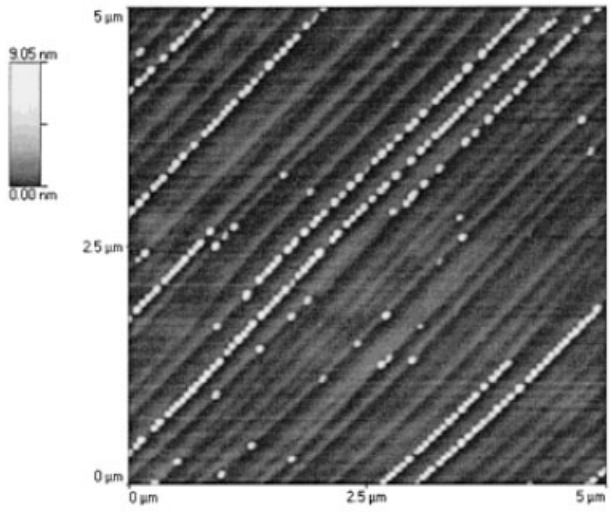

Figure 4-11: AFM image of vicinal Si surface annealed at 1100C on which 5ML Ge were deposited. The multi-atomic steps are visible as diagonal weak stripes. Aligned Ge islands decorating these steps appear bright. From Ref. [129].

The limitations of this technique are obvious from Figure 4-11. First, only one-dimensional ordering is created, with lines of Ge islands forming along the Si steps. Second, as mentioned above, the dimension D and spacing L of the Ge islands are too large and not precisely controlled, even though the size uniformity is good (typically below 10%).

4.3.2.3. Use of dislocations

Ge is deposited on a Si surface modified by misfit dislocations generated in buried compositionally graded Si_{1-x} Ge_x layers. Two types of such layers are typically created, both of them by molecular beam epitaxy (MBE). The first type consists of linear graded films where the Ge composition is increased with a grading rate of 10% per micrometer. A Si layer caps the graded structure. The second type is the so-called "strain bottle" system in which the Ge content is first linearly increased and then linearly decreased to zero. The dislocation strain accumulated in the buried system propagates through the Si capping layer. Upon deposition of Ge, ordering of Ge islands occurs, caused by the surface-strain patterns associated with the misfit dislocations [134-136]. As was shown by Fitzgerald et al. a non-uniform distribution of misfit dislocations in heteroepitaxial systems generates a non-uniform distribution of elastic strain at the surface [137]. As can be seen on Figure 4-12, the islands have diameters > 100nm with uneven spacing larger than 200nm.

The elastic strain field arising from the buried dislocations propagates through the capping layer. The lattice spacing at the surface is locally increased for the points located above the dislocation network. These points present therefore lower energy sites for the incoming Ge atoms to incorporate. Unfortunately, as can be seen in Figure 4-12, the 2D-ordering is far from

being perfect, with the spacing between neighboring lines of islands uneven. Many islands are missing, which might be due to the inhomogeneity of the strain propagating to the surface and to the high deposition temperature of Ge (~750C) and resulting high diffusion coefficient. Lowering the temperature might result in a lower number of missing islands, but at the same time, the high deposition temperature is required to ensure sufficient Ge diffusion so that Ge can reach the preferred nucleation sites.

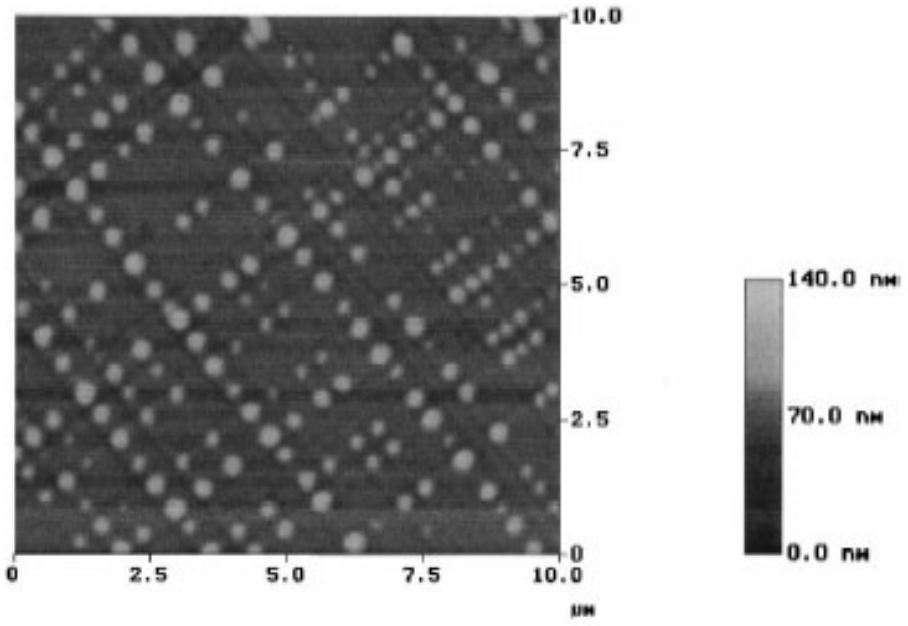

Figure 4-12: A 10μm x 10μm AFM image of the sample with 1.0nm of Ge coverage at 750C. From Ref. [136]

4.3.2.4. SiO_2/Si windows

The use of bare Si windows resembles the use of lithography to create Si mesas on the oxidized Si surface. After the formation of a thermally grown silicon dioxide film on the Si(100) crystal, small windows of bare Si are patterned on the surface using a scanning electron microscope combined with a lithography system via local removal of the oxide layer. Ge is then directly deposited on the sample. The nucleation of 3D Ge islands ensues following the Stranski-

Krastanow growth mode [138-142]. The size of the 'window' defines the size and arrangement of the Ge islands as shown in Figure 4-13. The smallest dots are about 70nm in diameter, obtained with a window size of ~90nm. Since the spacing between the dots is defined by the spacing between the windows, which in turn is defined by the lithography system, an excellent reproducibility in the dot-to-dot distance can be obtained. It should be noted that Ge is deposited at high temperatures (~700C) to allow for Ge diffusion over large distances [139-141]. To date, the smallest islands reported are still too large for interesting applications. Moreover, the sample surface is left with an oxide layer between the Ge islands.

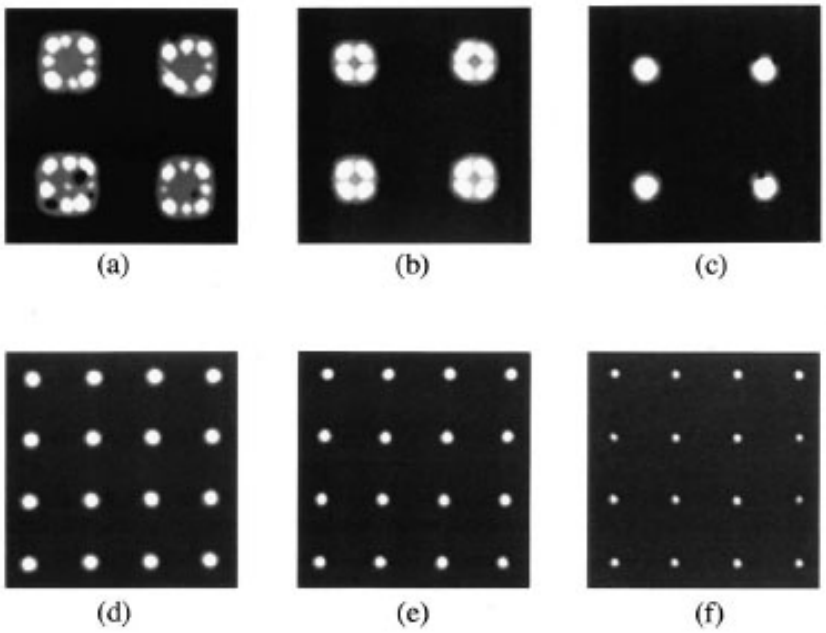

Figure 4-13: AFM images of Ge dots grown in windows of different sizes. The images are 2µm x 2µm. The windows sizes are respectively (a) 580nm, (b) 440nm, (c) 300nm, (d) 180nm, (e) 130nm, and (f) 90nm. From Ref. [140]

4.3.2.5. Focused Ion Beam – FIB

The technique was pioneered by Ross et al. [143] and later improved [144]. The Si(100) surface is micropatterned using a focused ion beam with Ga^+ ions. When the Ga^+ ion beam hits the surface, Si is locally sputtered and ion implantation occurs in parallel. Very precise micro-patterning is therefore made possible. The beam energy is varied typically from 5kV to 25kV. When Ge is deposited on the patterned surface, Ge islands nucleate following a SK growth mode and the formation of islands occurs exclusively at the locations irradiated by the ion beam. It is not clear as of yet whether the selective nucleation of Ge islands is controlled by a modification of the local strain field due to implantation of Ga^+ ions [135] or if the diffusion of Ga to the surface during the annealing step [145] creates a modified surface region which acts as a preferred nucleation center [146,147]. This technique favors an all-UHV process. The typical diameter of the dots is in the order of 20-50 nm and the spacing is as small as 75nm. Unfortunately the error bar in the mean diameter of the Ge islands is rather large.

4.4. Conclusion

The techniques presented above aim at ordering Ge islands on Si(100) substrates. As was demonstrated, some of them allow good control over either the spacing L between the islands or the diameter D of an island but rarely over both parameters at once. In the event they do, the dimension D obtained is still too large for interesting applications. The common point of these techniques is that they all rely on the Stranski-Krastanow growth mode to nucleate Ge islands on the Si surface. As was described in this section, upon deposition of Ge on bare Si(100), Ge forms

a wetting later whose thickness depends on the deposition temperature. When a critical thickness is reached, Ge islands start to nucleate on the surface. Nevertheless, extremely small Ge islands can never be fabricated following a SK growth mode because of the existence of a critical island size [18]. A summary of the Ge islands dimensions as a function of the technique used to order them is shown in Table 4-1. Since all these approaches follow a SK growth mode, the dimension of the Ge islands is unlikely to get below 20nm in diameter.

Table 4-1: Table showing the dot diameter obtained for various Ge islands ordering techniques reported in the literature. Also see Figure 4-14 for a plot of the diameters obtained. Line 2 in this table refers to the bibliography entries.

Entry Figure 4-14	1	2	3	4	5	6	7	8	9	10	11	12	13	14	15	16	17	18	19	20	21
Ref # Biblio	118	119	123	122	121	124	148	149	150	129	126	131	133	135	136	139	141	142	143	144	99
D (nm)	75	86	90	90	140	85	100	100	180	100	100	150	100	100	150	150	70	40	25	45	10

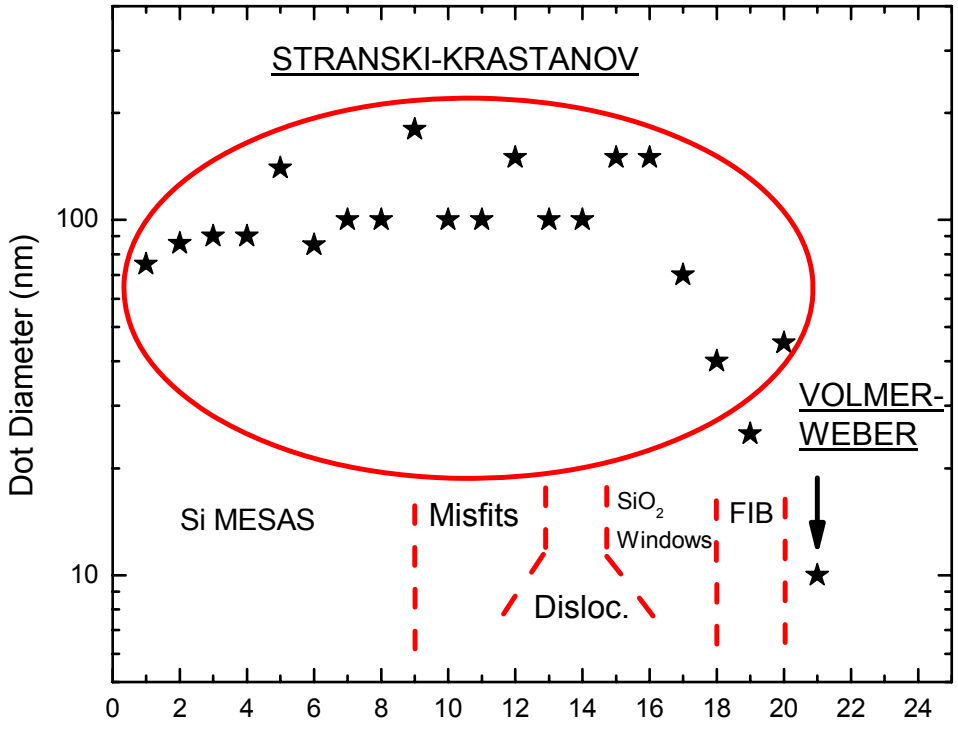

Figure 4-14: Graph showing the Ge island diameter as a function of the technique used for Ge island ordering on Si(100). These islands are grown following the SK growth mode. For comparison, the typical size of a Ge island nucleated on Si(100) with carbon pre-adsorbed (random nucleation, no ordering) following the VW mode is shown.

5. Development and Performance of the Nanoworkbench: A Four Tip STM for Electrical Conductivity Measurements Down to Sub-micrometer Scales

5.1. Abstract

A multiple-tip ultra-high vacuum (UHV) scanning tunneling microscope (MT-STM) with a scanning electron microscope (SEM) for imaging and molecular-beam epitaxy growth capabilities has been developed. This instrument (nanoworkbench) is used to perform four-point probe conductivity measurements at sub-μm spatial dimension. The system is composed of four chambers, the multiple-tip STM/SEM chamber, a surface analysis and preparation chamber, a molecular-beam epitaxy chamber and a load-lock chamber for fast transfer of samples and probes. The four chambers are interconnected by a unique transfer system based on a sample box with integrated heating and temperature-measuring capabilities. We demonstrate the operation and the performance of the nanoworkbench with STM imaging on graphite and with four-point-probe conductivity measurements on a silicon-on-insulator (SOI) crystal. The creation of a local field-effect transistor (FET), whose dimension and localization are respectively determined by the spacing between the probes and their position on the SOI surface, is demonstrated.

5.2. Introduction

In order to measure the electrical conductivity of surfaces and the influence of adsorbates on conductivity, it is desirable to perform local four-point conductivity measurements. As shown in section 1 the typical in-line set-up with four probes involves driving a current between the two outer probes while measuring the resulting voltage drop between the inner two probes using a high-impedance voltmeter (> 10GΩ in our case) so that very little current is drawn. This yields a current-voltage (*I*-*V*) curve dependent on the separation *d* between the potential measuring probes. It has a strong advantage over the two-probe measurements since it eliminates measurement error due to probe resistance and the contact resistance between the substrate and the probes. The four-terminal configuration also presents the advantage of being more versatile – provided that the probes can be controlled independently - allowing not only in-line measurements but also van der Pauw configuration electrical conductivity measurements in which the probes are placed in a square or rectangular configuration [151,152].

Four-point-probe instruments are commercially available but the spacing between the probes is usually fixed and too large to be able to probe structures at micrometer or sub-micrometer levels. For this reason, it is desirable to implement instruments with smaller probe-to-probe distances.

Recently, the development of multiple-probe instruments for conductivity measurements has been reported [7]. Dual probe configuration measurements have been performed [153-156] as well as four-point probe measurements [157-159]. One reported instrument utilized four parallel insulating cantilevers – which cannot be driven independently - fabricated by a conventional silicon

processing technique [160,161]. Another approach is based on four independently-driven probes for conductivity measurements in ultra-high vacuum [8,162].

We report the development and operation of the Nanoworkbench (NWB), a novel multiple-chamber ultra-high vacuum system based on a multiple-probe STM/SEM instrument designed to perform four-point-electrical measurements. Each of the four probes of the multiple-tip system can be operated independently as an STM with nanometer-scale lateral resolution and atomic-scale vertical resolution. This specificity greatly increases the potential of the instrument for conductivity measurement at sub-micrometer levels by allowing precise positioning of the probes and characterization of the surface or object of interest. The NWB also features a surface analysis and preparation chamber equipped with standard surface science tools as well as a molecular-beam epitaxy system.

5.3. Overview of the System

A schematic picture of the basic structure of the Nanoworkbench (NWB) is shown in Figure 5-1a. Four STM nanomanipulators, oriented at 45° from the normal, and at 90° to each other, electrically probe a small region on the surface of a material of interest. They are guided by an SEM which images the surface and the tips. The sample is mounted on a positioning platform with X, Y and Z motion. Attached to the NWB are: (1) a chemical preparation and characterization chamber; (2) a molecular-beam epitaxy chamber (MBE); and (3) a fast-entry load lock chamber (see Figure 5-1b). Samples and probes may be transferred from these chambers to the NWB. The system was designed using AutoCAD 14 software (Autodesk, Inc.)

in combination with ACIS 3D Open Viewer (Spatial Technology, Inc.). The entire system is mounted on an aluminum frame box designed and built as a highly rigid structure.

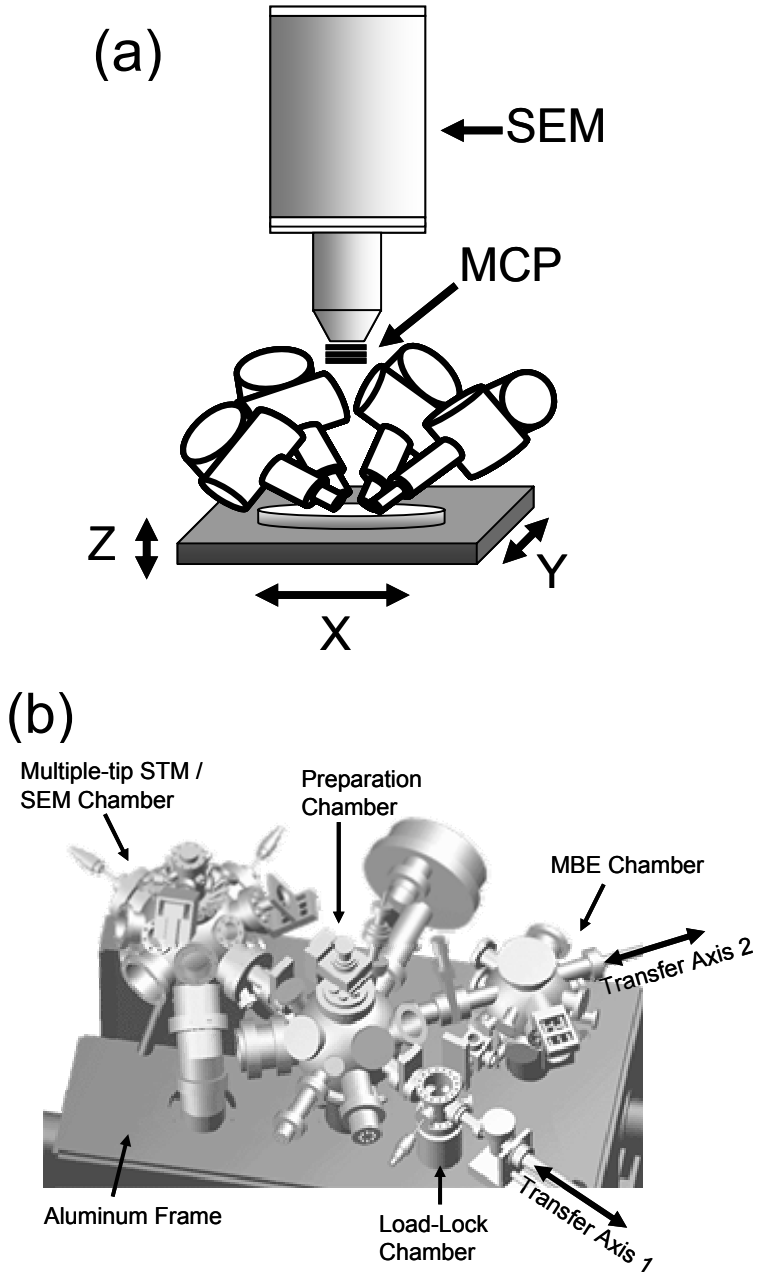

Figure 5-1: (a) Schematic picture of the Nanoworkbench. (b) Overview of the Nanoworkbench showing a multiple-tip STM / SEM chamber (left), a surface analysis and preparation chamber in the center featuring standard surface science tools and a molecular-beam epitaxy chamber (MBE) on the right equipped with Ge, Si and C evaporation sources. Additionally, a load-lock chamber allows for fast and easy transfer of the samples and probes following two transfer axes – Axis 1: Load-lock / Preparation chamber / STM-SEM chamber and Axis 2: MBE chamber / Preparation chamber.

5.3.1. Vacuum

The need for long mean free paths for electrons used in studying surfaces requires high or ultra-high vacuum. The average distance that a particle travels in the gas phase between collisions is given by equation 2-1. Ultra-high vacuum conditions will mean that the trajectories of particles such as ions or electrons will remain undisturbed over transit distances encountered in the vacuum system. Obviously, it is also necessary to keep the sample surface free from adsorbed gases during the course of an experiment.

$$\lambda = \frac{kT}{1.414 \times P \times \sigma} \quad [\text{m}] \qquad \textbf{5-1}$$

Where: P Pressure

k Boltzmann constant

T Temperature [K]

σ Collision cross section [m^2]

Two physical quantities are significant in characterizing the rarefied gas environment: these are the molecular incidence rate ϕ (the number of molecules striking a unit area per unit time) and the time t_m to build a monolayer, expressed as:

$$\phi = P \Big/ \sqrt{2 \times \pi \times m \times k \times T} \qquad \text{molecules/m}^2\text{.s} \qquad \textbf{5-2}$$

Where: m molecular mass [kg]

k Boltzmann constant

T Temperature [K]

Assuming a sticking probability equal to 1 for the impinging molecules on the sample surface, and knowing that the compact monolayer density of a molecule like N_2 with M=0.028kg/mol is about 8.10^{14} molec/cm^2, at T=298.15K, one can derive the following table.

Table 5-1: Evolution of t_m as a function of the background pressure in the system.

P (Pa)	P(mbar)	P(Torr)	t_m (s)
10^5	10^3	$7.5\ 10^2$	$2.7\ 10^{-9}$
10^0	10^{-2}	$7.5\ 10^{-3}$	$2.7\ 10^{-4}$
10^{-4}	10^{-6}	$7.5\ 10^{-7}$	$2.7\ 10^0$
10^{-8}	10^{-10}	$7.5\ 10^{-11}$	$2.9\ 10^4 \cong 480$min
10^{-9}	10^{-11}	$7.5\ 10^{-12}$	$2.9\ 10^5 \cong 80$h

5.3.1.1. Creation of Vacuum

We distinguish 4 levels of vacuum:

Rough Vacuum 1000 – 1 mbar

Medium Vacuum $1 – 10^{-3}$ mbar

High Vacuum (HV) $10^{-3} – 10^{-7}$ mbar

Ultra-High Vacuum (UHV) 10^{-7} mbar and below

To achieve the UHV conditions necessary for our experiments a complete pumping system has been assembled. Each chamber is individually equipped with one turbo-molecular pump, one ion pump and a titanium sublimation pump (TSP), with the exception of the load-lock chamber being only equipped with a turbo pump. In addition, each chamber is connected via hydraulically formed metal hoses and bellows to a fore-line pumped by a roughing pump.
The chambers are separated from each other by gate-valves and from the fore-line by hand-operated stainless steel Varian block valves. This allows any chamber to be pumped to UHV conditions while the others are under atmospheric pressure.

Titanium sublimation pumps are a form of getter pump in which the getter material is evaporated and deposited on the inner wall of the vacuum chamber as a getter film. Titanium is evaporated from a filament of high titanium content alloy by resistive heating. Particles from the gas which impinge on the getter film become bound to it by chemisorption. Since inert gases (He, Ar, CH_4) do not react with Ti, the sublimation pump is always used in combination with another high vacuum pump.

A schematic of the pumps / valves system for the Nanoworkbench is shown in Figure 5-2.

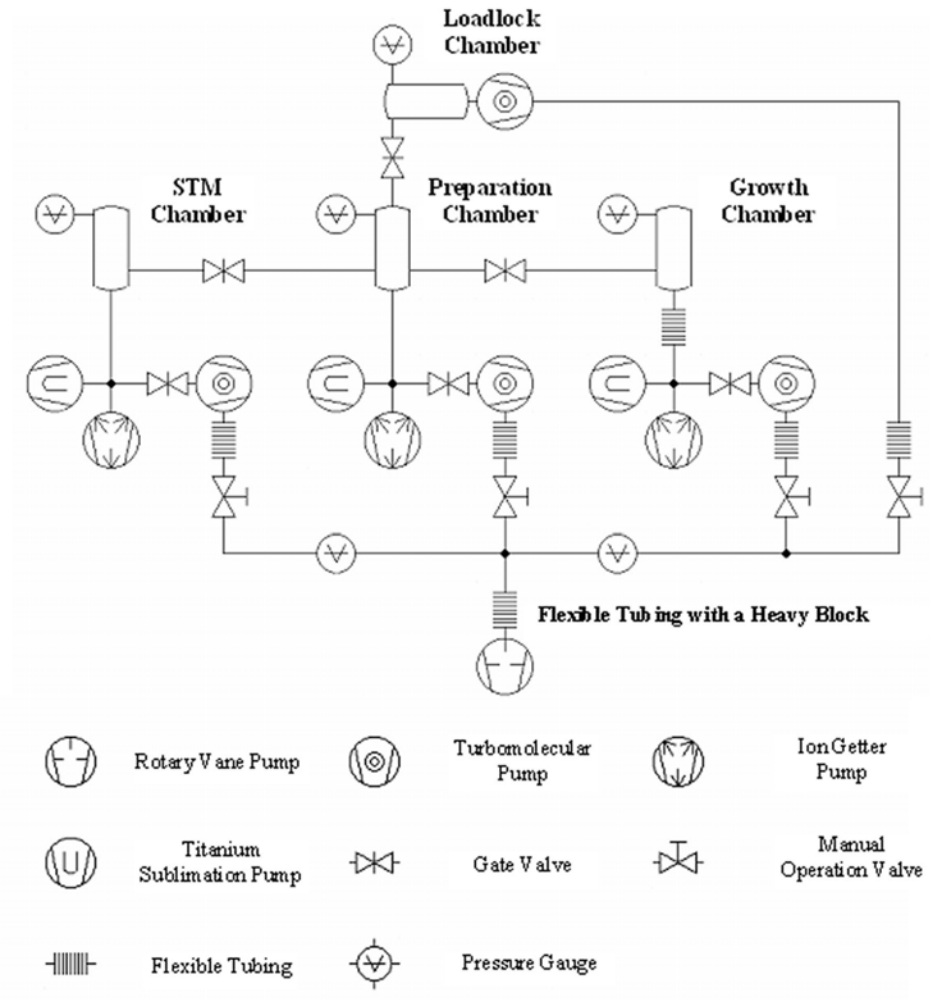

Figure 5-2: Schematic of pumping system for the Nanoworkbench.

5.3.2. Surface Analysis and Preparation Chamber

As shown schematically in Figure 5-3 the surface analysis and preparation chamber is a 15" diameter sphere, equipped with standard surface science tools, including a Perkin-Elmer Cylindrical Mirror Analyzer for Auger Electron Spectroscopy (AES model 10-155), a hemispherical Leybold-Heraeus EA-10 electron analyzer combined with a dual Mg/Al anode x-ray source for X-ray Photoelectron Spectroscopy (XPS), a UTI-100C quadrupole mass spectrometer (QMS), a home-made reverse view low-energy electron diffraction analyzer (LEED), an ion sputter gun and a gas dosing system. All the instruments are aligned radially along the chamber's equator (see Figure 5-3). An XYZ-manipulator with heating and cooling capability is used as a receiving stage for the sample box. These techniques are all widely used in surface science and this is not the scope of this dissertation to detail them here. A brief comparison of AES and XPS is provided in Table 5-2:

Table 5-2: Comparison of Auger Electron Spectroscopy (AES) and X-ray Photoelectron Spectroscopy (XPS)

	AES	XPS
Probe	Electrons	Soft x-rays
Detected Particles	Electrons	Electrons
Range	Li and higher	Li and higher
Sampling Depth	5-50Å	5-50Å
Detection Limit (Ratio)	1×10^{-3}	1×10^{-4}
Depth Profiling (speed and type)	Fast, Ions	Slow, Ions
Information	Elemental	Elemental, chemical
Quantitative	Semi	Semi
Spatial Resolution	>750Å	1mm to 200µm
Advantages	High spatial resolution Elemental mapping Analyzing conductors and semiconductors	Few limitations on sample type Chemical bonding information Often little damage to sample
Disadvantages	Charging with insulators Electron beam damage	Poor spatial resolution Cannot raster probe

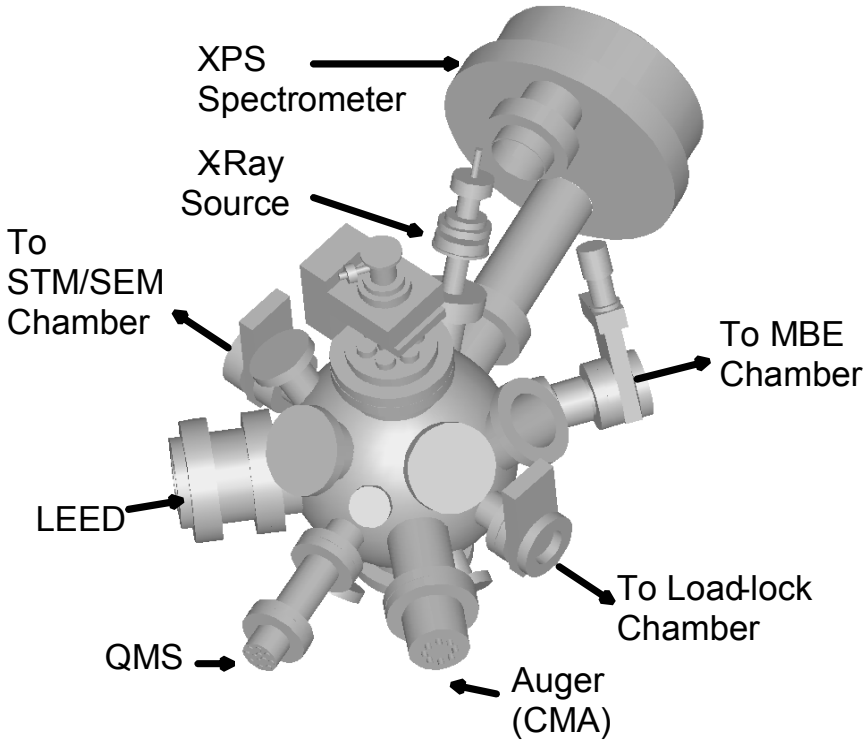

Figure 5-3: Configuration of the surface analysis and preparation chamber. The chamber is equipped with standard surface science tools such as AES, LEED, XPS and QMS as well as a gas-handling system.

5.3.3. Molecular Beam Epitaxy Chamber

Molecular Beam Epitaxy (MBE) is a UHV-based technique for producing high quality epitaxial structures with monolayer (ML) control. Since its introduction in the 1970s as a tool for growing high-purity semiconductor films, MBE has evolved into one of the most widely used techniques for producing epitaxial layers of metals, insulators and superconductors as well, both at the research and the industrial production level. The choice of MBE and other growth techniques depends on the desired structure and needs. For example, in the case of mass production, MBE suffers from a lower yield, compared to other techniques such as Liquid Phase Epitaxy (LPE) and Metalorganic Vapor Phase Deposition (MOCVD), due to a lower growth rate.

MBE, instead, is the proper technique when some particular requirements are needed, such as abruptness and control of interfaces and doping profiles, thanks to the lower growth temperature and growth rate. Besides, the control on the vacuum environment and on the quality of the source materials allows a much higher material purity, compared to non-UHV-based techniques. Finally, the UHV environment allows the use of electron diffraction probes such as reflection high energy electron diffraction (RHEED), which provide fundamental information on the growth mechanisms.

The MBE chamber (12" in diameter) is used for thin film deposition, doping or growth of quantum dots. It contains three 3 kW solid-source electron-beam evaporators (MDC – evap3000) and one 100 W wire source (MDC – evap100) as shown schematically in Figure 5-4. A Quartz Crystal Microbalance (QCM – Sycon model STM-100) is used to monitor thin film growth. An XYZ-manipulator similar to the one used in the preparation chamber serves as the sample box receiver. Each evaporation source can be isolated *via* a shutter mounted on a linear feedthrough.

Details about the quartz crystal microbalance are provided in the Appendix.

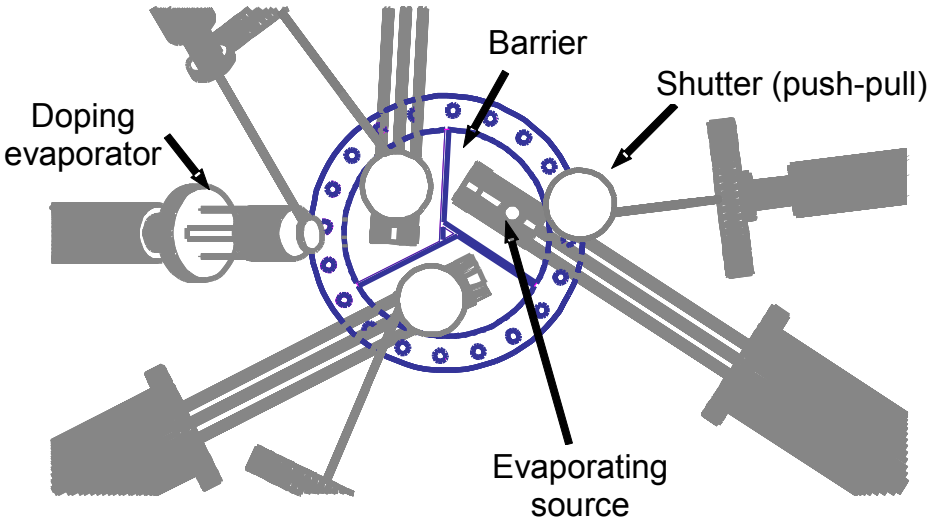

Figure 5-4: Top view of the evaporation system in the MBE chamber. Three evaporation sources (silicon, germanium and carbon) employ three separate shutters to control the evaporation process. A barrier separates the sources to prevent cross-contamination.

5.3.4. STM/SEM Chamber

The STM/SEM chamber is equipped with four nanomanipulators (Kleindiek Nanotechnik—model MM3 and MM3a) holding etched W or PtIr probes. The addition of a UHV-SEM (FEI—model 2LE-EVA) based on a Schottky emitter source allows fast and precise approach and positioning of the probes. The STM/SEM chamber also features a UTI-100C quadrupole mass spectrometer, a gas handling system as well as a probe-garage holding up to 10 tips and a sample box carousel holding up to 3 sample boxes.

5.4. Transfer System and Sample Box

5.4.1. Sample Box and Receiving Stages

For the preparation of clean crystal surfaces and the controlled deposition of materials by MBE, it is important to have precise control over the temperature of the sample in each UHV chamber. Moreover, it is desirable to have a system which can accommodate samples with various sizes and requirements. For this purpose a special transferable sample box with integrated heating and temperature measuring capabilities has been developed. As shown in Figure 5-5 the sample box is made of OFHC copper with highly-polished outer walls. Four UHV-compatible male banana plugs (Transfer Engineering and Manufacturing - model BPBPM) are tightly connected to the sample box and isolated from it with ceramic spacers. The outer plugs are made one of chromel and the other one of alumel. They are used for K-type thermocouple connections. The inner plugs are used as electrical heating connections and are made of BeCu, 304 stainless steel, and gold-coated for enhanced electrical performance and reliability. The sample box is equipped with stainless steel inserts on each side. These inserts with tapered holes match tapered pins on the transfer manipulator and are used to grab the sample box for UHV-transfer. The sample box can be equipped with either resistive or radiative heating devices. Figure 5-5 shows the resistive heating setup with a 10 mm x 5 mm x 0.5 mm Si(100) crystal. The crystal is resistively heated using non-interacting Ta contacts following a method described by Yates [163,164]. Alternatively, the sample box can be equipped with a radiative heater (Tectra – Boralectric – not shown here).

Each UHV chamber is equipped with a receiving stage such as the one shown in Figure 5-6. The receiving stage is also made of OFHC copper - with highly-polished inner walls closely

matching the outer walls of the sample box - and is equipped with a similar set of female banana plugs. The receiving stage features a set of 2 mm diameter stainless steel pins on each side to ensure rigorous alignment of the sample box during transfer. In addition, each receiving stage features a liquid nitrogen reservoir for cooling the sample.

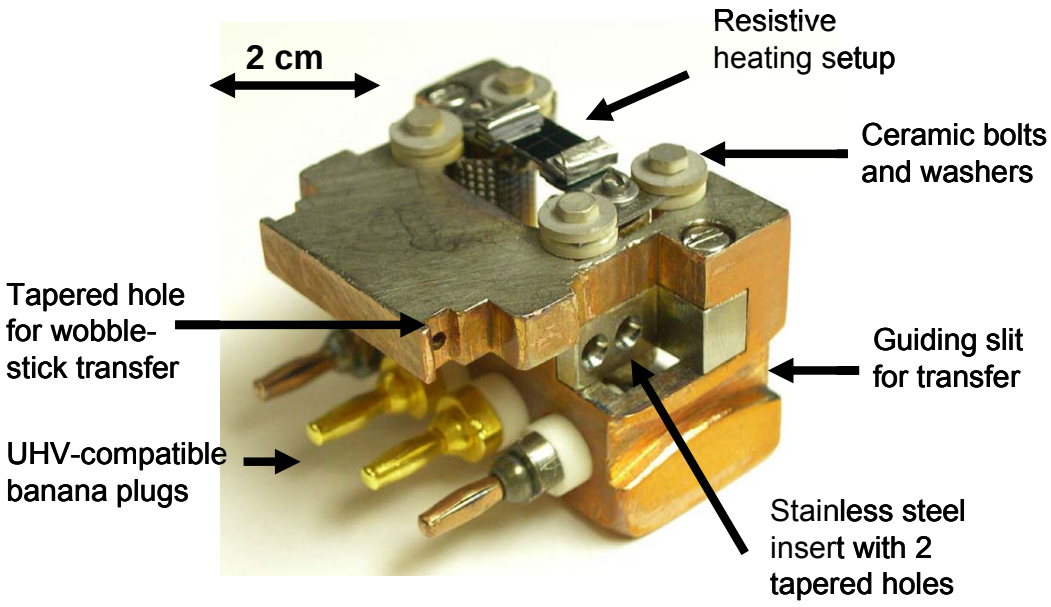

Figure 5-5: (a) Sample box equipped with four UHV-compatible banana plugs (models BPBPM) for heating and temperature measurements. Stainless steel inserts are used to tightly grab the sample box for transfer from one chamber to the next one. A resistive heating device is mounted on this sample box.

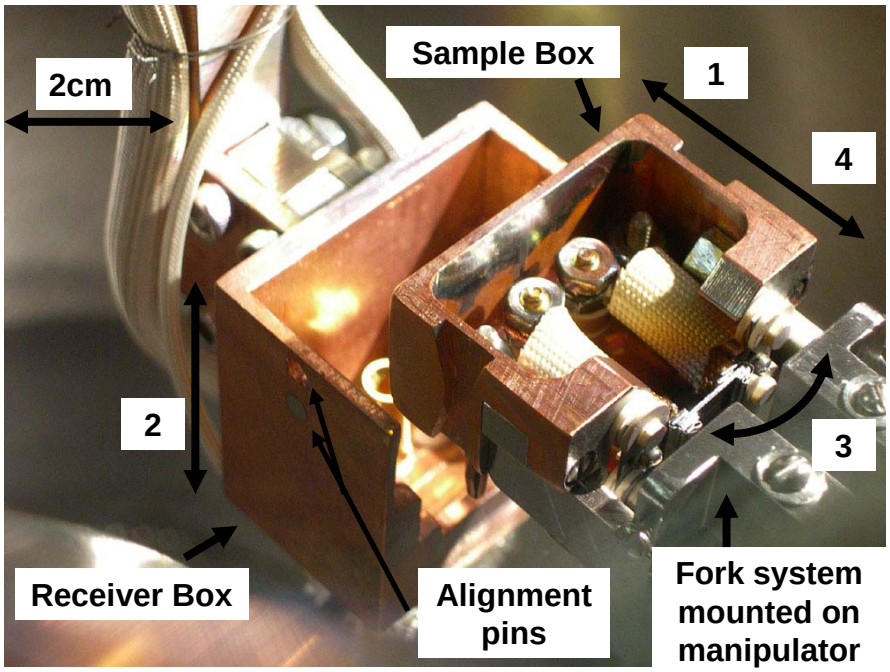

Figure 5-6: Snapshot of the sample box and receiver box in the preparation chamber. The transfer sequence is divided into 4 steps. (1) The sample box – held by the fork system of the linear/rotary manipulator approaches the XYZ receiver; (2) Once the sample box is positioned right above the receiving box, the receiver (controlled by an XYZ manipulator) is moved up, so that the receiving box tightly houses the sample box; (3) Once the connection is tight, the fork system is opened and; (4) the linear manipulator is moved away from the sample box. The sample box and receiving box are both made of highly-polished OFHC copper.

5.4.2. Transfer System

The transfer system is articulated around two main axes: Axis 1: Load-lock chamber – Preparation chamber – STM/SEM chamber, and Axis 2: MBE chamber - Preparation chamber, as can be seen in Figure 5-1a. Linear/rotary manipulators are used to transfer the sample throughout the system. In addition, two wobble-sticks are mounted on the STM/SEM chamber to allow for easy transfer of the sample box to the STM stage sample carousel as well as *in situ* tip-exchange. We use custom-made magnetically-actuated wobble-stick manipulators (Ferrovac) which are not affected by the pressure difference between atmospheric pressure and ultra high vacuum, allowing the shafts of the wobble-stick to be guided in a smooth and controlled way.

Both linear/rotary manipulators and wobble-sticks are equipped with a stainless steel fork system (pincer/grabber) featuring jaws with two stainless steel tapered pins at the end. These pins match the stainless steel inserts with tapered holes (see Figure 5-5) in the sample box and ensure enhanced stability during transfer of the sample box.

The typical transfer sequence is divided into 4 steps (see Figure 5-6):

(1) The linear transfer manipulator holding the sample box approaches the XYZ manipulator.

(2) Once the sample box is precisely positioned above the receiving stage, the XYZ manipulator is translated up, so that the receiving stage houses the sample box.

(3) Once the connection between the sample box and the receiving stage is tight, the fork system (pincer) at the end of the transfer manipulator is opened and,

(4) The linear manipulator is moved away from the sample box.

5.5. Multiple-tip STM/SEM Chamber

5.5.1. Overview - Nanomanipulators and XYZ-table

The STM/SEM chamber is directly connected to the preparation chamber (see Figure 5-1b). Its core is a multiple-tip scanning tunneling microscope (MT-STM) combined with a scanning electron microscope (SEM).

The MT-STM assembly is shown in Figure 5-7 (Figure 5-7a: side view and Figure 5-7b: top view). It comprises four nanomanipulators models MM3 and MM3a (Kleindiek Nanotechnik) mounted on a stainless steel ring at 90° from each other in the horizontal plane (see Figure 5-7b) and inclined at 45° from the sample plane (see Figure 5-7a). This design ensures a

large opening from the top to accommodate the SEM and its detector. Electronic components such as the preamplifiers for STM feedback control and imaging are also mounted on the STM stage mounting ring and are connected to the outside *via* electrical feedthroughs.

Both the STM nanomanipulators and the sample stage must be capable of coarse and fine motion. The design of the Nanomotor ® [165] achieves both through its unique design. For fast large travel, the Nanomotor ® can be driven in the coarse step mode which exploits the well known stick-slip mechanism [166]. At the same time, positioning in the nanometer range is possible in the fine step mode, which utilizes the piezoelectric effect in the conventional way [167].

The sample table (Kleindiek Nanotechnik, model LT6820XYZ) has three perpendicular degrees of freedom and is equipped with three Nanomotors. The table can travel 20 mm in the X and Y directions and 15 mm in the Z direction. The integrated optical encoding system allows positioning of the sample with 100 nm repeatability. The stiffness of the table was enhanced by mounting additional vertical aluminum columns.

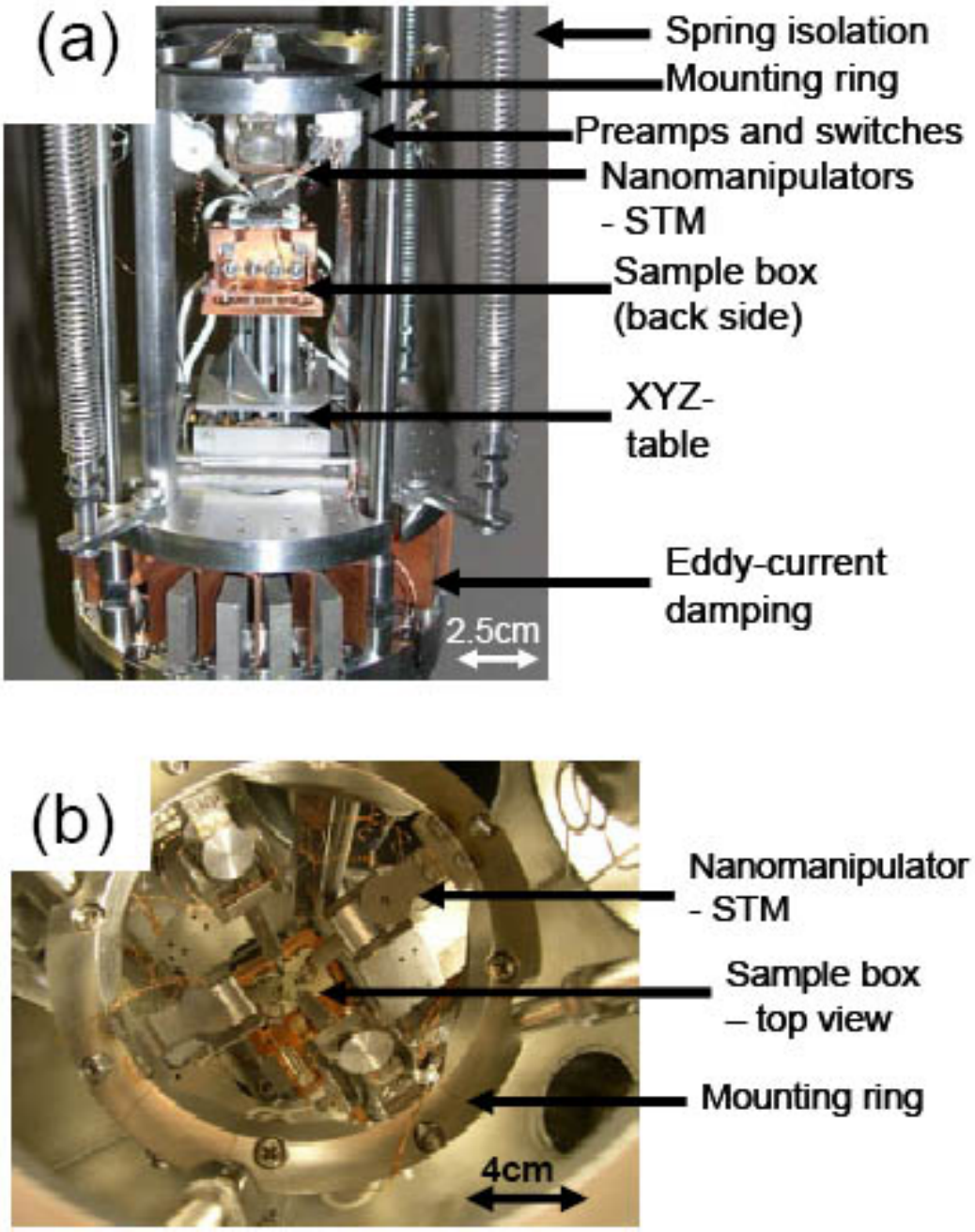

Figure 5-7: (a) Overview of the STM stage in the STM / SEM chamber. The STM stage features four nanomanipulators that can be used as STMs (models MM3 and MM3a – Kleindiek Nanotechnik) mounted on a ring at 45° from the sample plane, a sample stage mounted on an XYZ-table, as well as spring isolation and an eddy-current damping system. (b) Top view (SEM point of view) showing the four nanomanipulators mounted at 90° from each other in the sample plane (horizontal plane). The large solid angle allows enough space to accommodate the SEM-gun.

The nanomanipulators have been developed in collaboration with Kleindiek Nanotechnik for STM applications. As shown in Figure 5-8 the nanomanipulators have two rotational axes (X, Y) and one linear motion (Z). Two slightly different models are being used: the MM3 model with a length of 80 mm and the MM3a model with an overall length of 65 mm.

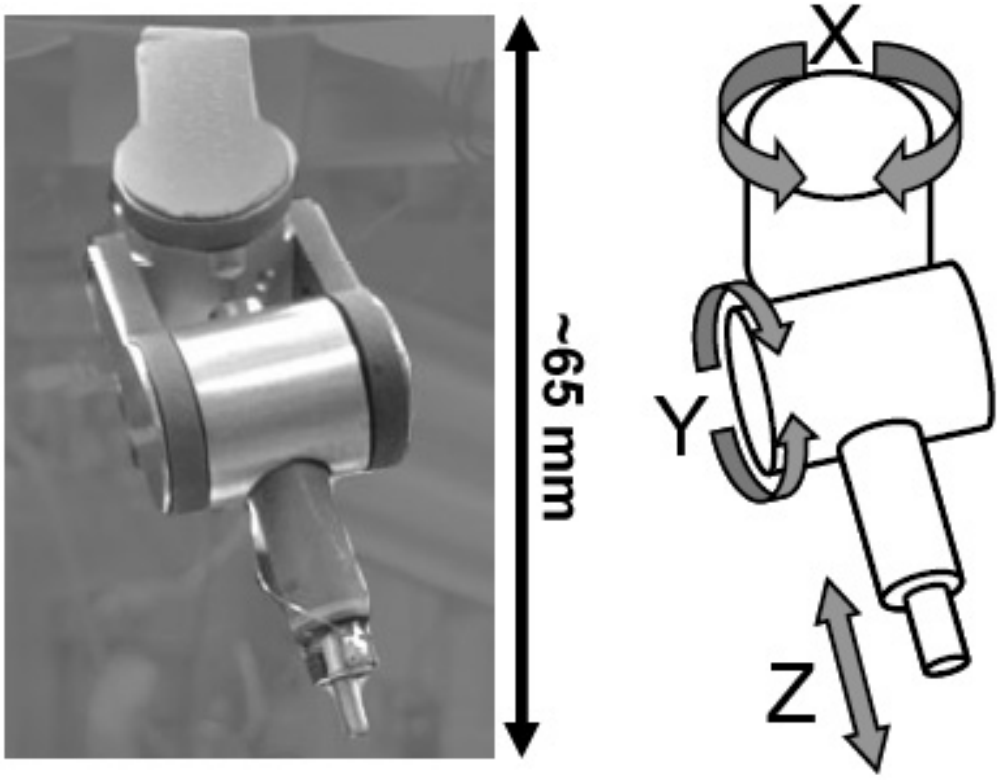

Figure 5-8: Left: a photograph of the MM3a nanomanipulator. Right: schematic showing both rotational axes (X, Y) and the linear motion (Z) of the nanomanipulator.

From the standpoint of control electronics, the simultaneous operation of four STM devices or the performance of four point probe conductivity measurements on a small scale is a challenge by itself. The SPM electronics for the four-tip STM is provided by Kleindiek

Nanotechnik (Nanomotor® STM Control and Image Acquisition Electronics / Software). The electronics is controlled *via* a computer through an RS-232 serial interface. Each SPM electronics system is controlled by a dedicated PC to guarantee simultaneous independent operation of all four nanomanipulators. An analog feedback-loop is used in constant-current mode. To reduce coupling of ambient electromagnetic noise the first amplification stage of the tunneling current is located inside the UHV system close to the nanomanipulators using a low-noise fast operational amplifier OPA111 (Burr-Brown). The gain of the OPA111 is set with a 100 MOhm resistor. With this setup the range of voltage/current is -2.5 V to +2.5 V (restricted by SPM electronics)/ -100 nA to +100 nA (restricted by the specification of OPA111 in combination with a 100 MOhm resistor). To enable four-point conductivity measurements, direct electrical access to the probes is also desirable. Low dissipation electromagnetic relays (Teledyne, type 732-12) are mounted close to the OPA111, as shown in Figure 5-9.

The MM3 nanomanipulator is composed of a tube connected to the piezo drive, whose inner diameter is 1.50 mm. The tip holder must fit in this tube and hold onto it. The tip holder is made out of stainless steel. Tip exchange under UHV requires the use of wobble stick to grab, manipulate and transfer the tip holder assembly. As shown in Figure 5-10, the tip holder is slotted parallel to its central axis (7mm deep) so that its upper part acts as a spring. When grabbing the tip holder with a wobble-stick, the upper part is compressed, reducing the effective holder diameter, allowing the tip to be inserted into the manipulator tube. Upon releasing the tip holder, the force of the spring is released, holding the tip assembly in position.

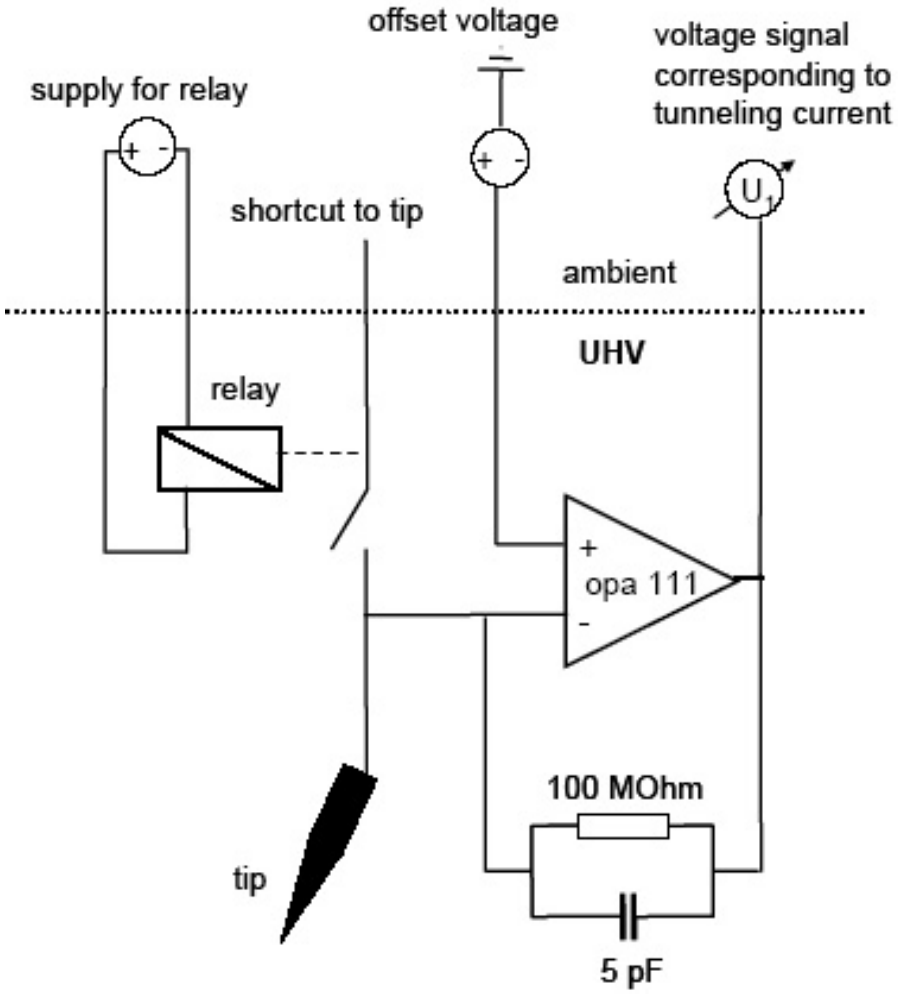

Figure 5-9: Schematic of preamplifier and relay electronics close to tip. The parts shown below the dashed line are located inside the UHV chamber.

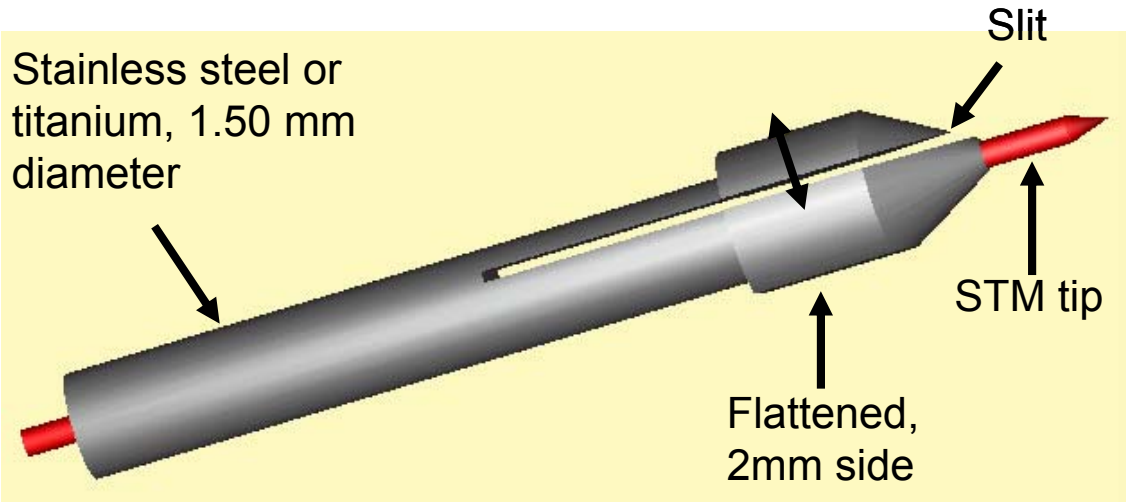

Figure 5-10: Schematic of the tip holder assembly. The tip holder slides into the piezo tube of the nanomanipulator. PtIr etched wire is mounted in the tip holder.

5.5.2. UHV-SEM + MCP Detection

The SEM column (FEI - Model 2LE EVA) is based on a Schottky emitter source with a two-lens electron technology and an electronically-variable aperture. Mounted on top of the chamber, it is mainly used to locate features on the surface and to guide the STM tips near objects of interest.

Conventional scanning electron microscopes (SEM) operate at pressures near 10^{-6} mbar. Therefore typical SEM detection systems are based on scintillation amplifiers (a summary of SEM detectors can be found in [168]). In these systems secondary electrons are converted into light and subsequently the photons are converted back into an electrical signal, which limits the sensitivity and signal-to-noise ratio (typical gains are in the range of 10^4).

The UHV environment of the nanoworkbench system permits the use of a high efficiency multi-channel plate (MCP) system, similar to those used in UHV instruments for ion and electron spectroscopy [164]. A typical MCP consists of an annular array of tiny glass tubes (12-23 μm diameter and 0.5 to 1mm long) fused together to form an array of thousands of independent electron multipliers. An accelerating potential is applied to a metal film deposited across the ends of the tubes, and when an electron enters a tube it produces additional secondary electrons as a result of striking a special highly emissive coating on the inside of the tube. Two MCPs stacked together are used to create a gain approaching 10^7.

Figure 5-11 shows a schematic diagram of the ultra high efficient secondary electron detection, the electron beam deflection and image recording system used in the nanoworkbench. Here we use an ultra-thin (2.5 mm maximum) annular MCP assembly with a center hole (Hamamatsu F6589), which is directly mounted below the SEM electron column. The shielded center hole allows undisturbed travel of the primary electron beam to the sample surface. The detector position above the specimen surface is ideal for collecting a large percentage of secondary and backscattered electrons emitted from the specimen surface. Because of the large solid angle detection efficiency of the MCP, shadowing due to the nanomanipulators and the topography of the specimen is minimized. In particular, in the area of critical dimensions, the MCP can provide uniformly illuminated shadow-free images from which highly accurate measurements can be obtained. The front surface of the detector array may be biased positively or negatively to attract or repel secondary electrons from the sample. In this way a secondary electron image or a backscattered electron image may be selected easily.

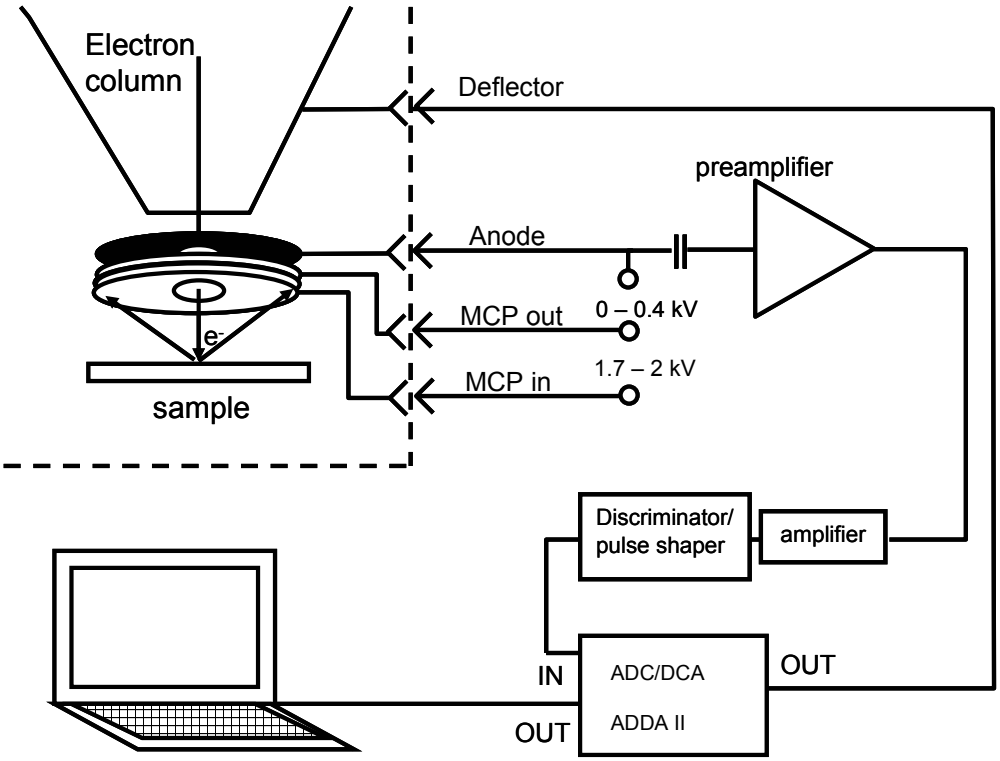

Figure 5-11: Schematic of the SEM-MCP detection system.

The electronic amplification and pulse shaping of the MCP output signal is performed by a combination of a commercially available preamplifier (ORTEC Fast Preamplifier model 9301), and an amplifier (ORTEC Amplifier Discriminator model 9302) along with an home-built pulse shaper. The resulting pulse sequences (up to 20 MHz frequency) are digitized and synchronized with the deflection controller using a fully programmable scan system (ADDA II, Soft Imaging System). The ADDA II system is connected to a PC for control of scan parameters and image recording.

Under experimental conditions – in four-point probe configuration - the SEM resolution is approximately 100 nm. Large working distances imposed by the design of the STM stage limit the SEM-resolution of the instrument.

5.5.3. Docking-stage

The STM unit is decoupled from the electron column mounted on top of the STM/SEM chamber *via* the spring isolation system and the eddy-current damping unit (see section 5.5.4). As a result, the distance between the sample (which floats during STM imaging) and the electron gun aperture is not constant. Such variation in the working distance makes it difficult to focus the SEM, especially at high magnifications ($\geq 10^3$).

A docking system has been developed to address this problem. Figure 5-12 shows the design of the docking mechanism. It consists of three pairs of metal pillars and a piston-like linear actuator. One metal pillar is mounted on the STM unit, whereas the second pillar in a given pair is mounted on the frame under the STM unit. The mating faces are mirror-finished to ensure excellent mechanical contact. The actuator is composed of a piston head and a cylindrical chamber without any contact with one another. These two elements are connected to the linear motion feedthrough and the STM unit, respectively. When the piston head of the actuator is pulled down (using the linear motion feedthrough) it makes contact with the cylindrical chamber to transmit the linear motion and, consequently, pulls down the STM unit until both pillars are in contact. A spring between the linear motion feedthrough and the actuator regulates the linear force to give a consistent pulling force. When the STM unit is undocked, the piston head does not have any contact with the cylindrical chamber, and the STM unit is floating, completely decoupled from the rest of the system (Figure 5-12a). This position is used for STM operation and conductivity measurements. For high-resolution SEM imaging, it is preferable to dock the stage (Figure 5-12b).

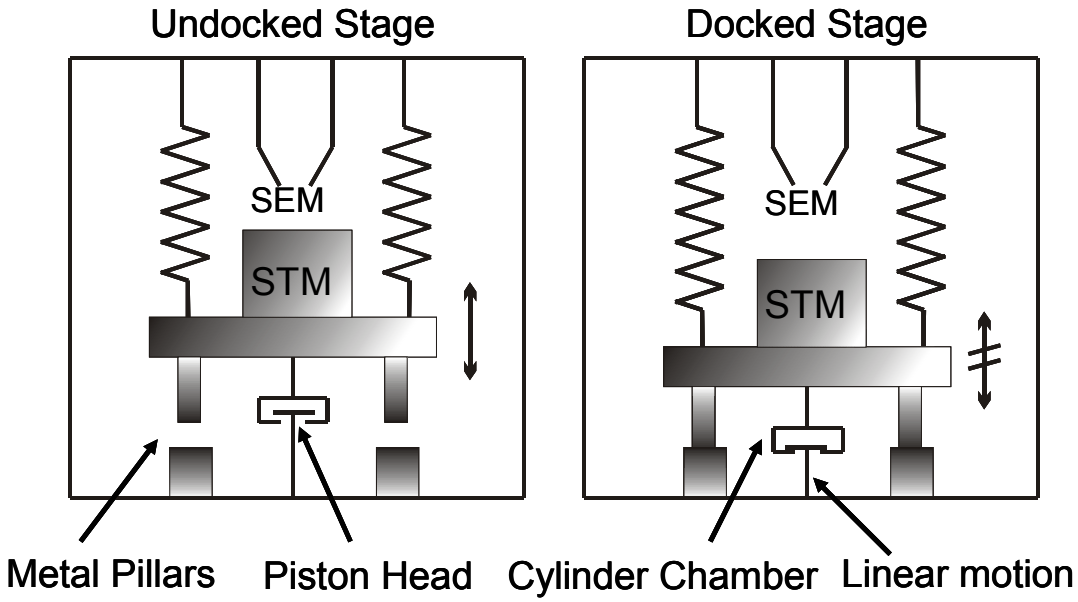

Figure 5-12: Schematic view of the docking system. The STM unit is connected to the docking system without any mechanical contacts to the frame, (left) undocked and (right) docked. The undocked position is used for STM and conductivity measurements applications while the docked position is used for SEM imaging to keep the working distance constant.

5.5.4. Vibration Isolation

Vibration isolation is especially challenging since the NWB is a large system with UHV-requirements. Nonetheless, vibration isolation is crucial not only for STM operation but also for conductivity measurements since one would like to achieve stable contact of the probes with the substrate over a long period of time.

As a first step towards vibration isolation, the main mechanical pump is isolated by coupling the rough vacuum line to a heavy concrete block. In addition, each turbo-molecular pump is connected to the rough vacuum line via flexible tubing to minimize vibration transfer. During STM operation and conductivity measurements, all turbo-molecular pumps are turned off. Additional isolation of the entire NWB from the building is achieved through a six-point

commercial active vibration system (HWL bioanalytic SYSTEMS, MOD-4). Each of the six elements senses vibrations along both horizontal and vertical directions, and a closed-loop feedback system compensates these disturbances. The isolation elements are active within the range of 0.75 – 35 Hz and passive above that. Additional vibration isolation elements are mounted inside the STM/SEM chamber.

5.5.4.1. Spring Isolation and Eddy-current Damping

The STM assembly is suspended from the chamber with custom UHV-compatible springs, fabricated using Inconel X750 wire, 0.041" diameter (Gibbs Wire and Steel Co., Inc.). The whole STM assembly (four nanomanipulators, sample box receiver and XYZ-table) is suspended on four springs, each adjusted to have similar force constants (see Figure 5-7a). The springs were electropolished to reduce their porosity and limit their outgassing in vacuum by immersion in a 3:1 mixture bath of phosphoric acid and sulfuric acid [169], and a 9V potential with respect to an array of graphite electrodes was applied for 3 minutes. Every 60 seconds, the side of the springs facing the cathode was rotated by 120° to produce a uniform surface finish. Because the surface area of a spring is large, the ohmic drop across the length of a spring often produced an insufficient surface finish at the end. A conducting backbone was therefore used to keep the spring at the same potential throughout its length. Stock removal from the process is almost negligible, the diameter of the spring was found to decrease by a mere 0.001" upon electropolishing. The measured spring constant is 110.3 $kg.s^{-2}$ for each spring used.

To further dampen vibrations in the STM stage, an eddy-current system was employed, consisting of a circular array of samarium-cobalt magnets (Magnetic Component Engineering, Inc., model S2669, 1T) with interposed conducting copper blades. The copper blades are mounted on the STM unit and the magnets are mechanically clamped on the frame (Figure 5-7a).

The samarium cobalt magnets have good corrosion resistance and high temperature stability. The Curie temperature is about 800 °C and the maximum working temperature is 320 °C, well above the requirement of our system for bakeout.

5.5.4.2. Vibration Analysis

Vibration analysis on the spring and eddy-current damping system was performed to ensure maximum effectiveness. The vibrational motion was created by simply lowering the STM stage and releasing it. The motion was recorded with a CCD camera interfaced to a computer.

This analysis enabled us to optimize the force constant of the spring system as well as the damping constant. The resonance frequency of the vibration isolation system (~1.5Hz) could be kept far from the lowest natural frequency of the nanomanipulators (~300Hz), leading to an effective vibration isolation. Figure 5-13a shows the vibrational motion of the spring system without the eddy-current damper. The resonance frequency, f_{meas}=1.9Hz, is in good agreement with the calculated resonance frequency, f_{calc}=2.1Hz. Figure 5-13b shows a plot of the motion with the eddy-current damper. The damping factor, ς, goes from 0.0419 without the eddy-current to 0.184 with the eddy-current system.

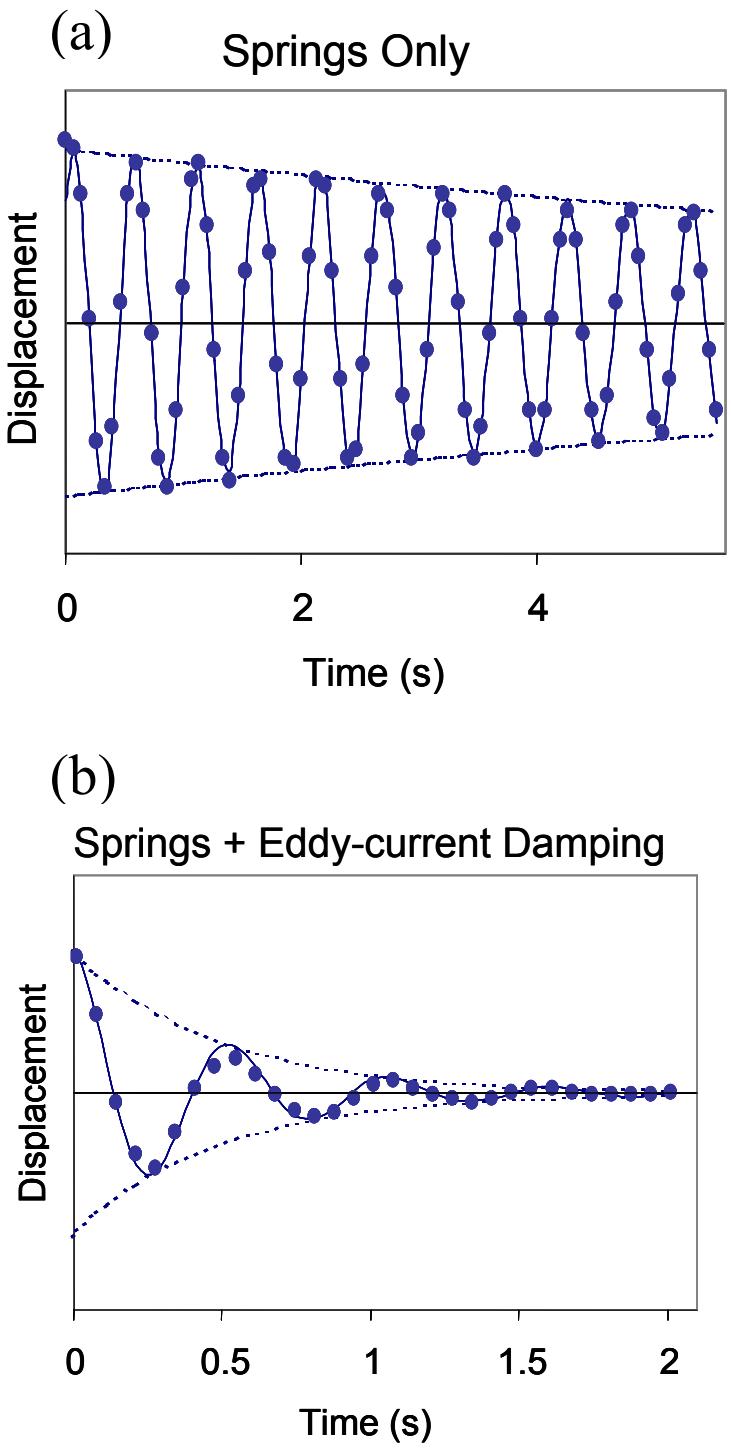

Figure 5-13: Vibration analysis showing the relaxation of the STM unit after a manual perturbation, (a) without the eddy-current damper (resonance frequency = 1.9Hz, damping factor ς=0.0419) and (b) with the Eddy-current damper (resonance frequency = 1.9Hz, damping factor ς=0.184).

5.6. Performance

The Nanoworkbench is capable of performing measurements in a variety of operational modes, some of which are illustrated below.

5.6.1. STM

The possibility of performing STM measurements distinguishes the nanoworkbench from other four probe setups. STM operation also expands the imaging capabilities of the NWB.

5.6.1.1. Sample Preparation

A highly-oriented pyrolytic graphite (HOPG) sample of 10mm x 10mm x 2mm (SPI – model 440HP-AB) is used for testing the STM capability of the nanomanipulators. The usual approach to prepare the HOPG sample for STM is to take a piece of tape, press it onto the flat surface and pull it off. The tape takes with it a thin layer of HOPG, leaving a freshly cleaved HOPG surface.

5.6.1.2. STM-operation and STM Imaging

The specifications of the Nanoworkbench STM probes differ in several important respects from typical single-probe STM instruments. First, as mentioned earlier, the manipulators are mounted at 45° from the surface plane. Therefore the Z motion of the manipulators is

established with a similar angle and is not perpendicular to the sample surface as is customary for STM systems. The SPM software incorporates a tilt correction feature to compensate for the large angle. Improved STM operation was achieved by bending the tips ~25 degrees downwards (in direction of sample) at a distance of 1 mm before the end of the tip. Secondly, the nanomanipulators themselves are less compact and rigid than most STMs. Therefore the lowest resonance frequency of the nanomanipulators is close to 300 Hz. Despite the described procedures for vibration isolation and the increase of the overall stiffness built into the STM stage, slow scanning (~1Hz) was required to acquire satisfactory STM images.

Using custom-made PtIr etched probes (Custom Probes Unlimited) we were able to reproducibly image atomic steps (see Figure 5-14) and small features with a lateral width as small as 4 nm on a cleaved HOPG surface. Similar images were acquired with all four nanomanipulators.

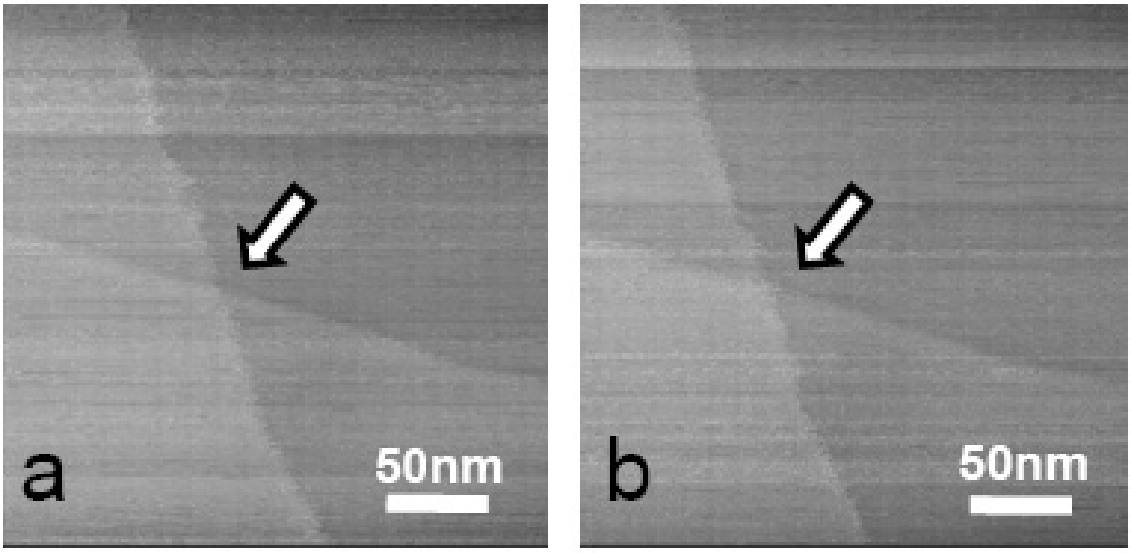

Figure 5-14: Reproducible STM imaging of atomic steps on HOPG acquired with MM3a nano-manipulator. The images were acquired consecutively. Experimental conditions for both images: 1x 10^{-8} mbar; U_{bias} = 200 mV, $I_{setpoint}$ = 0.43 nA, image size 271 x 271 nm, acquisition time per image was 260 s. The bar scale represents 50 nm.

5.6.2. Four-Point Probe

As explained in section 1.1.2 four terminal measurements have several advantages over two-terminal measurements. The nanoworkbench allows *in situ* positioning of four nanoscale contacts, allowing four probe measurements to be obtained.

5.6.2.1. Motivation

The goal of these experiments is to demonstrate operation of the NWB by performing four-point-probe conductivity measurements and to create a Field-Effect Transistor (FET) whose size and position will be determined by the spacing between the probes and their location on the surface respectively.

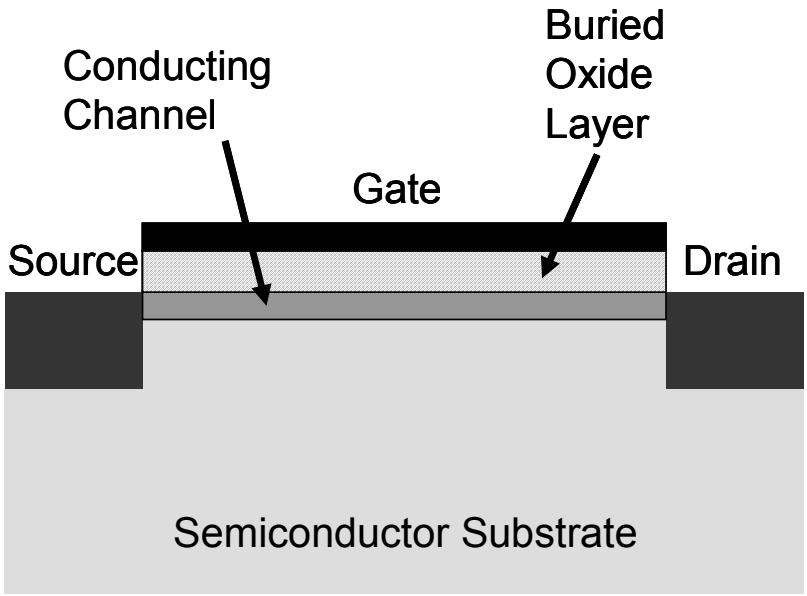

Figure 5-15: Principle of FET Operation.

An FET works by modulating an electric field inside a semiconductor material. As can be seen in the schematic of Figure 5-15, an FET is defined by three electrodes: two of them are used as Source and Drain, while the third one is a Gate electrode. It should be noted that in our case and as shown in Figure 5-15 (also see Figure 5-16b) there will be no direct connection between the gate electrode and the semiconductor material itself. The gate electrode is insulated from the semiconductor material by a thin oxide barrier. This insulating barrier acts like the dielectric layer of a capacitor, and allows gate-to-source voltage to influence the depletion region electrostatically rather than by direct connection. Additionally as can be seen in Figure 5-16b, our FET system will be composed of five electrodes: the four electrodes of the four-point probe system + the gate electrode.

5.6.2.2. Set-up and Strategy

To perform the measurements the precise placement of the probes is crucial. The following procedure is employed for positioning the four probes:

(1) The tips are brought into close proximity to the sample surface, using the UHV-SEM as a guide. The "electron shadow" of the probes in the SEM images can be used to estimate the distance between the tip and the sample.

(2) When the distance between the tip and the sample is small enough the automatic STM Z-motion coarse-approach with the feedback loop control is activated.

Steps 1 and 2 are repeated until all four tips are in tunneling contact with the surface. The spacing between the probes can be measured to an accuracy of ± 100 nm from the SEM image.

Fine positioning of the tips in tunneling contact is possible. Gentle contact is achieved between the tips and the sample surface. By changing the tunneling parameters (increase of current setpoint, decrease of bias voltage) the tunneling gap is minimized. By setting the gain of the feedback loop (SPM software) to zero, the feedback control is switched off. To prevent damage and/or interference of the operational amplifier (OPA111) all connections to the preamplifier are disabled via a switchbox. By switching an electromagnetic relay (see Figure 5-9), an electrical shortcut to the tip is established and the resistance between tip and sample can be monitored. With all four tips in electrical contact with the sample, four-probe measurements can be performed. A Keithley 6487 picoammeter/voltage source is used as a current source between the outer probes while the voltage drop between the inner probes is measured with an Agilent 34401A 6 ½ digit multimeter (input impedance >10 GOhm).

5.6.2.3. Sample preparation

Four probe experiments were performed on silicon-on-insulator (SOI) samples (Ultrasil, Inc.), which consist of an undoped Si(100) layer with a thickness of 3.5 μm, separated from a highly doped Si(100) substrate called a "handle" (410 μm-thick) by a buried oxide layer (500nm-thick). The handle is highly doped (resistivity of 1-10 Ω·cm) allowing the insulating top layer to be flash cleaned by resistive heating of the handle (see schematic of the SOI sample in Figure 5-16b). The dimensions of the crystal are 10x5x0.5 mm^3. Prior to introduction in vacuum the crystal was chemically-cleaned *ex-situ* using the following recipe: (1). 10 minutes acetone; (2). 10 minutes (H_2O_2:H_2SO_4 1:2) at 130°C [170]; (3). Standard Clean-1 at 65°C for 5 minutes (H_2O:H_2O_2:NH_4OH 5:1:1); (4). Standard Clean-2 at 65°C for 10 minutes (H_2O:H_2O_2:HCl 6:1:1)

[170,171]; and (5). Oxide etch for 15 seconds using ($HF:H_2O$ 2:100). This treatment is known to produce a hydrogen-terminated Si(100) surface free of organic contaminants [172]. The crystal was subsequently annealed in vacuum for 20 minutes at 870 K, followed by 20 minutes at 1170 K and then by a 15-second flash at 1470 K. Following this treatment the Auger spectrum reveals an intense Si peak at 92 eV and only tiny signals from carbon (272 eV) and oxygen (502 eV) (not shown). The C/Si peak-to-peak ratio of the clean sample was found to be less than 0.002, which corresponds to a C atomic fraction of 0.005 in the depth of Auger sampling.

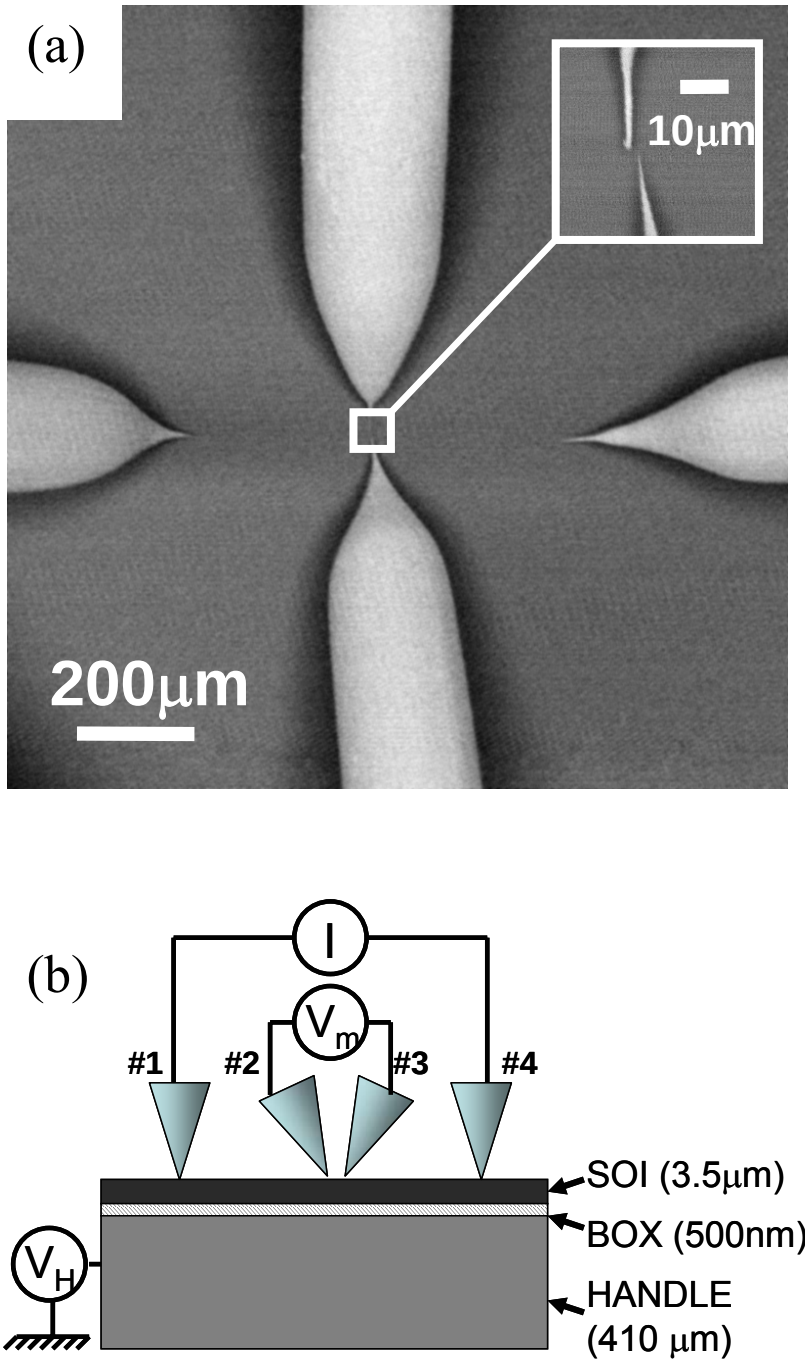

Figure 5-16: (a) SEM image showing the in-line configuration with the inner tips at a distance of 2.5 μm. The insert in the upper right corner is a magnified view of the marked area. The scale bar represents 200 μm for the overview image and 10 μm for the insert. (b) Schematic of the experimental setup.

5.6.2.4. Results

A typical experimental configuration is shown in Figure 5-16b. In a first step, all four tips were brought in contact with the clean Si(100) crystal, according to the positioning procedure described above. The four probes are arranged in a linear fashion as shown in the SEM image (Figure 5-16a). The spacing d_1 between the inner probes and d_2 between the outer probes was determined by SEM. Throughout the experiment d_1 and d_2 were maintained constant respectively at 2.0μm and 10 μm. A voltage ($V_{applied}$) was applied between the outer tips #1 and tip #4, and the resulting voltage drop between tip #2 and tip #3 ($V_{measured}$) was measured for different values of the handle voltage V_{handle}.

Figure 5-17a and Figure 5-17b summarize the resulting charactistics of the "device" formed by the SOI sample, the handle and the four probes. Figure 5-17a shows an intensity map of $V_{measured}$ as a function of V_{handle} and $V_{applied}$. The characteristics are linear for low values of V_{handle}, and become highly nonlinear at sufficiently large V_{handle}. Figure 5-17b shows a "cross-section" of Figure 5-17a for 7 values of V_{handle}: -8V, -5V, -4V, 0V, +4V, +5V and +8V. The handle voltage causes a local depletion region at the "source" and "drain" which are the outer tips #1 and #4, thus reducing the measured value of the voltage. This transition from Ohmic behavior to a highly non-linear device characteristic is typical of a field effect transistor (FET). The difference is that this FET is "roaming" because the source and drain leads are STM probes that can touch down at different locations on the sample. A roaming FET may prove useful in probing the transfer characteristics of a variety of nanoscale devices such as quantum dot-based single electron transistors. One can think for instance of moving the FET configuration at will on a surface and more specifically to surround a quantum dot. This could lead to a measure of the

contribution of the dot to charge transfer by comparison to a similar experiment performed on a dot-free zone of the sample. An extension of this type of experiments is the realization of a single electron transistor (SET) which is described in the conclusion of this dissertation.

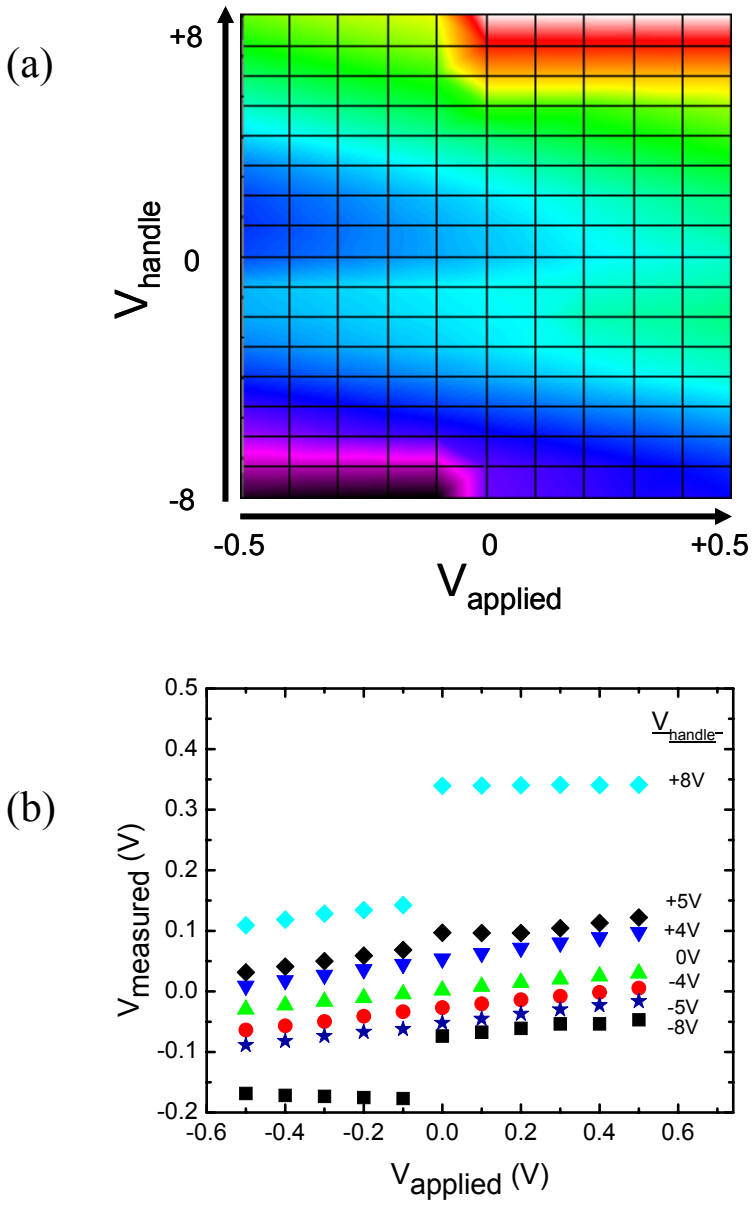

Figure 5-17: Four-point probe measurement on SOI sample. (a) Map of the voltage drop measured between the inner probes ($V_{measured}$) as a function of the voltage applied between the outer probes ($V_{applied}$) and the bias voltage on the handle (V_{handle}) and (b) Cross section of (a) for various values of V_{handle}.

5.7. Conclusion

A multiple-chamber UHV system was designed and assembled for use as a general purpose nanoworkbench. The combination of SEM and four STM nanomanipulators, along with *in situ* film growth capabilities, allows one to perform conductivity measurements down to sub-micrometer levels. We demonstrated STM imaging capability and four-point conductivity measurements leading to the formation of a localized field-effect transistor. The ability to grow nanoscale structures and to probe their properties *in situ* presents a powerful new tool for exploring the electronic behavior of nanoscale objects. Additional experiments to probe the quantum nature of ultra-small Ge islands on Si(100) are under way. These experiments will aim at creating a single-electron transistor operating at room temperature.

6. Direct Measurement of the Direction of Interface Motion in the Oxidation of Metals and Covalent Solids- Al(111) and Si(100) Oxidation with O_2 at 300 K

6.1. Abstract

Measurements of the surface electrical resistance at the oxide film-metal interface and at the oxide-film semiconductor interface have shown that the direction of the buried interface motion during oxide film growth is opposite in the two cases. During the formation of amorphous Al_2O_3 layers on Al(111) at 300 K, outward film growth occurs due to Al^{3+} ion transport from the metal into the growing oxide film. For the formation of amorphous SiO_2 layers on Si(100) at 300 K, oxygen transport occurs inwardly into the Si lattice as the oxide film forms. The surface resistance measurements have been made on atomically clean single crystals using a unique ultrahigh vacuum four-point probe STM apparatus. These probes make direct electrical contact with the surface. The direction of motion of the substrate interface during oxidation has been determined by four-point probe current/voltage measurements of surface conductivity. The inner two probes separated by 300nm act as potential probes while the outer probes, spaced 1μm apart, act as source and drain for the current. These are the first electrical measurements which directly detect the fundamentally differing oxidation mechanism of metallic and covalent solids in the thin film regime with Å sensitivity. The measurements agree with the widely accepted Mott-Cabrera model of metal oxidation which is based on kinetic measurements of the rate of oxidation. Kinetic measurements provide only *indirect* evidence about the direction of interface motion during oxidation.

6.2. Introduction

The formation of passive thin oxide films on surfaces of materials provides a natural protection mechanism of great importance in the prevention of metal corrosion [173-176] and for the production of dielectric films needed for semiconductor device fabrication[177,178]. Even though the formation of thin (< 30 Å) oxide films has been studied for over 100 years, fundamental questions about the mechanism of oxide film growth still exist, as suggested by the current activity in research on this topic using modern methods of surface science[179-191].

A basic issue concerns the direction of interface motion at the surfaces of metals and covalent solids when a thin oxide film forms. The theory of Mott and Cabrera (MC) [10,14,192] extending and clarifying earlier work by Wagner[193], showed that an electric field, naturally produced across a growing thin *ionic* oxide film, determines the rate of oxidation by controlling the rate of diffusion of metal cations from the metal to the outer surface of the oxide film. Here metal cations combine with oxide ions. In the framework of this model, oxide film growth should occur in an outward direction from the metallic interface. Electron transfer from the metal to the oxide film, followed by tunneling between electron trap sites in the oxide to the outer surface of the oxide film, provides a counter current to metal ion diffusion through the oxide film during thin film growth[175]. This mechanism explains the observed oxide growth kinetics and the approach to a limiting film thickness in homogeneous oxide thin film growth on metals. The MC mechanism has been modified to some extent to consider inhomogeneous oxide film growth due to nucleation of oxide clusters for some systems[174], and to consider the role of defects on the metal surface[179] and in the oxide film[175,192]. The influence of externally applied electric fields on the rate of oxide film growth on metals supports the MC theory[194]. This large body of knowledge

is however not based upon *direct* physical evidence detecting the motion of the metal-oxide interface during oxide film growth.

In contrast to ionic thin film growth, the growth of thin non-ionic oxide films on covalent solids has been postulated to proceed by oxygen penetration into the covalent solid [11]. A recent study, involving optical and Auger spectroscopy measurements of oxygen adsorption and oxidation processes on Si(100), suggests that oxidation at the silicon surface occurs initially and is then followed by continued oxidation of silicon in the bulk [187]. Again, these studies do not provide *direct* physical evidence measuring the motion of the semiconductor-oxide interface during oxide film growth.

This paper reports high sensitivity electrical measurements of the motion of the interface between substrate atoms and the oxide film formed on a metallic and on a covalently-bonded solid. Both solids are known to produce homogeneous oxide films beyond monolayer oxidation [191,195]. We employ a special ultrahigh vacuum four-point probe STM apparatus[196]. Here four independently movable STM tips are used to make current/voltage measurements of surface resistivity over a lateral (x,y) distance, d (between the inner probes) of 300nm. The apparatus allows the surface of the solid to be located in the z coordinate to Å accuracy using the STM feedback prior to electrical contact before and during oxidation. The measurements show that Al(111), during oxidation by O_2(g) at 300 K, retains its metallic conductivity at the interface position, whereas Si(100) becomes less conductive. The measurements directly show therefore that the oxidation of a representative metal, Al, occurs by outward growth of the oxide film from the initial surface location. In contrast, the oxidation of a non-metal, silicon, takes place by inward motion of the buried interface. The difference between outward film growth (ionic oxide) and inward film growth (non-ionic oxide) is schematically shown in Figure 6-1a and 1b.

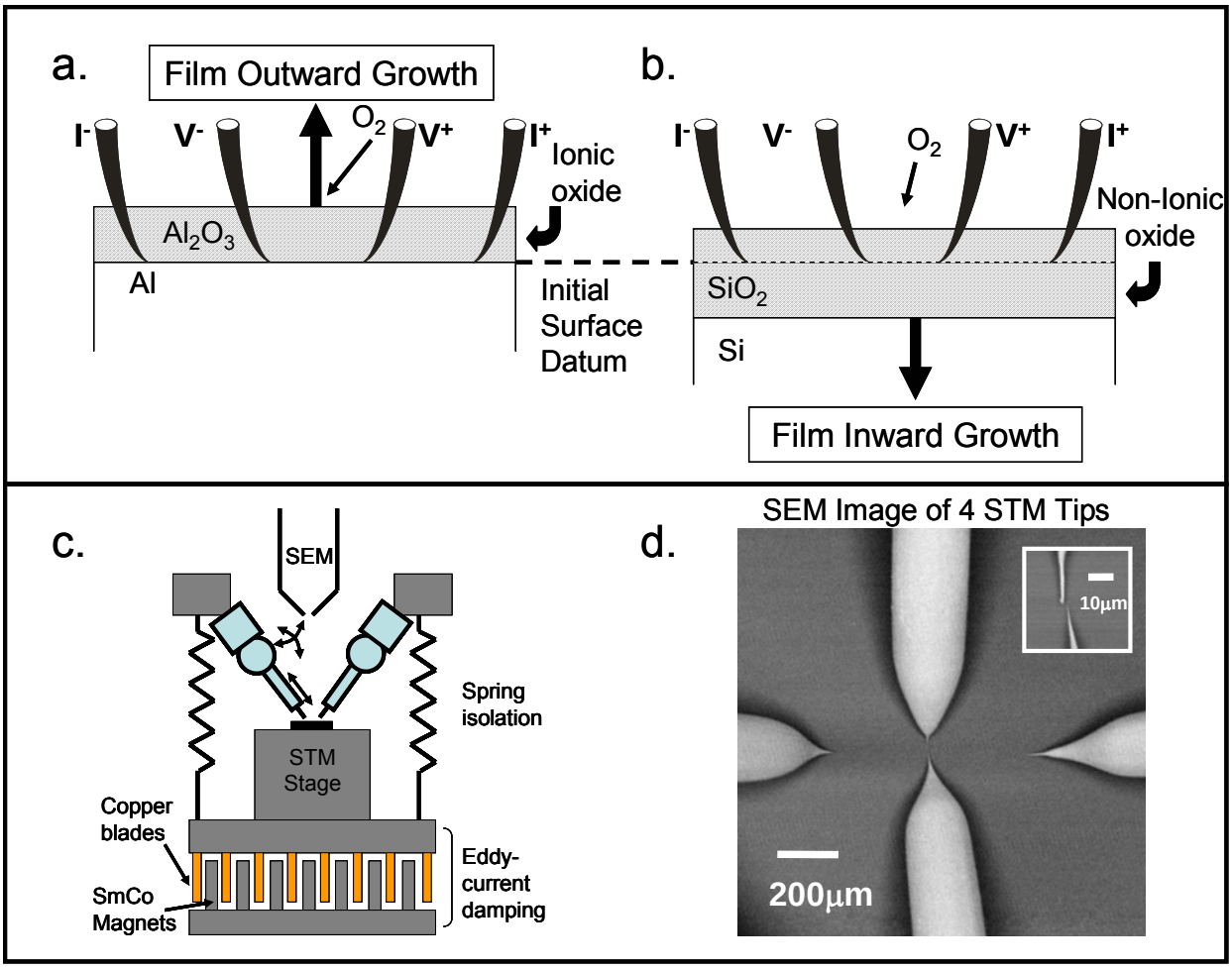

Figure 6-1: Schematic of electrical measurement of oxide film growth direction on (a) Al(111) and (b) Si(100) crystals. (c) Schematic of the multiple tip STM – SEM chamber for electrical measurements. The STM stage is suspended on springs and is further vibrationally isolated via an eddy-current damping system; (d) SEM image of the 4 STM probes during approach to the Si(100) crystal surface.

6.3. Experimental Methods

The experiments were conducted in an ultrahigh vacuum (UHV) system operating at a base pressure of 4×10^{-10} mbar [196]. The UHV-system is composed of chambers interconnected with each other via a transfer system: (1) a load-lock chamber for fast entry of samples and probes; (2) a chemical preparation and analysis chamber equipped with standard surface science

tools such as Auger Electron Spectroscopy (AES), Low Energy Electron Diffraction (LEED), X-ray Photoelectron Spectroscopy (XPS), Quadrupole Mass Spectrometry (QMS) and a gas handling system; and (3) a unique chamber combining four STM probes which are imaged with a scanning electron microscope for four-point-probe conductivity measurements at sub-micrometer tip separation. As shown in Figure 6-1c, the STM stage is suspended on springs and is further isolated from external vibrations via an eddy-current damping system. In addition, the entire UHV system rests on an active vibration isolation system. The four nanomanipulators, oriented at 45º from the normal, and at 90 º from each other, electrically probe a small region on the surface of a material of interest. They are guided by a scanning electron microscope (SEM) which images both the surface and the probes as shown in Figure 6-1d. It should be noted that the nanomanipulators are controlled independently from each other. Four-point-probe conductivity measurements are performed in the following way: once the atomically clean sample is transferred to the STM/SEM chamber, all four probes are caused to approach to the surface using the STM feedback loop control. The SEM is used to guide the probes with respect to each other and to determine the spacing between the probes. Once all four tips are in tunneling contact, the tunneling current set-point is increased to its maximum value allowing a gentle contact to be achieved between the probes and the sample and little deformation of the sample occurs[197]. Details of the calculations of the indentation created by the hertzian contact of a PtIr probe with the Al(111) surface are shown in the Appendix. Conductivity measurements can then be performed. A current is applied between the outer probes while the potential drop is measured between the inner probes (with an input impedance > 10 GOhm to prevent any current flow between the inner probes). Remarkable stability is achieved between the probes and the surface

of the sample as will be demonstrated later in the paper. Thus the potential probes are able to electrically locate the sample surface to very high accuracy.

An Al(111) crystal and a Si(100) crystal were used for these experiments. The Al(111) single crystal (10 x 5 x 1mm^3) was mechanically polished to produce the (111) surface plane orientation (±0.5º). The crystal was mounted onto the sample holder by Ta wires passing through slots on the crystal face. It should be noted that the Ta wires do not protrude above the edge of the crystal surface to avoid Ta contamination of the Al crystal during sputtering. In UHV, the Al crystal was cleaned by Ar sputtering cycles (U_p = 1.5kV, I_p=3.2μA) for 1h and radiatively annealed at 800K for 5 min. The temperature was measured with a type K thermocouple attached to the crystal. The sputter and annealing cycles were repeated until no oxygen or carbon were detected by AES. The Si(100) crystal (n-type, P doped, Umicore) was 10 x 5 x 0.5 mm^3, with a resistivity of 100 ohm-cm and was polished on both faces. The crystal was resistively heated using non-interacting Ta contacts [198]. Prior to introduction in vacuum the Si crystal was ozone-cleaned for 20 min and HF-cleaned for 30s (using a HF:H_2O 2:100 solution). The crystal was subsequently annealed in vacuum, 20min at 870K, followed by 20min at 1170K and then by a 15s flash at 1470K. Following this treatment the Auger spectrum reveals an intense Si peak at 92eV and the absence of both carbon (272eV) and oxygen (502eV). The C/Si peak-to-peak ratio of the clean crystal was found to be less than 0.002, which corresponds to a C atomic fraction of 0.005 in the depth of the Auger sampling.

After UHV-cleaning, the crystals were rapidly transferred in UHV to the STM/SEM chamber where four-point-probe conductivity measurements were performed. In separate experiments molecular oxygen (O_2) or nitrous oxide (N_2O) is dosed sequentially for exposures from 0.1L up to more than 20,000 L [1L=10^{-6} Torr s exposure]. After each dose, a four-point

probe measurement was performed. It should be noted that the SEM was turned off throughout the dosing / measurement process and that the four probes were not moved until completion of the experiment.

6.4. Results and Discussion

Figure 6-2 shows the surface resistance measurements made during the oxidation of Al(111). The very low resistance of the clean Al(111) surface remains constant to within 2% up to an O_2 exposure of 20,000 L, indicating that the tip contact with metal is retained throughout the growth of the oxide layer. The insets of Figure 6-2 show the Auger spectrum of the Al(111) surface before (left) and after (right) oxidation. The conversion of the Al^0 feature near 68eV from a spectrum characteristic of metal to that of oxide is evident, as well as the development of a strong O(KLL) feature at 502eV. Other studies indicate that the thickness of the Al_2O_3 layer produced by a 20,000 L O_2 exposure at 300 K is near 20-30 Å [199].

In order to determine that the surface resistivity measurements can detect an Al_2O_3 thin film, an additional experiment was performed. Following the oxidation the potential leads were laterally translated by 25Å from their metal contact position, placing them on the surface of the surrounding oxide film. As shown in Figure 6-3, translation of the potential probe results in a $\sim 10^6$ fold increase in measured resistance. Complete separation of the potential leads from the oxide surface results in infinite resistance.

Figure 6-4 shows the surface resistivity for Si(100) during oxidation at 300 K up to an O_2(g) exposure of 20,000 L. A 55 % increase of resistance is observed at the final O_2 exposure.

The smoothness of the data indicates that tip contact is maintained throughout the experiment. The insets of Figure 6-4 show the Auger spectrum of the clean (left) and the oxygen-covered (right) Si(100) surface. The appearance of the O(KLL) feature at 502eV and the change in the Si(LVV) silicon lineshape indicates that extensive silicon oxidation has occurred. Other studies on Si(100) indicate that a 20,000 L O_2(g) exposure at 300 K will produce an oxide layer of ~ 2 ML thickness [187].

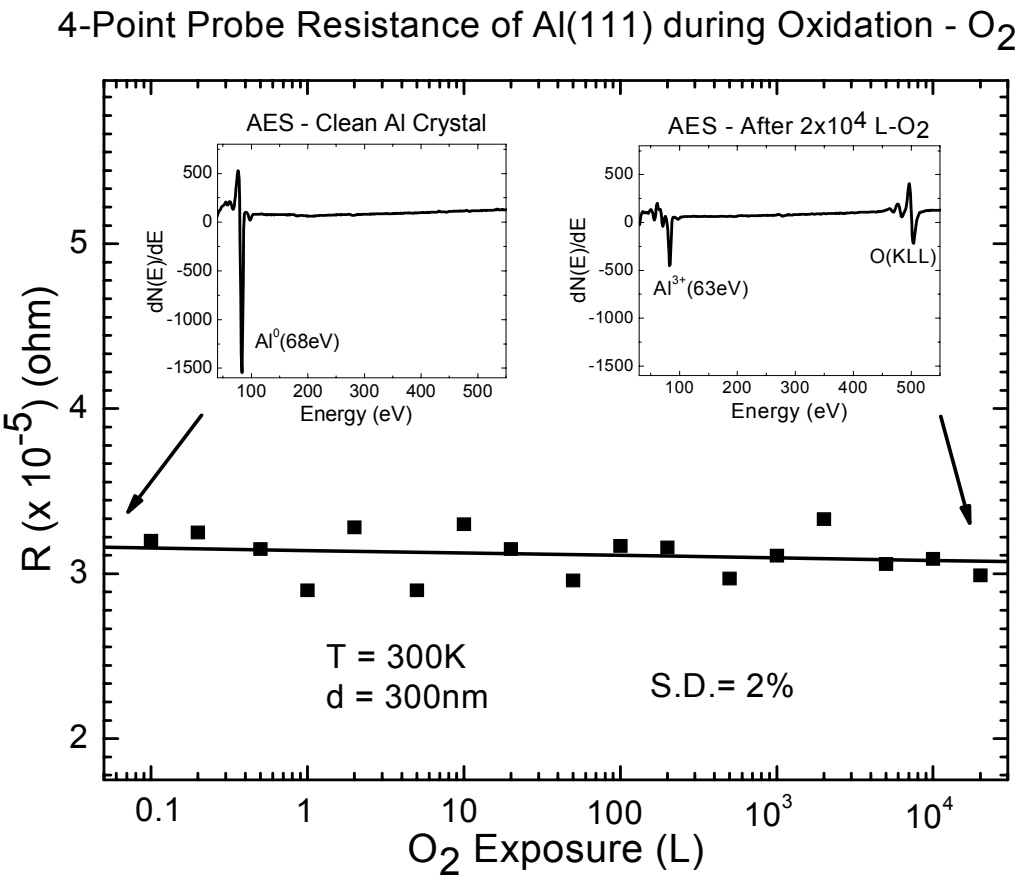

Figure 6-2: Four-point probe resistance measurement of Al(111) during oxidation with O_2 at 300K. The O_2 exposure is sequentially varied from 0.1L up to 20,000L. Left Inset: Auger spectrum of clean Al(111) before exposure. The sample is atomically clean; Right Inset: Auger spectrum of Al(111) after exposure to 20,000L-O_2 at 300K, producing 20-30Å Al_2O_3 film.

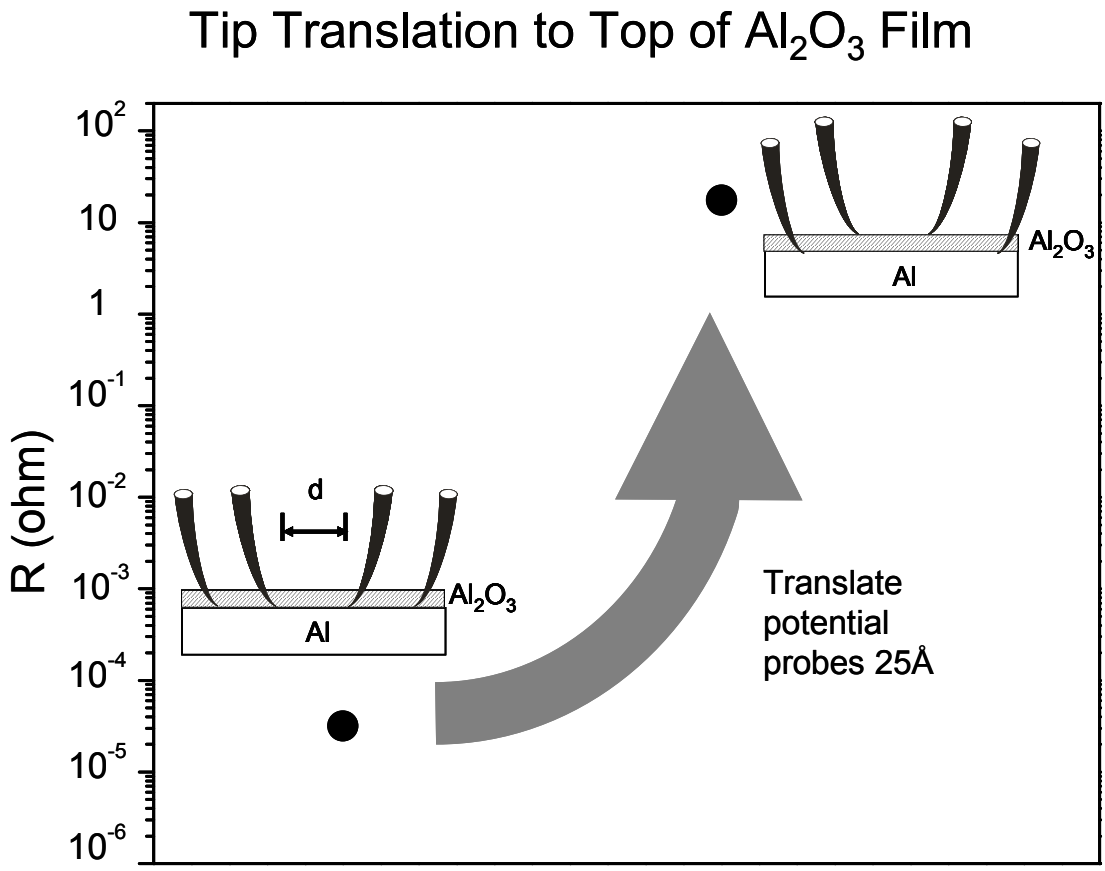

Figure 6-3: Evolution of the measured resistance on the oxidized Al crystal as the inner probes are laterally translated 25Å to the top of the Al_2O_3 film. The measured resistance increases by 6 orders of magnitude.

A 4-point probe experiment was performed on a clean Si(100) surface over a period of 60 minutes to check for the stability and reliability of the measurements, with data acquisition every 10 minutes. The data exhibit a standard deviation of less than 0.5% in measured resistance (see Figure 6-5). These control measurements, along with the smoothness of the resistance measurements in all of the oxidation experiments indicate that mechanical vibration or thermally induced motions do not occur at the tip / substrate interface during the experiments.

In order to indirectly determine the sensitivity of the surface resistance measurements to oxygen adsorption on Si(100), studies were done using N_2O(g) as the oxidizing agent. It is known that N_2O produces only one monolayer of oxide in a process which involves reaction only with surface Si dangling bonds at 300 K[187]. Figure 6-6 shows the surface resistance for Si(100) during exposure to N_2O(g). The first observable increase in resistance occurs at about 10L N_2O(g) exposure, and by 20,000 L N_2O(g) exposure, a 0.2 % increase in surface resistivity has occurred. Thus the electrical measurements on Si(100) have sub-monolayer oxide sensitivity.

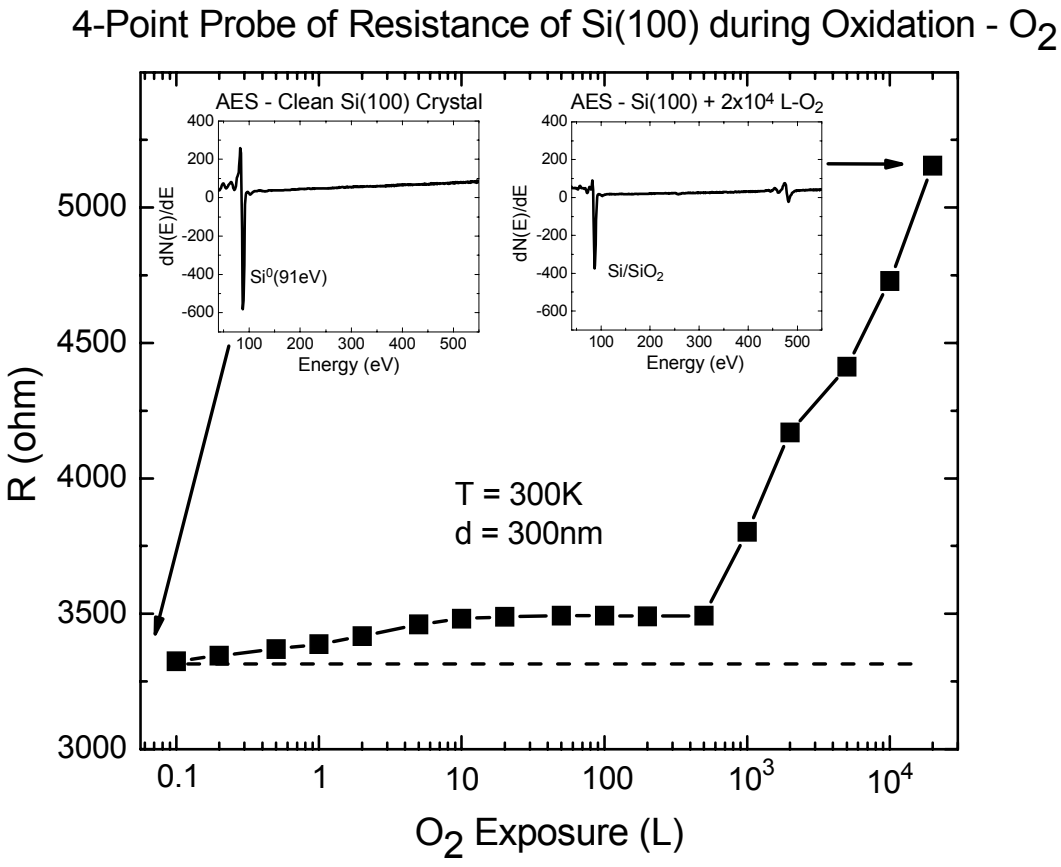

Figure 6-4: Four-point probe resistance measurement of Si(100) during oxidation with O_2 at 300K. The O_2 exposure is sequentially varied from 0.1L up to 20,000L. Left Inset: Auger spectrum of Si(100) before exposure. Before exposure, the sample is atomically clean; Right Inset: Auger spectrum of Si(100) after exposure to 20,000L-O_2 at 300K. Several monolayers of SiO_2 are produced.

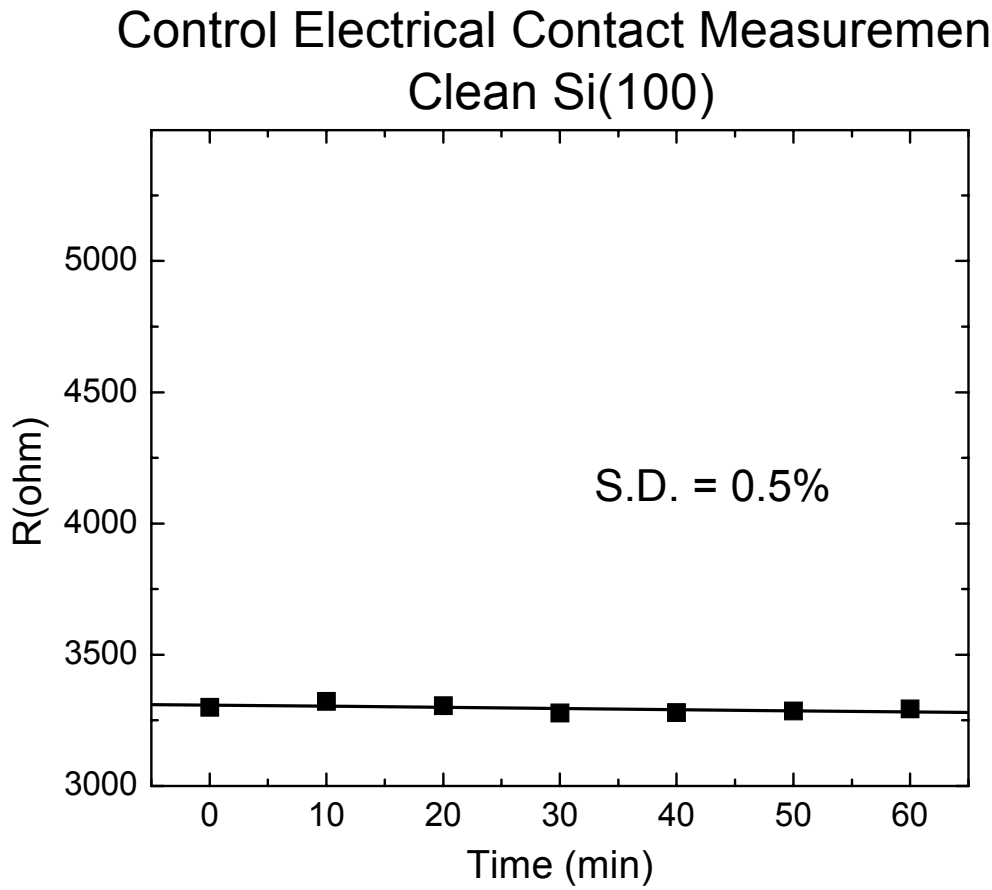

Figure 6-5: Control electrical contact measurement on a clean Si(100) surface. Over a period of 60 minutes in UHV, the standard deviation for the resistance measured is less than 0.5%.

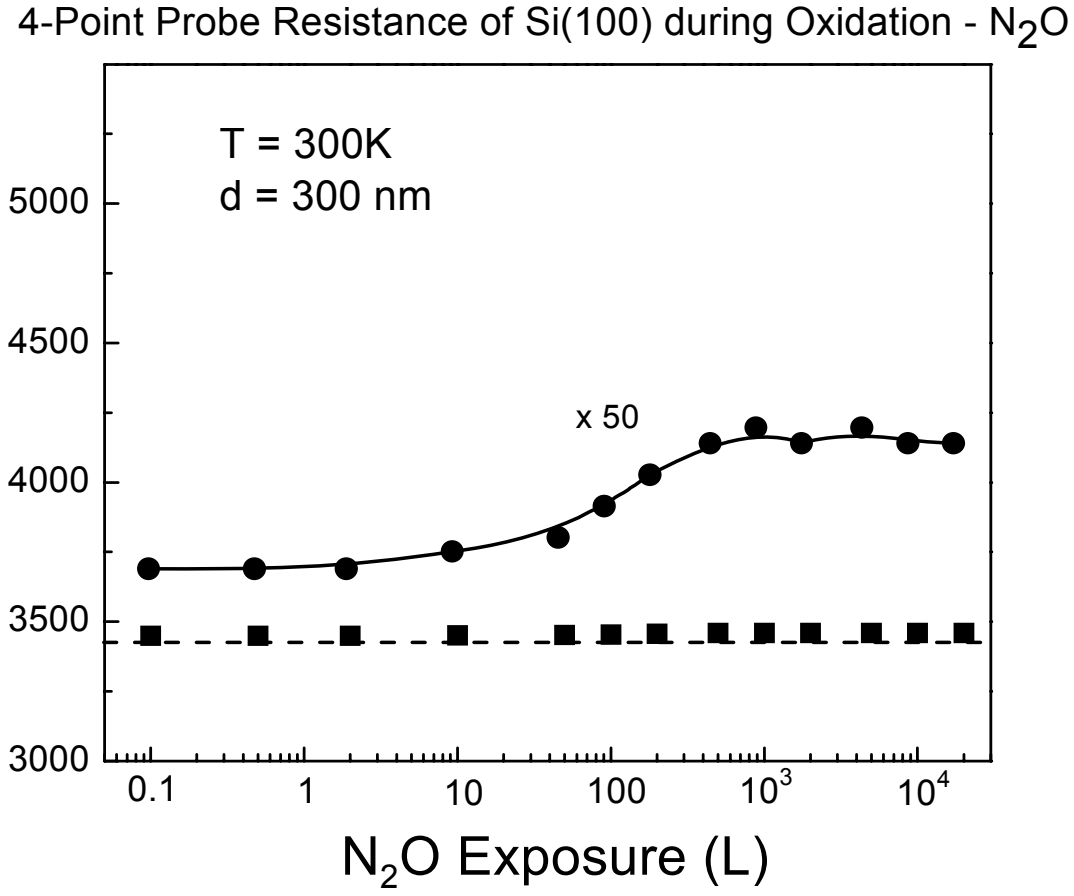

Figure 6-6: Four-point probe resistance measurement of Si(100) during oxidation to only 1 ML of oxide thickness with N_2O at 300K. The N_2O exposure is sequentially varied from 0.1L up to 20,000L.

Figure 6-1 schematically summarizes the basic findings of this research. In Figure 6-1a it is shown that the oxidation of Al(111) takes place by ***outward growth of the oxide film***, and that electrical contact is therefore maintained between the potential leads and the metallic surface throughout the film growth process, as indicated by the almost constant low resistance measured. The removal of Al atoms (as Al^{3+} ions) by diffusion to the outer oxide surface must be accompanied by diffusion of Al metal atoms from the bulk metal into the metal atom vacancies

so produced at the Al/Al_2O_3 interface, maintaining the location of the metal-oxide boundary. Figure 6-1b schematically shows that the oxidation of silicon occurs by ***inward growth of the buried oxide / silicon interface*** as diffusing oxygen species attack Si-Si back bonds under the crystal surface. In this case the electrical resistance measured between the potential leads increases, even in the sub-monolayer regime of oxide film thickness. Both oxide films are less dense than the metal or semiconductor on which they grow contributing to outward growth of the *outer* surface of each oxide film.

These findings are in agreement with expectations for the oxidation of a metal, where kinetic fits have been made of the oxidation rate to the Mott-Cabrera and related models involving rate-controlling metal cation diffusion through the oxide film (under the influence of a naturally occurring negative-outward electrical field). These measurements are also in agreement with expectations from surface science studies of the oxidation of covalently-bonded silicon, and the formation of a non-ionic oxide film on silicon. The distinctive difference in the direction of the buried oxide / substrate interface motion observed during the oxidation of Al and Si will probably apply to other metals and covalent solids.

7. Materials Architecture for Quantum Computation

The next three sections describe effort towards the fabrication of materials for constructing a quantum information processor using ferroelectrically coupled Ge/Si quantum dots.

In this system, shown schematically in Figure 7-1, the spin of single electrons forms the fundamental qubits. Small (<10 nm diameter) Ge quantum dots will be engineered, allowing optical excitation of spin polarized electrons in Si. Eventually, an epitaxial ferroelectric film will be grown using oxide-Molecular Beam Epitaxy (MBE). The use of the system is summarized below:

- Use electron spins in group-IV semiconductors as qubits;
- Spin-polarize electrons optically using direct band gap quantum dots;
- Process quantum information using the static and dynamic polarization of a ferroelectric thin film;
- Measure the final state using optical and transport methods.

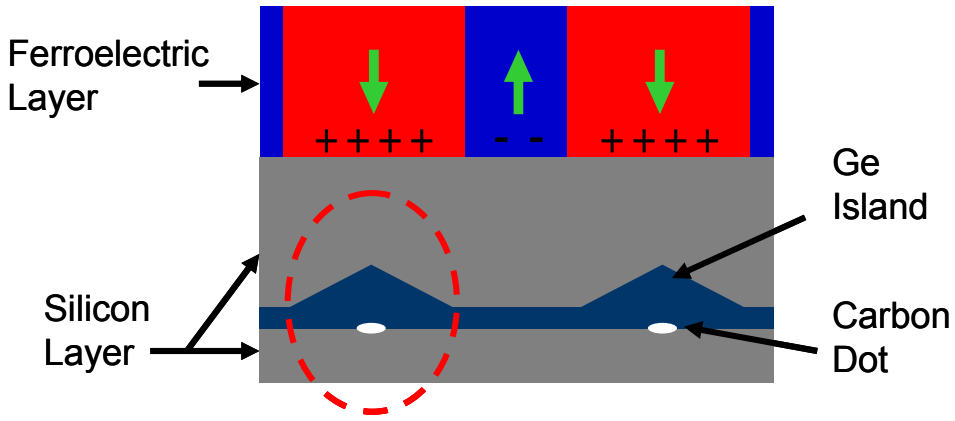

Figure 7-1: Schematic of the quantum computation system. Sub-10nm Ge islands form a matrix on Si(100) substrate. A ferroelectric layer caps the islands.

Three important subsystems make up the physical system being proposed for electron spin-based quantum information processing. First, it is imperative to create a spatially controlled array of small (<10 nm diameter) Ge quantum dots on Si. Second is the ferroelectric thin film, which will likely be a short-period superlattice or graded composition of $BaTiO_3$ and $SrTiO_3$. The third subsystem is the interface between the semiconductor system (in this case the Si capping layer) and an epitaxial ferroelectric thin film. Without careful attention to the interface, it will be difficult to ensure a low density of interface traps, and to control the band offsets between the ferroelectric and semiconductor. All three subsystems are essential for the proper performance of the proposed device.

The scope of the project described in this dissertation is limited to the Si/Ge system.

Naturally formed Ge/Si quantum dots grown by self-assembly using the Stranski-Krastanov mode have a range of diameters that start at approximately 20 nm and increase to as large as 50-100nm. These quantum dots are *not useful* for quantum computing applications, because they are too large to have appreciable direct optical transitions. Formation of smaller Ge islands by pre-adsorption of carbon on the silicon surface has been demonstrated to yield quantum dots with strong luminescence and signatures of direct optical transitions[200,201] but arrays of small Ge islands have yet to be created with perfect control over both the diameter D of the Ge island and the spacing L between neighboring islands as shown in Figure 7-2. As was presented in section 4.3, all methods used to pattern Ge islands on Si(100) to date make use of the Stranski-Krastanov growth mode and the dots are too large and their spacing sometimes

uneven (see Table 4-1 for a summary). The creation of specific quantum dot patterns requires the ability to initiate growth on specified locations on the substrate.

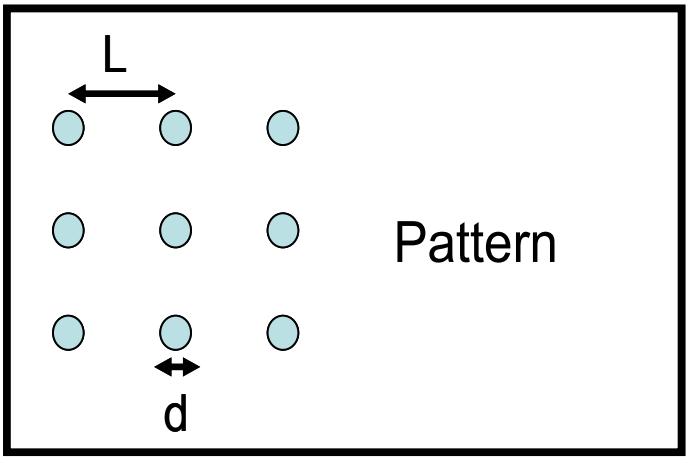

Figure 7-2: Schematic of an array of Ge islands. The array is defined by two parameters: the diameter D of an island and the spacing L between neighboring islands.

We developed an approach which will promote the nucleation of Ge islands via a Volmer-Weber growth mode. This approach is based on the use of carbon as a precursor to Ge deposition. We propose to use this "carbon effect" by creating carbon templates on Si(100) by electron-beam induced deposition. Upon annealing in UHV, these carbon templates will turn into SiC dots which will act as nucleation centers for subsequent Ge deposition.

In section 8, we study the electron-beam-induced deposition (EBID) process in a UHV-environment using ethylene as a precursor molecule. The evolution of the carbon deposit to produce SiC is studied as a function of temperature by AES, XPS and TPD. Comparison with a classical CVD deposition process will also be provided.

In section 9, we will describe the EBID-process applied to the formation of a carbon template composed of ultra-small carbon dots on Si(100).

This carbon dots template will serve as nucleation center for the subsequent deposition of Ge and the formation of sub-10nm Ge islands as reported in section 10.

8. Electron-Beam Induced Deposition of Carbon Films on Si(100) using Chemisorbed Ethylene as a Precursor Molecule

8.1. Abstract

We studied the electron-beam-induced deposition of carbon on Si(100) at room temperature. Ethylene molecules dosed from the background were adsorbed on the surface and decomposed by an electron-beam. The chemical properties and structure of the resulting carbon film, as well as its evolution with the dose of ethylene and annealing temperature after dosing, were investigated by Auger Electron Spectroscopy (AES) (line-shape analysis), by X-ray Photoelectron Spectroscopy (XPS) and by Temperature-Programmed Desorption (TPD). Additionally, the amorphous-like hydrogenated carbon structure obtained after electron-beam-induced deposition (EBID) converted completely into SiC upon annealing to ~ 1150 K as evidenced by the shift of the Si(2p) plasmon loss peak and the C(1s) peak. We also show that C-H bonds in ethylene are cracked by electron bombardment and that some of the hydrogen atoms produced from cracking are captured. The EBID of carbon was also compared with the chemical vapor deposition of ethylene on Si(100) in the absence of an electron-beam and a more stable carbon structure can be formed by EBID. It is postulated that EBID deposition produces an amorphous hydrogenated film which contains a high fraction of multiple carbon-carbon bonds, compared to films made by thermal decomposition of the ethylene precursor. This leads to a higher conversion temperature to SiC.

8.2. Introduction

It is well known from previous studies[202-205] that ethylene chemisorbs on Si(100) dimer sites by forming a di-σ $C_2H_4 - Si_2$ complex. The existence of this surface complex is supported by high-resolution electron energy loss spectroscopy (HREELS) investigations[206,207], as well as by theoretical studies[208,209]. Under such conditions chemisorbed ethylene desorbs unimolecularly from the Si(100) surface near 600K, with less than 5% of the monolayer undergoing dissociation[205,210]. Clemen *et al.* [205] found that the activation energy for C_2H_4 desorption is only 38 kcal/mol. Therefore because the low desorption activation energy allows C_2H_4 to desorb prior to significant dissociation, the formation of significant carbon deposit by C_2H_4 decomposition does not occur.

Electron-Beam-Induced Deposition (EBID) and dissociation is a well-known process[211-217]. As early as 1973, Joyce and Neave studied the electron-beam – adsorbate interactions on silicon surfaces[218] and later, Klauber *et al.* investigated the production of NH_2 species from NH_3 molecules adsorbed on Ni(100) by electron irradiation[219]. Typically, adsorbed molecules are dissociated by an electronic excitation process. Molecular fragments are produced which may bind to the surface. In the work to be reported here, EBID carbon-film formation using ethylene dosed from the background as a precursor molecule was investigated by Auger Electron Spectroscopy (AES) and Auger line-shape analysis[220,221] and by X-ray Photoelectron Spectroscopy (XPS) as well as by Temperature-Programmed Desorption (TPD). Similar studies were performed with carbon films grown without the aid of electronic excitation by Chemical Vapor Deposition (CVD). As we will show, the carbon products differ for the two processes.

8.3. Experimental Methods

Experiments were performed in an ultrahigh vacuum system with a base pressure of ~ 5 10^{-10} mbar. As shown in Figure 5-3, the system contains a Perkin-Elmer Cylindrical Mirror Analyzer for Auger Electron Spectroscopy (AES model 10-155), a hemispherical Leybold-Heraeus EA-10 electron analyzer combined with a dual Mg/Al anode x-ray source, a UTI-100C quadrupole mass spectrometer, a reverse view LEED analyzer and a gas dosing system.

The Si(100) crystal (p-type, boron-doped) was 10x5x0.5 mm^3, with a resistivity of 0.05Ω·cm (Virginia Semiconductor) and was polished on both faces. The crystal was resistively heated using non-interacting Ta contacts[164]. We found using a IR-pyrometer that this method provides a rather uniform temperature, with a temperature difference across the sample of less than 20 K at 1400 K.

Prior to introduction in vacuum the crystal was chemically-cleaned *ex-situ* using the following recipe: (1). 10 minutes acetone; (2). 10 minutes (H_2O_2:H_2SO_4 1:2) at 130°C [170]; (3). Standard Clean-1 at 65°C for 5 minutes (H_2O:H_2O_2:NH_4OH 5:1:1); (4). Standard Clean-2 at 65°C for 10 minutes (H_2O:H_2O_2:HCl 6:1:1)[171,222]; and (5). Oxide etch for 15 seconds using (HF:H_2O 2:100). This treatment is known to produce a hydrogen-terminated Si(100) surface free of organic contaminants[172]. The crystal was subsequently annealed in vacuum, 20 minutes at 870 K, followed by 20 minutes at 1170 K and then by a 15 second flash at 1470 K. Following this treatment the Auger spectrum (see Figure 8-1) reveals an intense Si peak at 92 eV and the absence of both carbon (272 eV) and oxygen (502 eV) (not shown). The C/Si peak-to-peak ratio of the clean crystal was found to be less than 0.002, which corresponds to a C atomic fraction of 0.005 in the depth of Auger sampling. The inset of Figure 8-1 shows the C(1s) and Si(2p) XPS

peaks for the clean crystal. The Si(2p) plasmon loss peak is at -17.3eV measured from the Si(2p) peak.

Ethylene (purity 99.7%) was dosed into the system using a variable leak valve. An uncalibrated Bayard-Alpert gauge was used to monitor the ethylene pressure. The temperature of the crystal was measured with an infrared pyrometer.

Using ethylene as a precursor molecule, two different sources of electrons for the electron-beam induced carbon deposition were employed: (1) the electron-beam from the Auger system, with an incident energy of 2 keV and a beam diameter of ~300 μm; and (2) a hot tungsten filament at 2000 K positioned 5 cm away from the crystal. For the experiments with the hot tungsten filament the Si(100) crystal was positively biased at +400 V. This second method was used to create a carbon film on the entire front face of the crystal. In all experiments with ethylene gas as a source of carbon, the pressure of 1 x 10^{-7} mbar is equivalent to an electron mean free path of ~100 m. Thus essentially the entire EBID process must occur with molecules of C_2H_4 that are adsorbed on the surface, increasing the ethylene lifetime and density within the electron-beam to levels when useful numbers become dissociated by the beam. The current densities for the electron-beam are 5.7 x 10^{-2} C/cm^2·s (Auger electron-beam) and 4 x 10^{-4} C/cm^2·s (hot W filament).

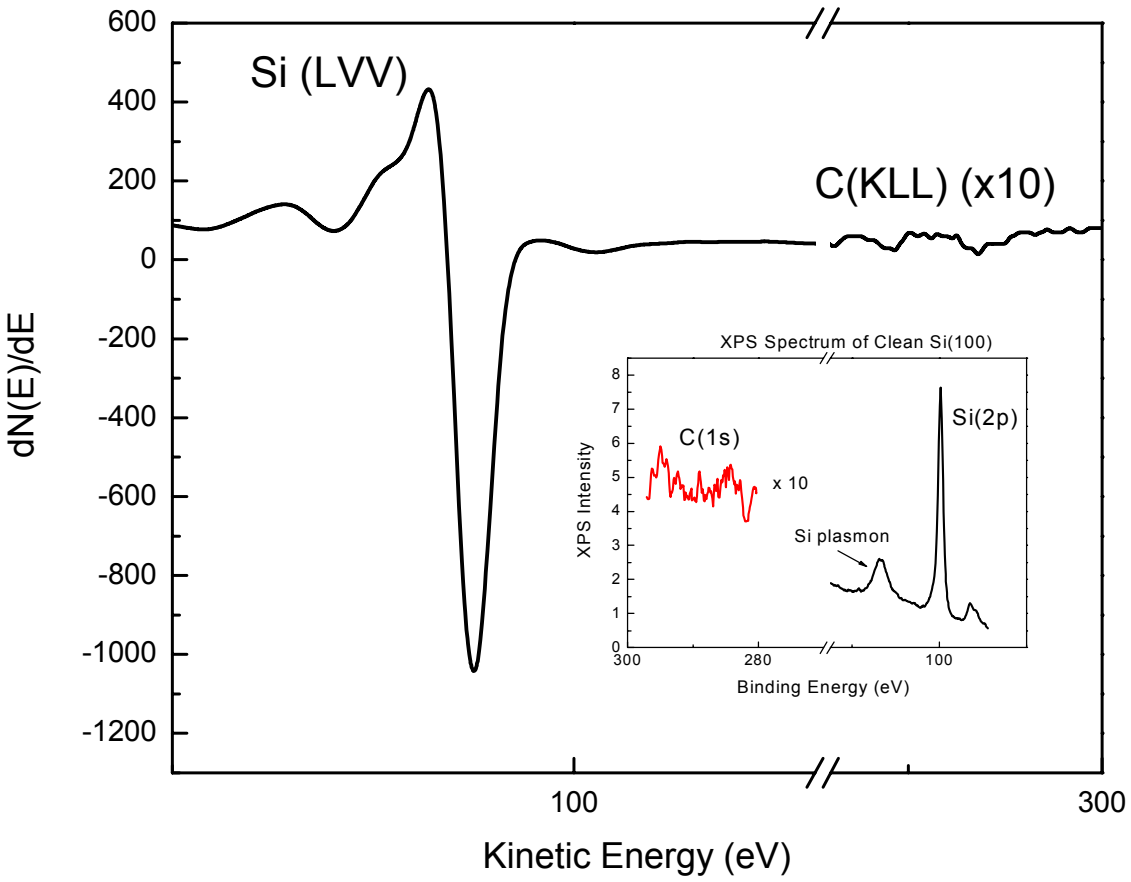

Figure 8-1: Auger spectrum of clean Si(100) showing the Si(LVV) and C(KLL) regions. *Inset*: XPS spectra of C(1s) and Si(2p) regions.

8.4. Results

8.4.1. Auger Spectroscopy Studies of Carbon Deposition by Electron-Beam-Induced Deposition (EBID)

The Auger intensity and lineshape of the C(KLL) peak (272eV) as well as the intensity of the Si(LVV) peak (92eV) were measured as a function of the ethylene dose during EBID. Figure 8-2 shows the evolution of the C/Si Auger ratio as a function of both the electron fluence on the sample and the background pressure of the ethylene precursor molecules during EBID. The C/Si

ratios are calculated as the ratio of the peak-to-peak height of the carbon C(KLL) peak and the silicon Si(LVV) peak. Regardless of the background pressure one can distinguish two regimes for the evolution of the C/Si ratio. For electron fluences smaller than 200 x 10^{+18} cm^{-2} the C/Si Auger ratio increases very fast. This can possibly be attributed to the growth of carbon on top of silicon. For electron fluences larger than 200 x 10^{+18} cm^{-2} the C/Si Auger ratio increases linearly at a lower rate. This steady behavior can be attributed to the growth of carbon on an already-formed carbon deposit. Figure 8-3 shows the evolution of the carbon C(KLL) peak shape for dosing levels between 1.75 x 10^{+15} molecules/cm^2 and 1.40 x 10^{+17} molecules/cm^2. Throughout the dosing step the carbon peak shape is characteristic of an amorphous carbon layer growing on the surface [223]. It should be noted that as shown in Figure 8-4 the carbon electronic character is invariant during EBID. In Figure 8-4, we define two parameters *a* and *b*, characteristic of the amorphous carbon Auger peak. The evolution of *a* vs. *–b* is plotted on the right side of Figure 8-4 as the dose of ethylene on the sample is increased. The linear evolution (constant *a*/*b* ratio) is indicative of the invariant electronic character of the carbon deposited during the EBID process.

Figure 8-5 shows the evolution of the C/Si Auger ratio for the chemisorption (CVD) of ethylene (absence of electron-beam) on Si(100) at 300K (obtained from reference [203]). By comparing with the ratios of Figure 8-2, one can directly compare the efficiency of CVD and EBID for the growth of carbon deposits on the Si(100) surface at 300K. The CVD process saturates at a C/Si Auger ratio of ~ 0.036 whereas the amount of carbon potentially deposited by EBID appears unlimited.

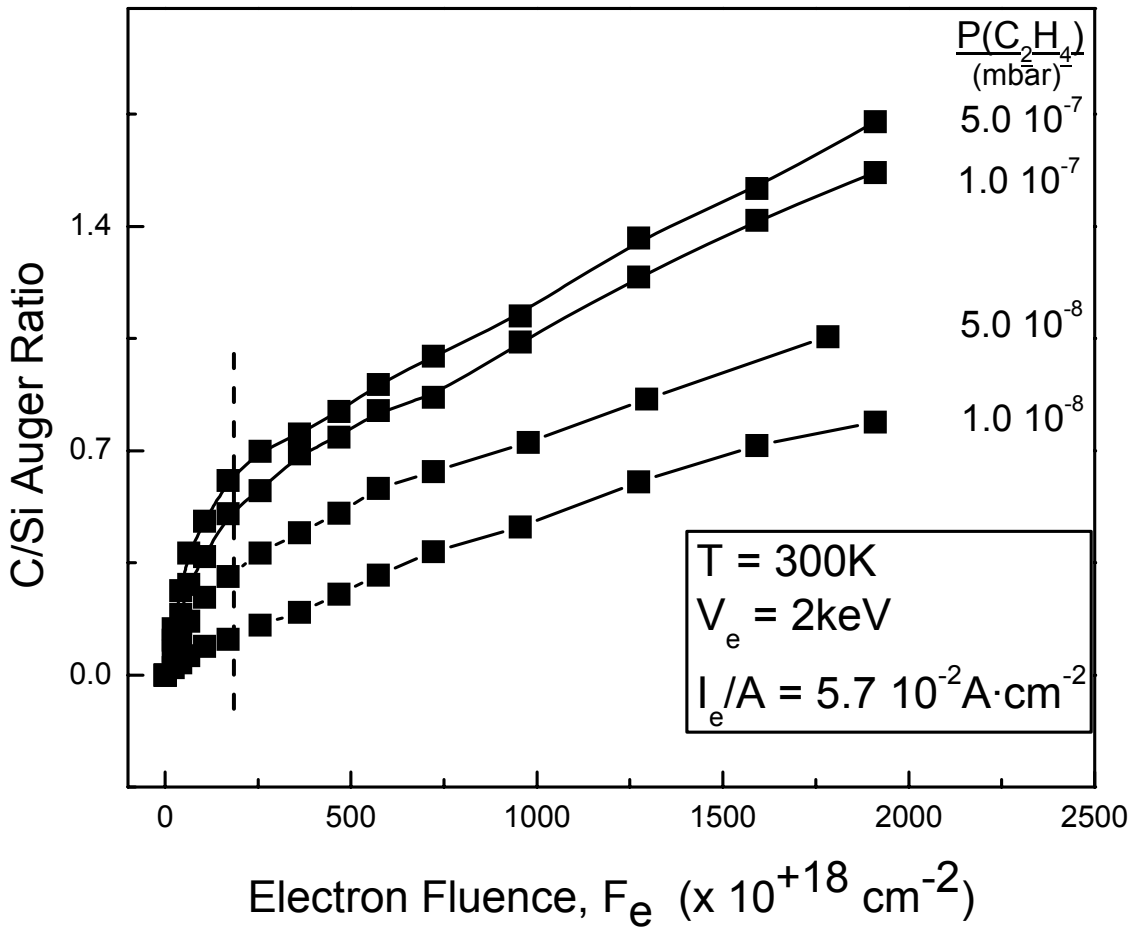

Figure 8-2: Evolution of the C/Si Auger ratio with increasing fluence of electrons, F_e, on the sample and as a function of the background pressure of the ethylene precursor molecules during electron-beam-induced deposition. Experiments were performed at 300K, with an acceleration voltage of 2keV and a current density of 5.7 x 10^{-2} A cm^{-2}.

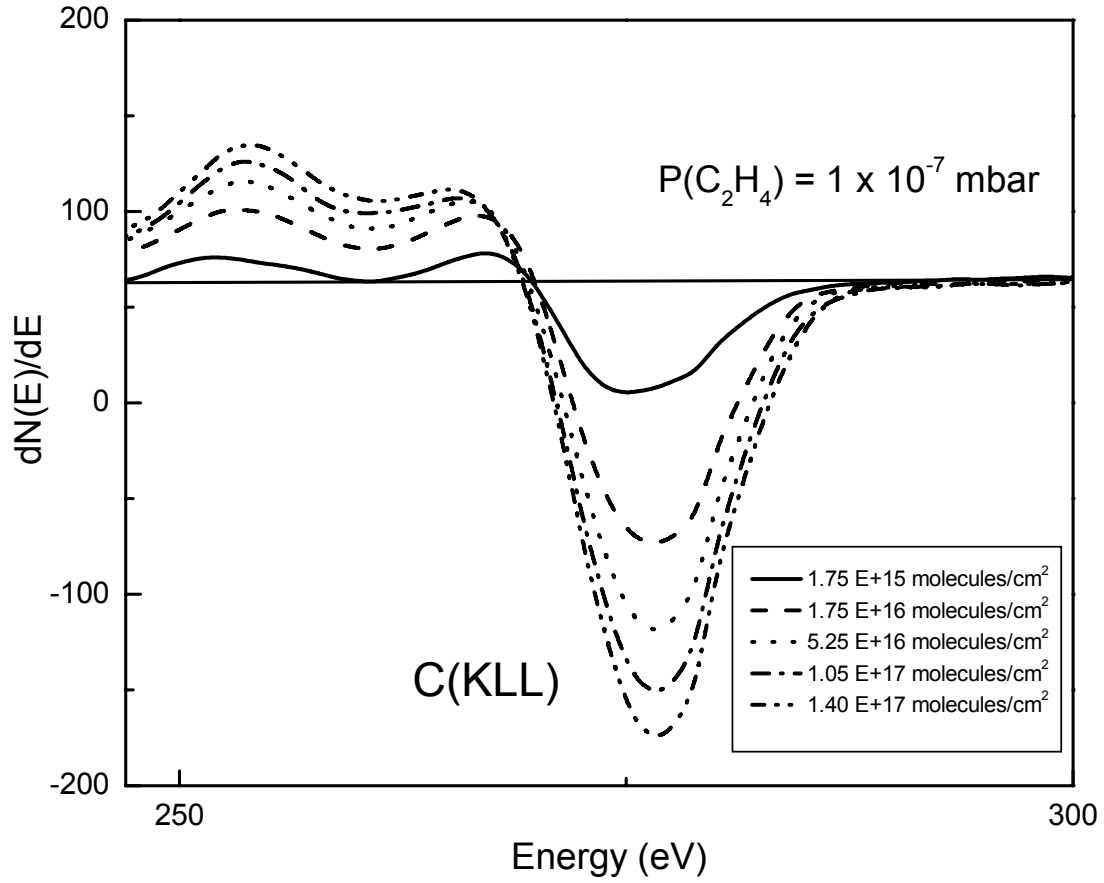

Figure 8-3: Carbon Auger lineshape vs. extent of EBID process. Full line represents the early C_2H_4 dosing stage (1.75 x 10^{+15} molecules/cm^2). An amorphous carbon-like structure is formed. As the dosing time is increased so does the intensity of the carbon peak.

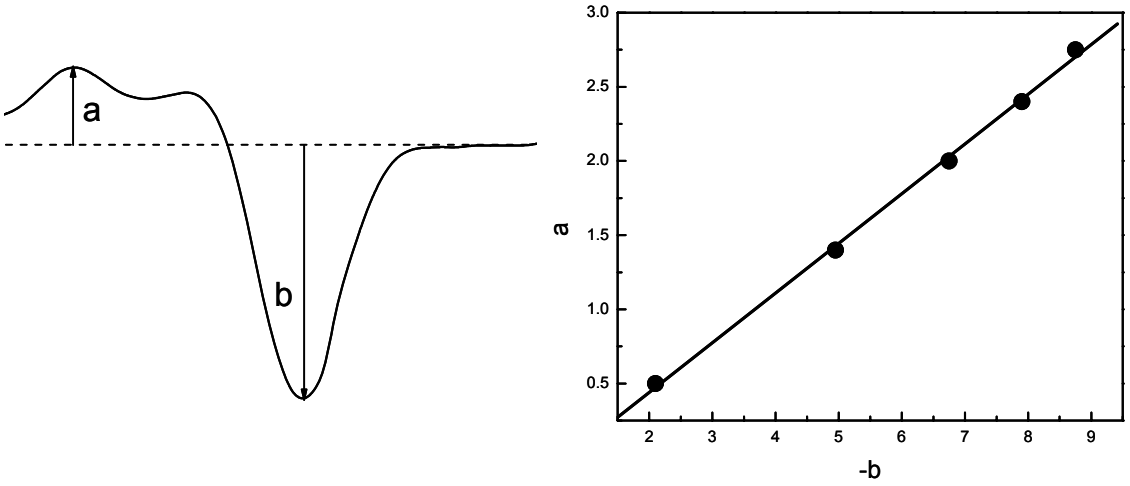

Figure 8-4: Analysis of the carbon Auger lineshape from Figure 8-3 showing the invariance of the carbon electronic character during EBID. (left) definition of two parameters *a* and *b*, characteristic of the carbon Auger lineshape; (right) plot of *a* vs. -*b*.

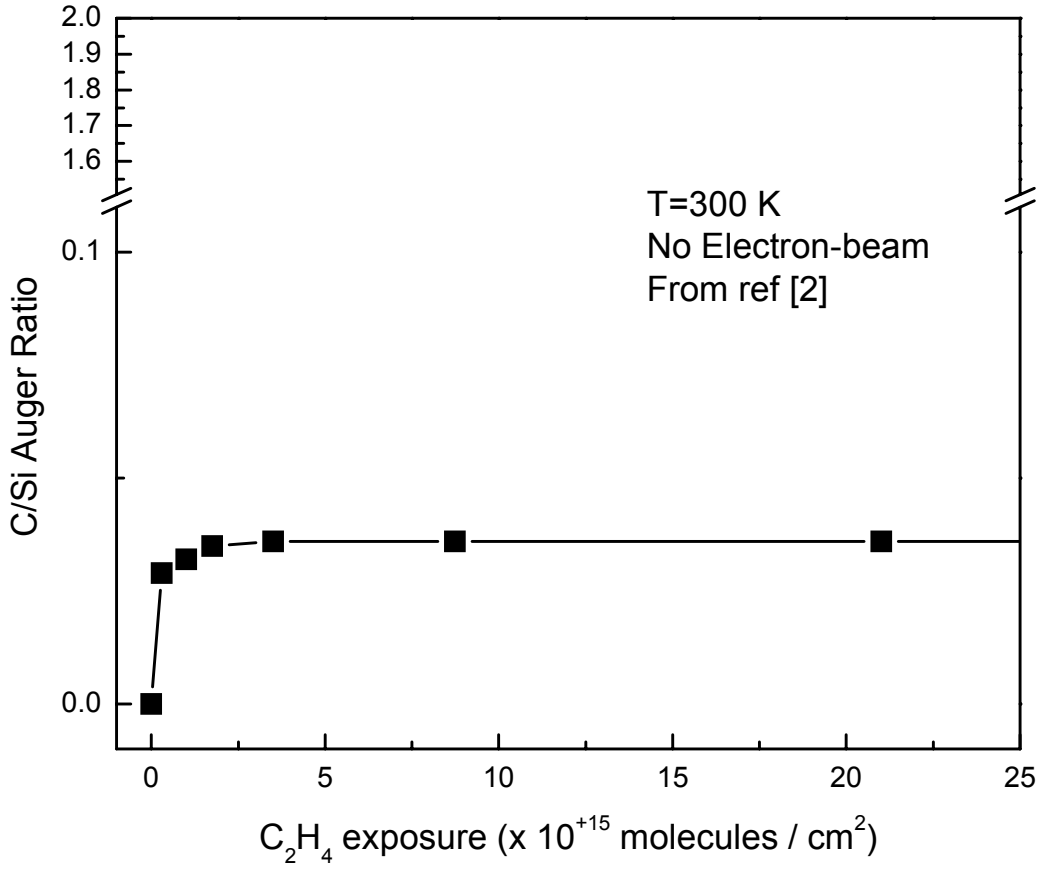

Figure 8-5: C/Si Auger ratio vs. exposure to ethylene molecules during CVD-process at 300K. Adapted from Ref. [203]. The C/Si Auger ratio saturates for a very low fluence of ethylene molecules, at a very low value compared to the EBID process.

8.4.2. Effect of Annealing EBID Carbon Layers

The evolution of the carbon Auger lineshape after annealing of the EBID-sample to temperatures in the range 1085K – 1276K is presented in Figure 8-6. Upon annealing, the carbon Auger lineshape becomes typical of a carbidic species [223]. The dashed curve on Figure 8-6 represents the C(KLL) peak after annealing the EBID-sample at 1085K. This curve exhibits a transitional lineshape, between the typical amorphous carbon lineshape (solid line) and the carbidic species lineshape (three curves corresponding to annealing of the EBID-sample at

1185K, 1235K and 1276K. For temperatures higher than 1170K the carbon layer is purely carbidic. There is no change of lineshape in the C(KLL) peak past this annealing temperature. The intensity of the carbon peak varies, presumably due to migration of carbon into the bulk above ~1000K. It should be noted that after rapid heating to 1470K, a clean Si(100) substrate is regenerated, as deep carbon penetration into the bulk takes place.

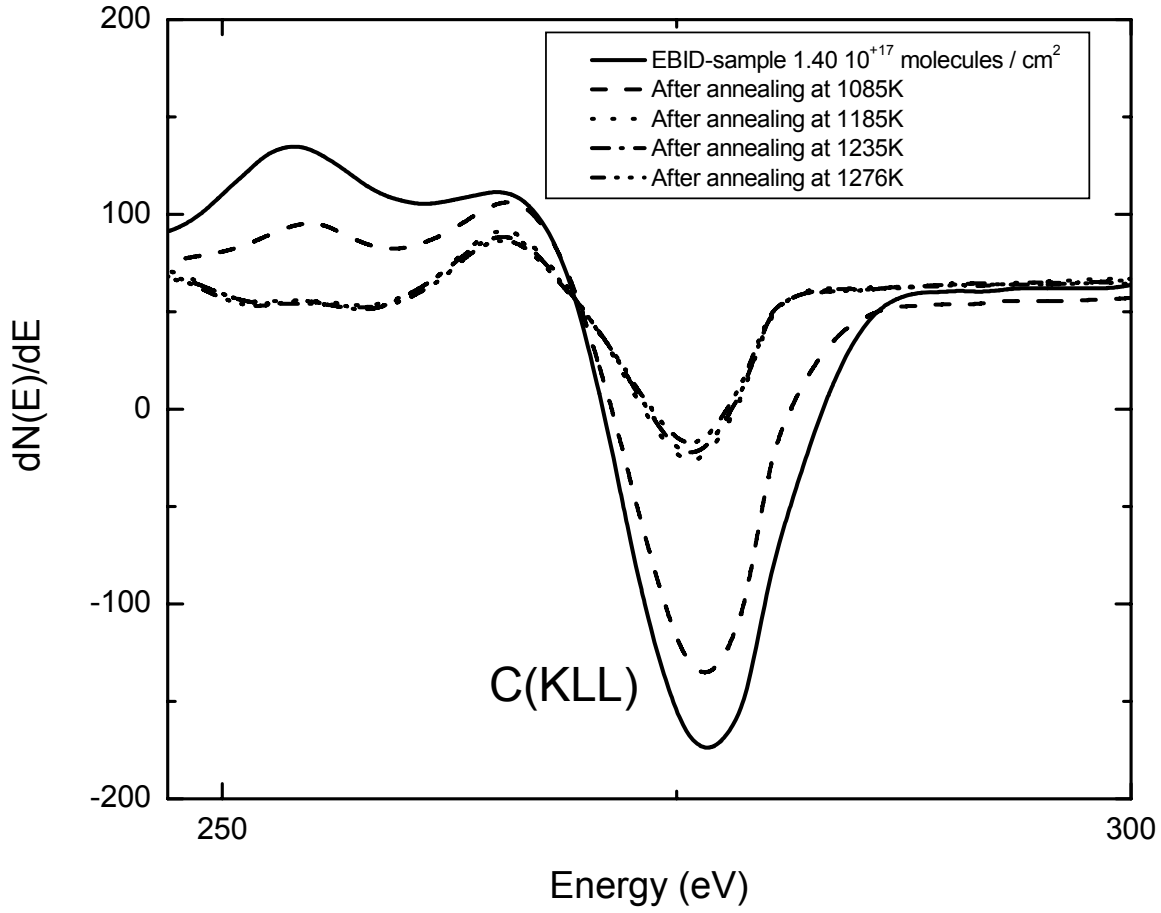

Figure 8-6: Evolution of the carbon Auger lineshape with annealing after EBID. The lineshape evolves from one characteristic of amorphous carbon (solid line) to a transition lineshape (dashed line) to finally a carbidic lineshape (dotted and dotted-dash lines) for temperatures above 1185K.

8.4.3. XPS Evolution of C(1s) Peak and Si(2p) Peak during Annealing after EBID

All XPS spectra were acquired with an X-ray source power of 480 watts (12kV, 40mA) using the Mg Kα source and with the electron energy analyzer operating in the ΔE mode, which results in constant resolution across the entire energy spectrum. The C(1s) and Si(2p) peaks including the Si(2p) plasmon-loss feature were investigated.

Figure 8-7 shows the development of the Si(2p) feature and its associated plasmon loss feature as the exposure to C_2H_4 occurs under EBID conditions. Little change is observed in either of the two features, indicating that little reaction between C and Si atoms occurs in EBID at 300K when C_2H_4 is employed as a carbon source.

Figure 8-8 shows the parallel evolution of the binding energies of the C(1s) peak and the Si(2p) peak and the associated plasmon loss feature as a function of the annealing temperature after ethylene dosing under EBID conditions. As the annealing temperature was increased the C(1s) peak shifted by 1.8eV towards lower binding energies (from 285.6eV to 283.8eV). The plasmon loss feature associated with the Si(2p) peak shifted towards higher binding energies by 5.5eV (from 17.3eV from Si(2p) peak to 22.8eV). The peak shift occurs in the temperature range 989K – 1178K. The 5.5 eV shift associated with the plasmon loss feature of the silicon peak is characteristic of the plasmon associated with the formation of SiC species on silicon [224]. The position of the C(1s) peak at 283.8eV for temperatures higher than 1124K is also characteristic of carbidic species [225].

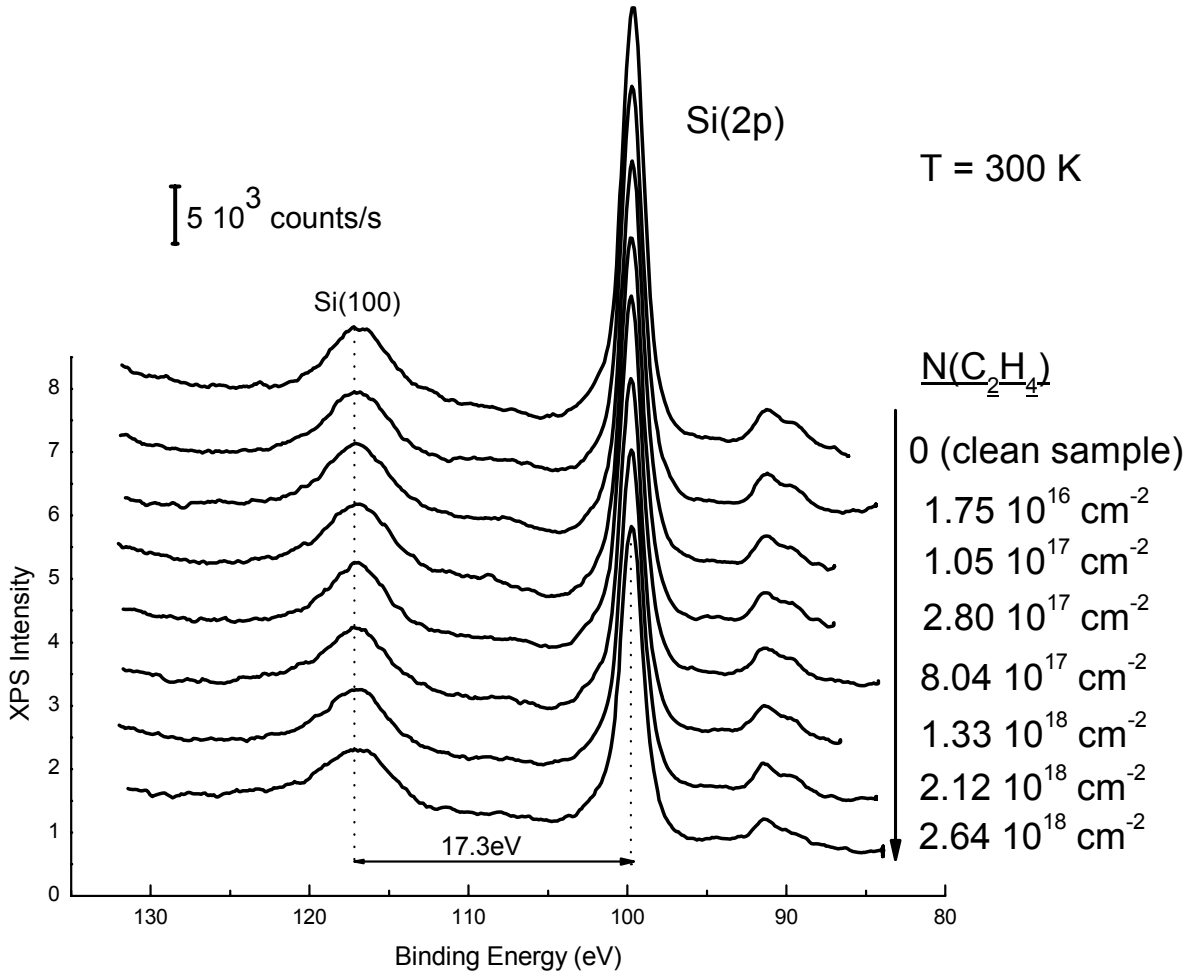

Figure 8-7: Evolution of the Si(2p) peak during the EBID of chemisorbed ethylene followed by XPS. The Si(2p) plasmon loss feature is at 17.3 eV above the Si(2p) peak when binding energy is plotted, and its position is invariant during the EBID process. This result correlates with the AES observation of Figure 8-4.

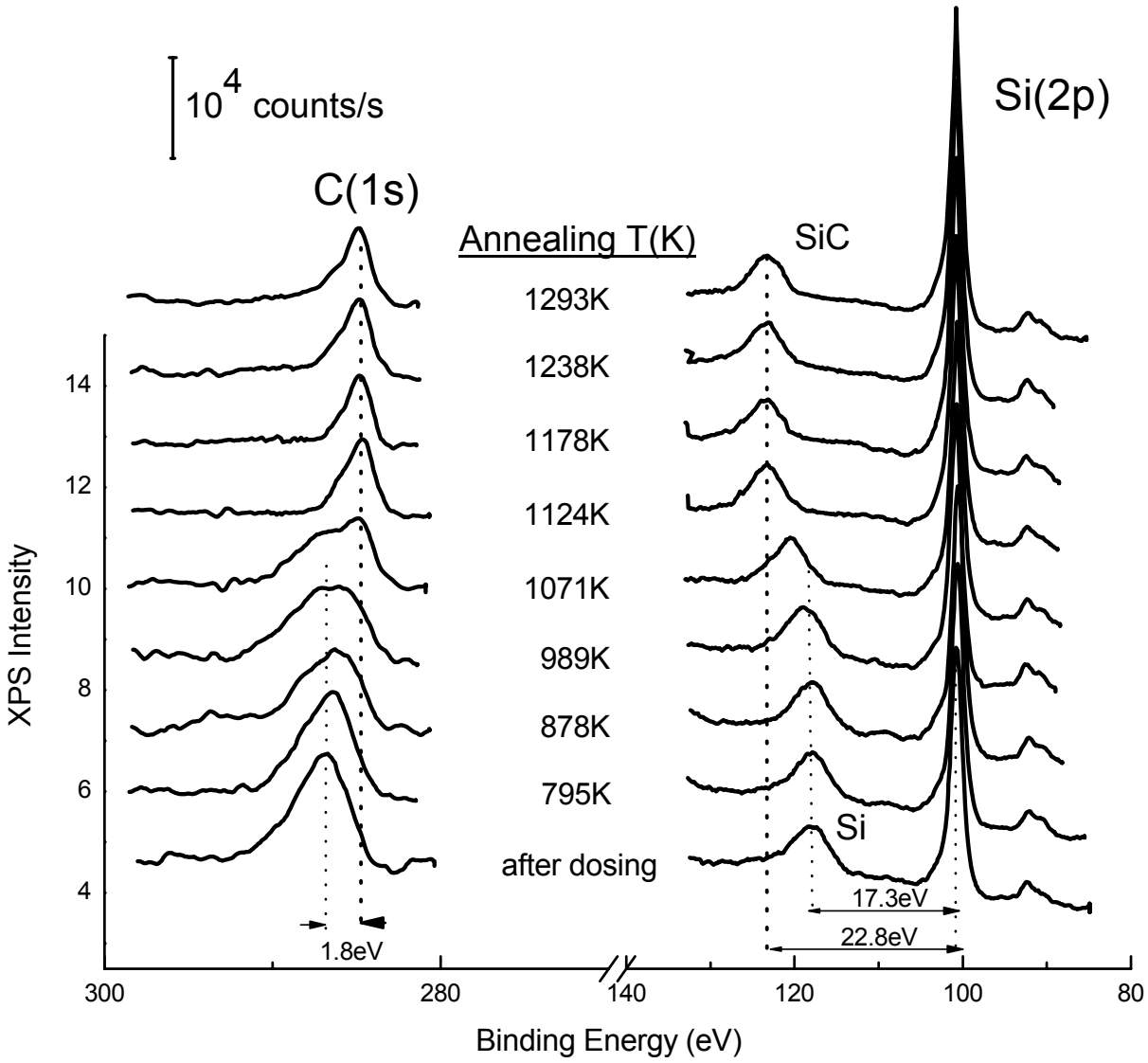

Figure 8-8: XPS spectra of C(1s) and Si(2p) during annealing after EBID. The plasmon loss feature shifts by 5.5 eV from the Si(2p) plasmon loss feature, characteristic of the formation of the carbidic species.

8.4.4. XPS Evolution of the Si(2p) Peak during Annealing after Chemical Vapor Deposition (CVD) in C_2H_4

Figure 8-9 shows the evolution of the Si(2p) peak for increasing annealing temperatures (between 677K and 1254K) for a sample prepared by CVD at 560K. The typical plasmon loss feature shift from 17.3eV after CVD at 560K to 22.8eV after annealing is observed. As was the case of annealing after EBID, the 22.8eV shifted feature is due to SiC and the spectral sequence corresponds to a transition from an amorphous-like carbon layer to the carbidic species.

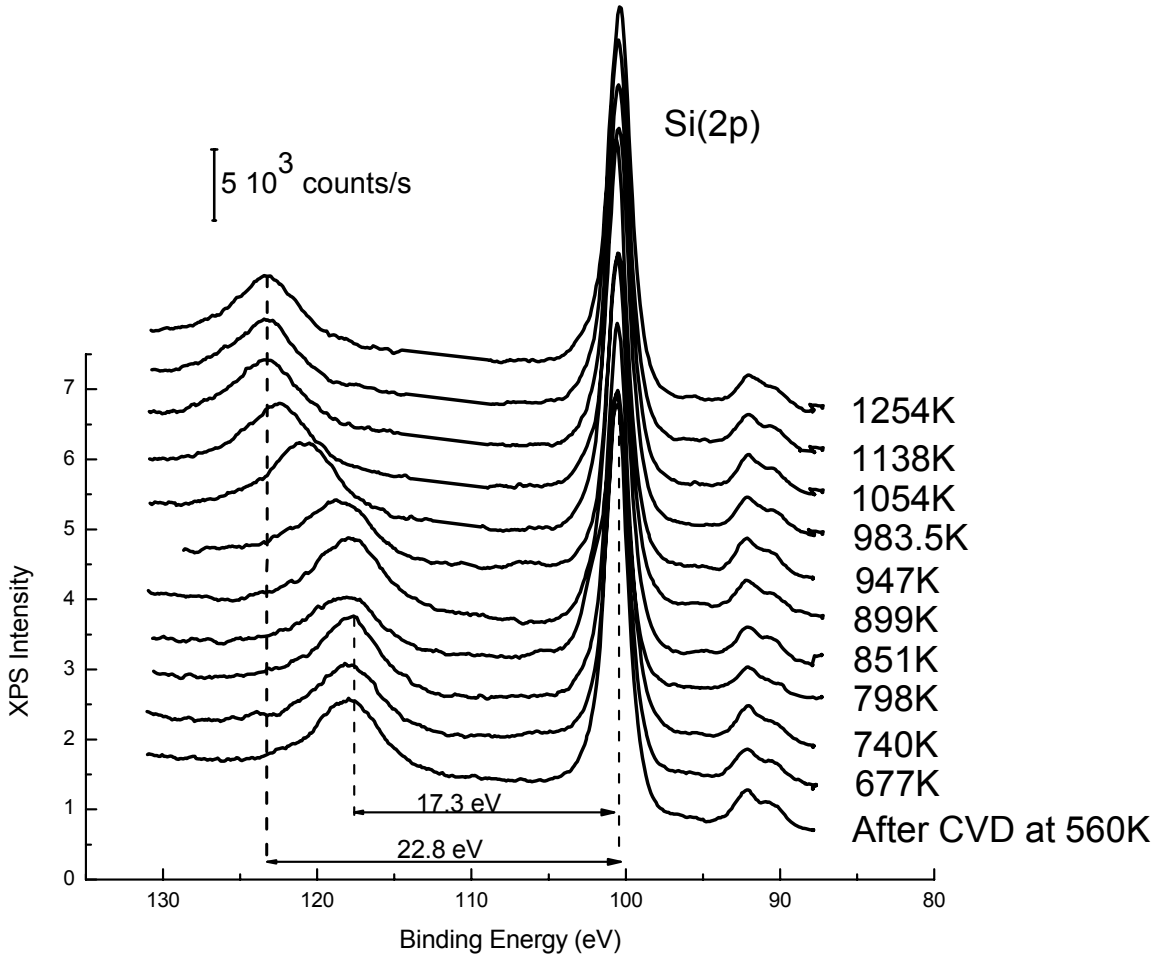

Figure 8-9: XPS study of the carbon layer produced by CVD from C_2H_4. During annealing, the Si(2p) plasmon loss feature shifts by 5.5 eV which is characteristic of the formation of carbidic species on the surface. The initial C_2H_4 exposure at 560K was 6.1 x 10^{+18} molecules cm^{-2}.

8.4.5. Temperature Dependence of the Conversion of EBID and CVD Carbon Layer to SiC

For both carbon deposition methods, the Si(2p) plasmon loss feature shifts by 5.5eV towards higher binding energies from the Si(2p) peak near 100eV (from 17.3eV to 22.8eV). As shown in Figure 8-10, the main difference resides in the temperature range over which this plasmon loss feature shift takes place. Figure 8-10 shows a comparison of the temperature range for the shift of the Si(2p) plasmon loss feature during annealing by an identical temperature program after carbon deposition by either CVD or EBID. It may be seen that the conversion of EBID-carbon to SiC occurs at about 100 - 150K higher temperature than is observed for CVD-carbon.

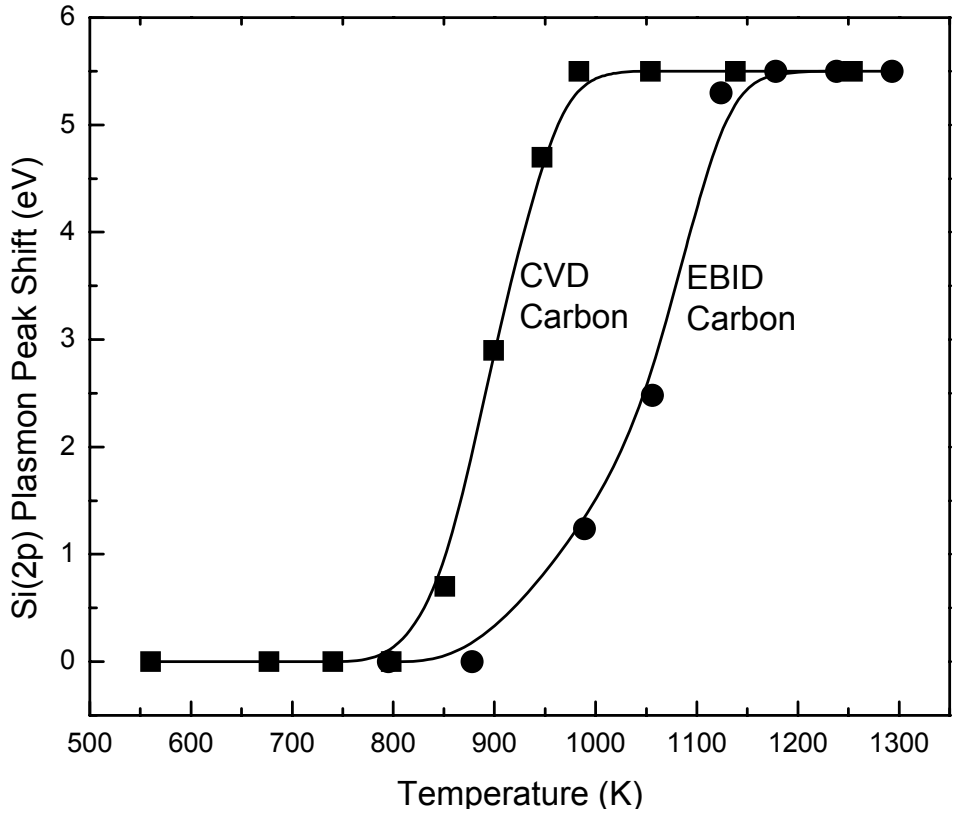

Figure 8-10: Comparison of the temperature range for the formation of SiC after CVD-carbon deposition (squares) and EBID-carbon deposition (circles). The formation of SiC occurs at about 100-150K higher temperature in the case of EBID-carbon. The lines are intended to guide the eye. The final SiC coverage in the two experiments, as judged by the SiC plasmon intensity, is within a factor of 1.25.

8.4.6. Temperature Programmed Desorption Experiments. Comparison of CVD-Carbon and EBID-Carbon

Temperature-programmed desorption (TPD) experiments were performed with a heating rate of 2 Ks^{-1}. Atomic mass units 28 (for ethylene) and 2 (for hydrogen) were measured simultaneously. Figure 8-11 shows the TPD spectra of ethylene and hydrogen from the Si(100) surface. The solid curve represents the TPD of ethylene after the EBID-process whereas the dashed curve refers to the sample after CVD of ethylene. The two dotted curves are intermediate steps, in which EBID was performed on the sample with smaller electron fluences than in the case of the solid curve. It may be seen that the coverage of ethylene diminishes as increased EBID occurs (left panel, Figure 8-11) whereas the production of chemisorbed hydrogen (desorbing by TPD at ~ 720 K) is enhanced by EBID. This experiment shows that C-H bonds in ethylene are cracked by electron bombardment and that some of the hydrogen atoms produced from cracking are captured.

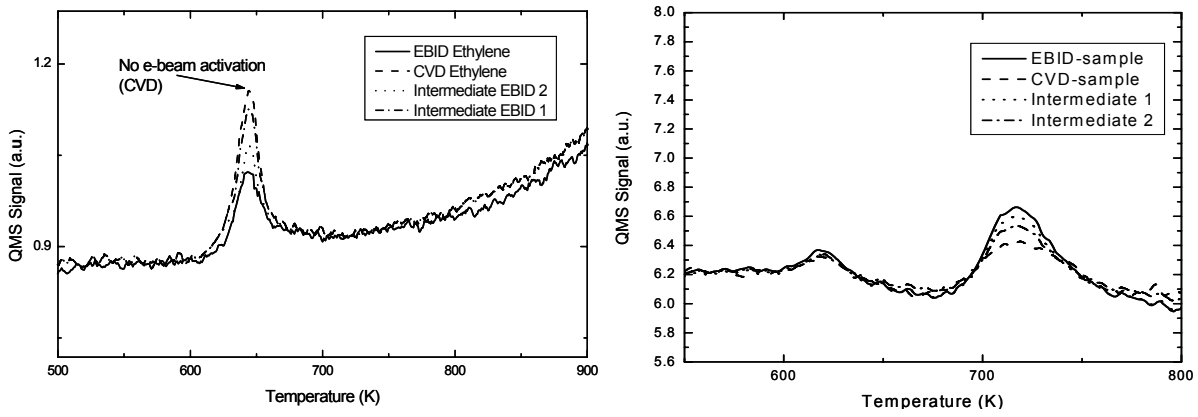

Figure 8-11: Temperature-programmed desorption spectra of ethylene (a) and hydrogen (b) after EBID (solid line) and after CVD (dashed line). Partial EBID curves (dotted and dash-dot lines) are also shown. In the case of EBID, thermal desorption of ethylene is reduced and dehydrogenation becomes the dominant surface process at higher temperatures (~720K). dT/dt = 2Ks^{-1}.

8.5. Discussion

The interest in the use of electron beam induced dissociation (EBID) of ethylene to produce adsorbed carbonaceous patterns on Si(100) surfaces is related to the use of these patterns for inducing localized regions of strain in the surface [226] as will be discussed in Section 9. Such strained regions can induce the nucleation of other deposited materials, such as Ge, leading to the production of Ge quantum dots [93,98] (see Section 10).

In this work, building on other studies of EBID of adsorbed molecules [211,213,215,216,218,219,227], we have found that the EBID process is efficient for adsorbed ethylene and that the properties of the carbonaceous deposit made by EBID differs from that produced by the thermal decomposition of the parent carbon source, adsorbed ethylene. The use of ethylene as a precursor molecule to carbonaceous film deposition builds upon previous studies of the bonding and surface chemistry of chemisorbed ethylene on Si(100). Here, di-sigma bonding of ethylene to Si(100) dimers results in the conversion of the hybridization state of ethylene from sp^2 to sp^3 as surface Si-C bonds are formed. Previous studies show that the thermally-activated surface decomposition of the sp^3-hybridized species to carbonaceous species is relatively inefficient, with about 95 % desorption of intact ethylene and only 5% decomposition, leading to the production of an adsorbed carbonaceous film [210].

The use of EBID for the production of a carbonaceous film is very efficient compared to the thermal decomposition of ethylene (compare Figure 8-2 and Figure 8-5), and the film can be grown to large thicknesses by EBID. Film growth rates of about $4\ 10^{-3}$ Å s^{-1} are observed under these conditions assuming a Si(2p) electron mean free path of 15 Å through the C_yH_x film. Thus, the majority of the EBID process involves the interaction of electrons with adsorbed C_2H_4, not on Si(100), but on the growing carbonaceous film. The observation of continued growth to very

thick films indicates that C_2H_4 can adsorb on the growing carbonaceous layer, where it is then dissociated by electron bombardment.

We believe that the primary electron-induced process is the partial dehydrogenation of adsorbed ethylene to produce C_2H_x species, where $x < 4$. Such coordinatively unsaturated species will interact with the underlying silicon, or carbonaceous layer, to produce a polymeric layer consisting of a carbon-carbon bonded structure where C-H bonds coexist, making a C_yH_x polymer. Continued irradiation of this polymeric film will remove C-H bonds in the surface and possibly the subsurface regions, leading to coordinative unsaturation and to the ability of the growing carbonaceous layer to bind incoming C_2H_4, for further EBID and film growth. The C_yH_x layer exhibits the C(KLL) Auger spectrum shown in Figure 8-3 (initial curve), and the C(1s) XPS spectrum shown in Figure 8-8 (bottom curve, left side), with a C(1s) binding energy of 286.7 eV. We designate this C_yH_x film as amorphous hydrogenated carbon. Figure 8-11 (right side) shows that H_2 may be thermally desorbed from this film at about 720 K, leading to the production of more carbon-carbon bonds in the amorphous carbon layer, where multiple C-C bonds are likely to be produced as C-H bonds are eliminated by EBID. The dehydrogenation process caused by electron bombardment does not lead to appreciable changes in the Si plasmon energy or the Si(2p) binding energy (Figure 8-7) (which are mainly related to the underlying Si surface), indicating that Si-C bonds have not been produced by EBID at 300K.

The EBID-produced carbonaceous film is converted to SiC beginning at about 900 - 950 K as judged by the onset of the 1.8 eV shift of the C(1s) binding energy from 286.7 eV to 284.9 eV (Figure 8-8), by the onset of the 5.5 eV shift of the plasmon loss feature from a loss energy of 17.3 eV to 22.8 eV (Figure 8-8 and Figure 8-10), and by a change in the C(KLL) Auger

lineshape (Figure 8-6). This thermal conversion temperature for the EBID-produced C_yH_x polymer deposit differs from the conversion temperature observed when adsorbed C_2H_4 is dehydrogenated thermally to an amorphous carbon layer and then converted to SiC. The latter process begins at a temperature about 100 - 150K lower than for EBID-carbonaceous material, near 800 K as shown in Figure 8-10. In both cases, the temperature programmed desorption data (Figure 8-11) show clearly that hydrogen has been completely evolved before conversion from amorphous carbon to SiC occurs.

These results suggest that two different types of dehydrogenated amorphous carbonaceous films result when EBID- and thermally-produced amorphous carbon films are produced. The EBID-produced dehydrogenated carbon films are more stable than the thermally-produced dehydrogenated carbon films. We can speculate that EBID, because of the electronic excitation involved, produces a greater fraction of higher order carbon-carbon bonds (C=C and C≡C) than does thermal decomposition of chemisorbed C_2H_4. The enhanced stability of the multiply-bonded carbon atoms in the dehydrogenated film leads to the ~100-150 K higher conversion temperature from C_y polymer to SiC. The production of multiple carbon-carbon bonds upon electron bombardment of organic species is consistent with the observations of the formation of fullerenes from graphite under electron bombardment conditions [228].

A schematic picture of the EBID process involving adsorbed C_2H_4 precursor species is shown in Figure 8-12, where both the EBID process and the subsequent thermal conversion process to SiC is illustrated.

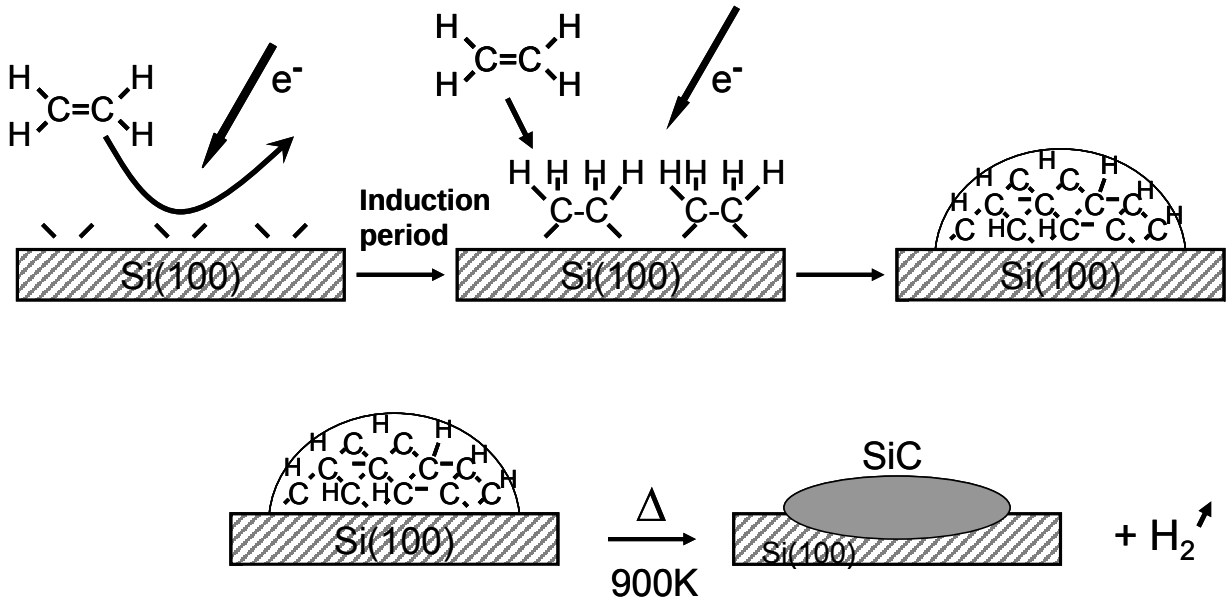

Figure 8-12: Schematic of the EBID deposition of C_yH_x on Si(100). The C_yH_x film is converted into SiC upon annealing to temperature higher than ~900K.

8.6. Summary of Results

The following results have been obtained in comparing the electron beam and the thermally-induced decomposition of C_2H_4 on Si(100).

1. Facile deposition of a C_yH_x film on Si(100) to any desired thickness is efficiently accomplished using 2 keV electron bombardment under conditions where chemisorbed C_2H_4 is continuously produced on the growing film. Current densities of the order of 56mA cm^{-2} and C_2H_4 pressures of the order of 10^{-7} mbar are employed.

2. The C_yH_x film has been characterized by XPS and Auger spectroscopy.

3. The C_yH_x film is dehydrogenated at about 720 K.

4. Beginning at about 900 - 950 K, the EBID-produced carbonaceous film begins to convert to SiC, as judged by XPS, plasmon loss and Auger lineshape studies. Conversion is complete near 1150 K.

5. Carbonaceous films produced by the thermal decomposition and dehydrogenation of C_2H_4 on Si(100) are less stable than EBID-produced carbonaceous films and begin to convert to SiC at about 800 K with completion near 1000 K.

6. It is postulated that the enhanced thermal stability of C_y films made by EBID compared to thermally-produced C_y films is due to an increase in the fraction of multiple carbon-carbon bonds in the amorphous C_y film when electronic excitation is involved in film formation from adsorbed C_2H_4.

In the next section, the results of this study will be applied to the formation of sub-10nm SiC arrays by electron-beam-induced deposition in a high-resolution scanning electron microscope.

9. Formation and Thermal Stability of sub-10 nm Carbon Templates on Si(100)

9.1. Abstract

We report a lithographic process for creating high-resolution (<10 nm) carbon templates on Si(100). A scanning electron microscope, operating under low vacuum (10^{-6} mbar), produces a carbon-containing deposit ("contamination resist") on the silicon surface *via* electron-stimulated dissociation of ambient hydrocarbons, water and other adsorbed molecules. Subsequent annealing at temperatures up to 1320 K in ultrahigh vacuum removes SiO_2 and other contaminants, with no observable change in dot shape. The annealed structures are compatible with subsequent growth of semiconductors and complex oxides. Carbon dots with diameter as low as 3.5 nm are obtained with a 200 μs electron-beam exposure time.

9.2. Introduction

Control over the growth of silicon-based structures at the sub-10 nm scale approaches the end of scaling for silicon. Single electron devices [109-111,229-231], quantum cellular automata [112,115], and quantum computing architectures [112-114] require device dimensions that fall below the 10-nm limit. Atomic-scale assembly in Si has already been demonstrated using scanning tunneling microscopy [232,233] (STM). However, STM-based self-assembly is inherently both demanding and time consuming. Self-assembled quantum dots, produced by Stranski-Krastanow growth processes [27,54], exhibit poor control over the size and none over the location of islands.

For decades it has been recognized that background gases in a scanning electron microscope (SEM) can be used as a "contamination resist" to create structures as small as 8 nm [234,235]. The lateral size of the deposited structures is determined by the convolution of the beam size with the spatial range of secondary electrons.

We have developed a procedure for creating carbon templates on Si(100) that will be employed for the subsequent growth of semiconductors or complex oxides, with reproducible feature sizes below 10 nm. These techniques may prove useful in the growth of controlled arrays of semiconductor quantum dots, devices that use few or single electrons, and quantum computing architectures [113]. The techniques described here are compatible with subsequent UHV-growth of materials using molecular beam epitaxy (MBE) or other growth methods.

9.3. Experiments and Analysis

9.3.1. Sample Preparation Prior to EBID Process

For the experiments described here, the following cleaning procedure is used. Si(100) crystals (boron doped, ρ=0.05 Ω·cm, single-side polished) are cut to dimensions 10x5x0.5 mm^3. Figure 9-1 shows schematically the sample preparation procedure. The polished Si surface is ozone-cleaned in air for 20 min. using a low-pressure mercury lamp, followed by a modified RCA *ex-situ* chemical cleaning procedure [172]: (1) 10 min. (H_2O_2:H_2SO_4 1:2) at 130°C [170]; (2) Standard Clean-1 at 65°C for 5 min. (H_2O:H_2O_2:NH_4OH 5:1:1); (3) Standard Clean-2 at 65°C for 10 min. (H_2O:H_2O_2:HCl 6:1:1) [171,222]; (4) oxide etch for 15 seconds using (HF:H_2O 2:100). This treatment is known to produce a hydrogen-terminated Si(100) surface free of organic contaminants[172]. Throughout the process we use water with a resistivity of 18.1 MΩ.cm which is

produced by a four-stage deionization process combined with UV-oxidation and a 0.2 micron filter producing low organic contamination (<1 ppb).

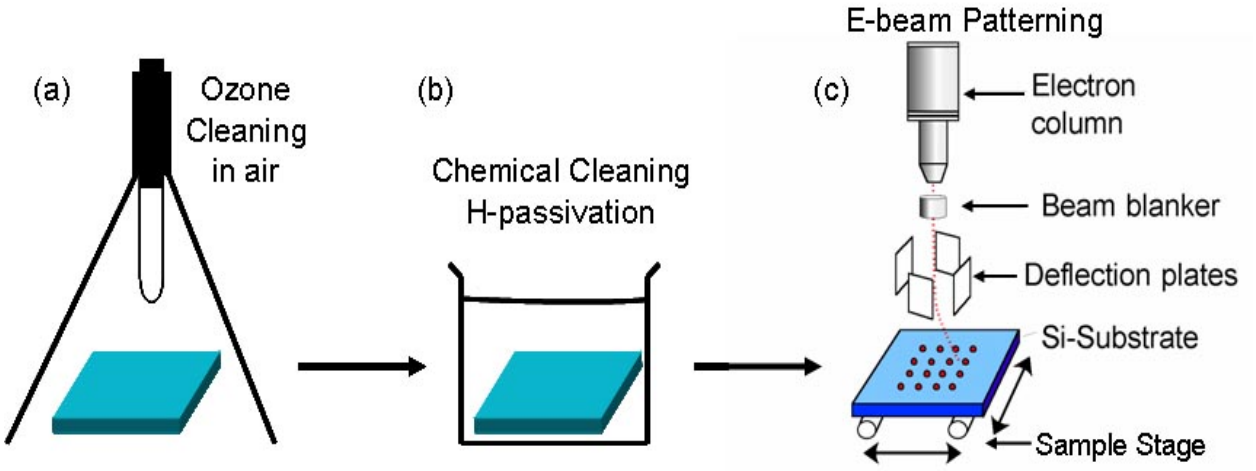

Figure 9-1: Process for carbon patterning of a Si(100) wafer. Wafer is (a) ozone cleaned using a low pressure mercury lamp; (b) H passivated using an RCA-derived chemical cleaning technique; and (c) transferred to a high-resolution SEM where ultrasmall carbon dots are patterned on the Si surface.

9.3.2. Carbon Patterning by Electron-Beam-Induced Deposition (EBID)

9.3.2.1. Experimental Set-up

Carbon patterns are created using a high-resolution scanning electron microscope (HR-SEM, LEO VT1530), combined with a high-throughput 50MHz pattern generator/ lithography system (Xenos semiconductor) and a ultra-fast beam blanker (Raith). The HR-SEM has a beam diameter of ~1 nm and is operated at an acceleration voltage of 20 kV and a beam current of 340 pA. The background pressure of $5x10^{-6}$ mbar in the HR-SEM is produced by a

turbomolecular pump and backed by an oil-free roughing pump. Carbon is deposited locally on the substrate by electron-beam induced deposition[236] using naturally-present background gas containing CO and hydrocarbon molecules – as observed with a quadrupole mass spectrometer - adsorbed on the Si(100) surface as precursors[237]. These carbon-containing molecules are decomposed by an electronic excitation process and form amorphous carbon-containing deposits – likely containing O and H - on the surface[238]. Electron-beam-induced deposition carbon-dot formation was investigated by HR-SEM and Atomic Force Microscopy (AFM).

Carbon patterns are created on the surface by controlling precisely the electron-beam location and exposure time. The electron fluence can be as small as 4.3×10^{16} e.cm^{-2} (430 e.nm^{-2}) which corresponds to an exposure time of 160 ns, although typical exposure times are in the 100 μs -10 ms range. Larger-scale patterns are created by stepping the coarse position of the sample stage.

9.3.2.2. Investigation of Carbon Patterns

Figure 9-2 shows examples of carbon dot patterns formed by the procedure described above. Figure 9-2(a) features an HR-SEM image of a square pattern of carbon dots. It shows the regularity of the interdot spacing, l=50 nm, with a positional accuracy of ±1 nm in the 100-1000 nm range. Figure 9-2(b) shows a tapping-mode AFM scan of a different sample with l=35 nm. The dots themselves exhibit a high degree of uniformity in both size and shape, as determined by both HR-SEM and AFM. The exposure time is 1000 μs for Figure 9-2(a) and 1000 μs for Figure 9-2(b).

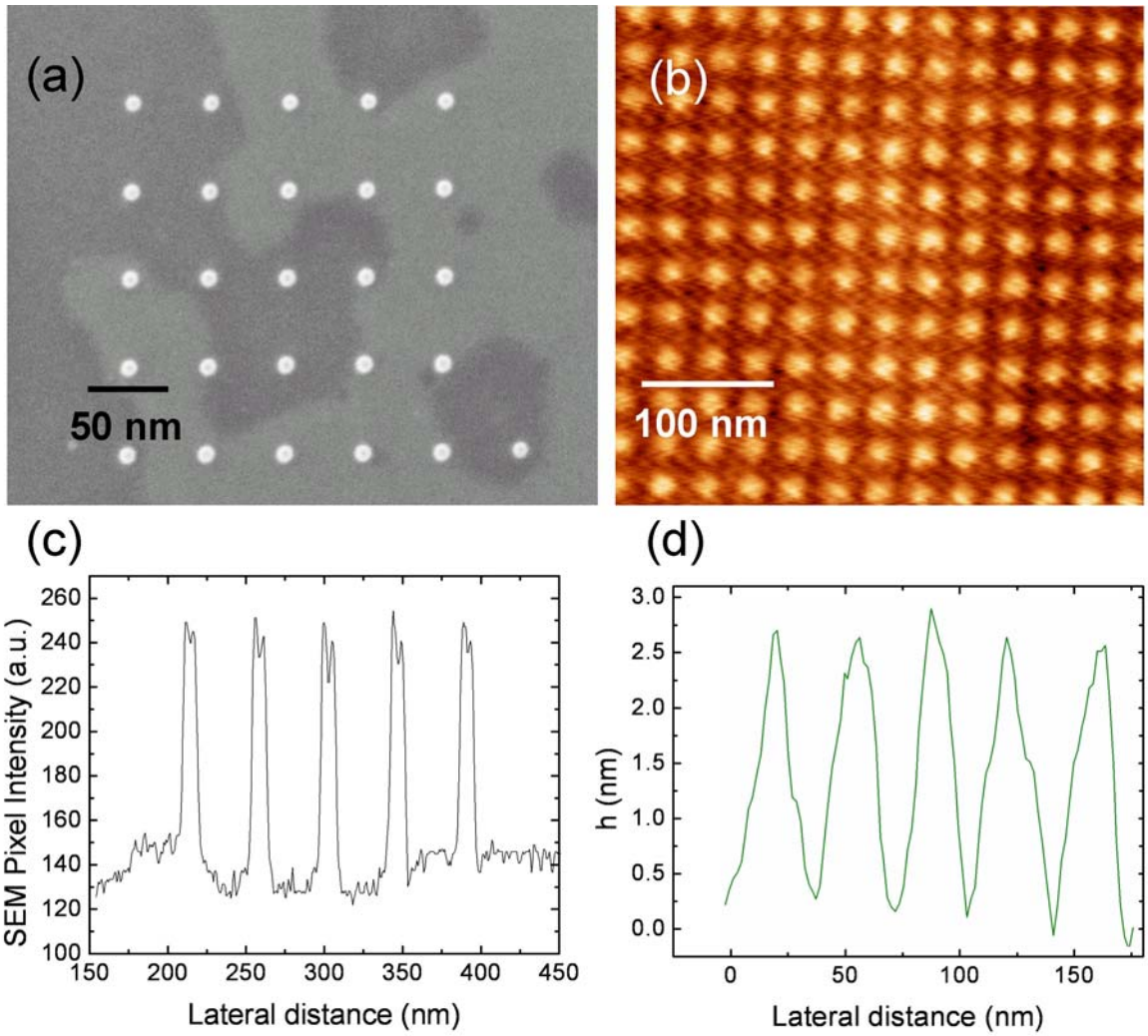

Figure 9-2: (a) SEM of a 5 x 5 array of ultrasmall carbon dots. Spacing between the dots is 50nm; (b) contact-mode AFM image of a similar carbon-dot array. Spacing between the dots is 35 nm; (c) FWHM profile of carbon dots from SEM image of (a). Average FWHM is ~9nm; (d) cross section profile of AFM from (b) showing an average height ~2.1 nm for the carbon dots. The dots were deposited by 1000 μs irradiation.

While AFM overestimates the width of the carbon dots due to the AFM probe interaction with the features, the height of the dots can be extracted from the AFM images. Figure 9-2(d) shows atomic force microscopy cross-sections of the high-density array of carbon dots produced with 1000 μs exposure time (dot-to-dot spacing ~35 nm) imaged in Figure 9-2(b), revealing their

height (~2.1 nm average). On the other hand, height information cannot be obtained from SEM images, but an upper bound of the width may be derived from analysis of the SEM images taken after patterning. Figure 9-2(c) shows a FWHM ~9.1 nm (estimated from the SEM image) for a pattern produced with 1000 μs exposure time.

Analysis of the dot height shows that the amount of carbon deposited is directly related to the beam exposure time (Figure 9-3). Carbon dots with various exposure times have been patterned on one single wafer. Over most of the range explored (200 μs to 1 s), the height h scales with the exposure time t according to $h \propto t^{1/3}$. The dependence of the dot width w (measured by AFM) agrees well with $w \propto t^{1/3}$ only at large exposure times. The deviation is most likely due to imaging artifacts associated with the finite radius of the AFM probe. Assuming that convolution of the dot profile with the tip simply adds a fixed amount to the measured diameter, one can fit the observed results to the $t^{1/3}$ scaling law, also shown in Figure 9-3. Under the conditions described above, the growth of the carbon dots appears isotropic, with a minimum dot diameter of 3.5 nm and 1 nm dot height obtained with a 200 μs exposure time.

9.4. Thermal Stability of Carbon Dots

For subsequent processing it is imperative that the carbon dots be stable to high-temperature annealing. In particular, it must be possible to remove oxide layers in order to grow subsequent semiconductor or oxide structures in UHV. In our annealing experiments we first treat the dot pattern with ozone to remove hydrocarbon contaminants from the substrate. Ozone cleaning prevents surface roughening by creating a protective oxide layer on the substrate [239]. Figure 9-4 shows AFM images of carbon dots before and after UHV-annealing at a pressure of

5.0 x 10^{-10} mbar and temperature of 1220 K for 5 minutes. After annealing at this temperature, the Auger and X-ray photoelectron spectroscopy spectra indicate no trace of contamination and feature only silicon and carbon peaks. The carbon pattern retains its overall geometry – symmetry and spacing. The gross pattern appearance did not change up to 1320 K, above which the dots disappeared, presumably due to migration of the carbon features into the bulk. We also observed a slight reduction of the dot height by AFM after ozone-cleaning of the dots (not shown).

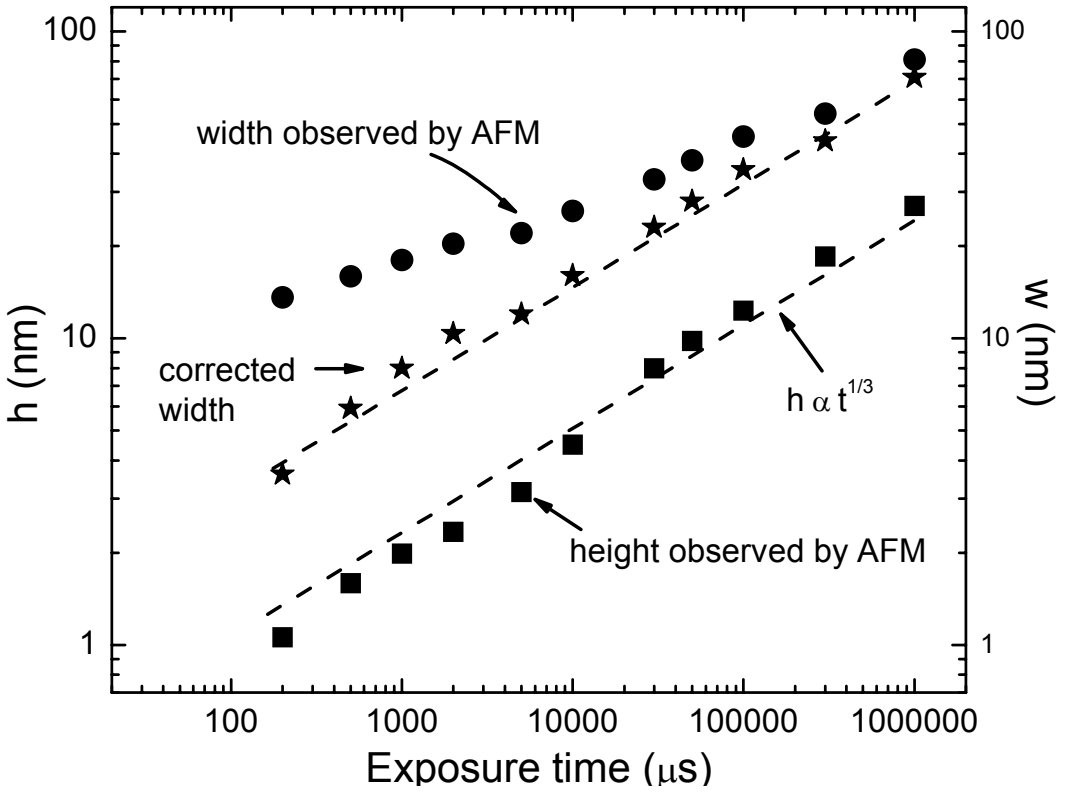

Figure 9-3: Height (squares) and FWHM (circles) of carbon dots, measured by AFM, vs. electron-beam exposure time. The FWHM by AFM was corrected (stars) assuming a tip radius of 5 nm.

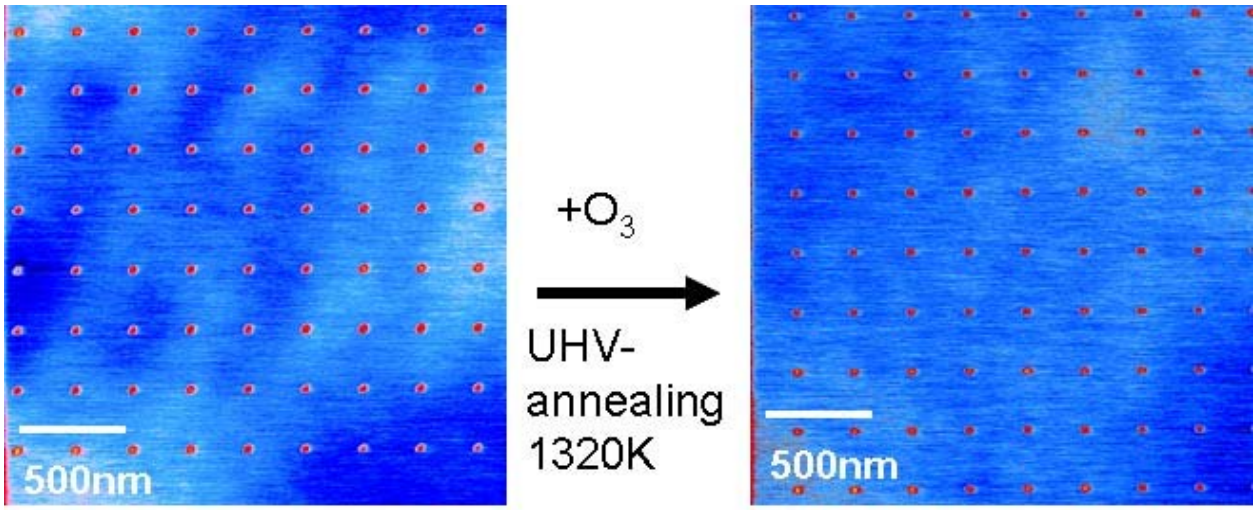

Figure 9-4: AFM images of a carbon dot array before (left) and after (right) annealing in ultrahigh vacuum (base pressure 5 x 10^{-10} mbar) at 1220K. The carbon dot spacing on appearance is stable up to 1320K.

9.4.1. Formation of SiC Dots

Electron-stimulated carbon deposition on Si(100) has been investigated using various pure hydrocarbon gases and was studied in UHV by AES, XPS and TPD[240] in Section 8. The thermal stability of the carbon films and dots was studied over the temperature range from 300 K – 1400 K. As the annealing temperature increased, the sample was investigated by AES and XPS. The signature of silicon carbide is observed for both techniques for temperatures higher than 989 K. The transformation of carbon into silicon carbide is complete 1178 K. The formation of the SiC structure is consistent with the observed high thermal stability of the carbon patterns.

9.5. Conclusion

In conclusion, sub-10 nm carbon patterns have been created lithographically on Si(100) by electron-beam induced deposition. These carbon dots are stable at temperatures higher than that required for the evaporation of SiO from oxidized silicon surfaces, making them very suitable for subsequent growth of semiconductors and oxides. In the next section, we will employ these locally strained Si surfaces[241] for subsequent semiconductor quantum dot growth[93,98] in organized patterns by directed self-assembly.

10. Patterning of sub-10-nm Ge Islands on Si(100) by Directed Self-Assembly

10.1. Abstract

Silicon-based devices with feature sizes below 10 nm represent the final stage for Moore's law scaling [242]. At these length scales, quantum confinement, tunnelling, and charge quantization can disrupt the functionality of conventional devices. These same quantum effects are essential for the operation of room-temperature single electron transistors [109,243-245], quantum cellular automata [115], and proposed Si-based quantum computing architectures [113,114,246,247]. Here we present a method for patterning sub-10 nm Ge nanostructures on Si(100) using a novel process of directed self-assembly. Electron-beam-induced decomposition of carbon-containing molecules on a silicon substrate produces carbon clusters that upon annealing in ultra-high-vacuum (UHV) form stable SiC nucleation sites. Subsequent deposition of Ge leads to templated growth of sub-10-nm Ge islands. We demonstrate control over Ge island size and placement that are significantly beyond what has been achieved previously. These nanostructured materials form attractive candidates for producing quantum devices that can operate at room temperature.

10.2. Experimental

Two important parameters related to the patterning of Ge nanoscale islands on Si are their average size *D* and spacing *L*. Nanoscale Ge islands (*D*~20-100 nm) can be created on Si(100)

via the Stranski-Krastanov instability, in which three-dimensional Ge islands form over a two-dimensional wetting layer that exceeds a critical thickness [27,54,55]. The kinetic and thermodynamic constraints on Ge island growth [54,70,83,248] produce random arrangements of islands with average diameters $D \geq 20$ nm and separations $L \geq 50$ nm. Pre-adsorption of carbon precursors (typically ~0.1 monolayers (ML)) has been shown to produce smaller (D~10 nm) Ge islands on Si(100) [92]. The islands are also randomly distributed, with a high density (~10^{11}/cm^2) and relatively narrow size distribution.

To control the placement of individual islands, several groups have developed templates using lithographic patterning [123,140,141] or focused ion beam implantation[143] as was shown in Section 4.3. In all cases, the smallest island size that has been achieved is D~20 nm, and the smallest separation observed is L~80 nm.

Our approach to creating precise patterns of Ge islands (Figure 10-1) exploits the ability of carbon to template the growth of Ge islands on Si(100). Single-side polished 2" diameter Si(100) substrates (phosphorus-doped, resistivity ρ~10^{-2} Ω-cm) are first ozone-treated and then chemically cleaned using standard methods [172], leading to the formation of a smooth hydrogen-passivated Si surface (RMS < 3 Å over a 1 μm scan size, measured by atomic-force microscopy (AFM)). A high-resolution electron-beam lithography system (Figure 10-1a) exposes this surface to a focused (~1 nm) beam of electrons (340 pA, 20 keV). Ambient carbon-containing molecules decompose on the surface, forming "carbon dots" whose diameters d~4-10 nm and heights h~1-10 nm depend on the electron beam exposure time per dot t_{el} (typically 10^{-4} – 10^{-1} s) as was shown in the previous Section[226].

After patterning, the Si wafer is ozone-treated again. This second treatment reduces the size of the carbon dots, removes hydrocarbons decomposed by secondary electrons during

exposure, and creates a protective oxide surface layer [239] that can be subsequently removed in UHV. The ozone exposure time should be longer than the time required to remove the background adsorbed hydrocarbons, and shorter than the time required to completely remove the carbon dots.

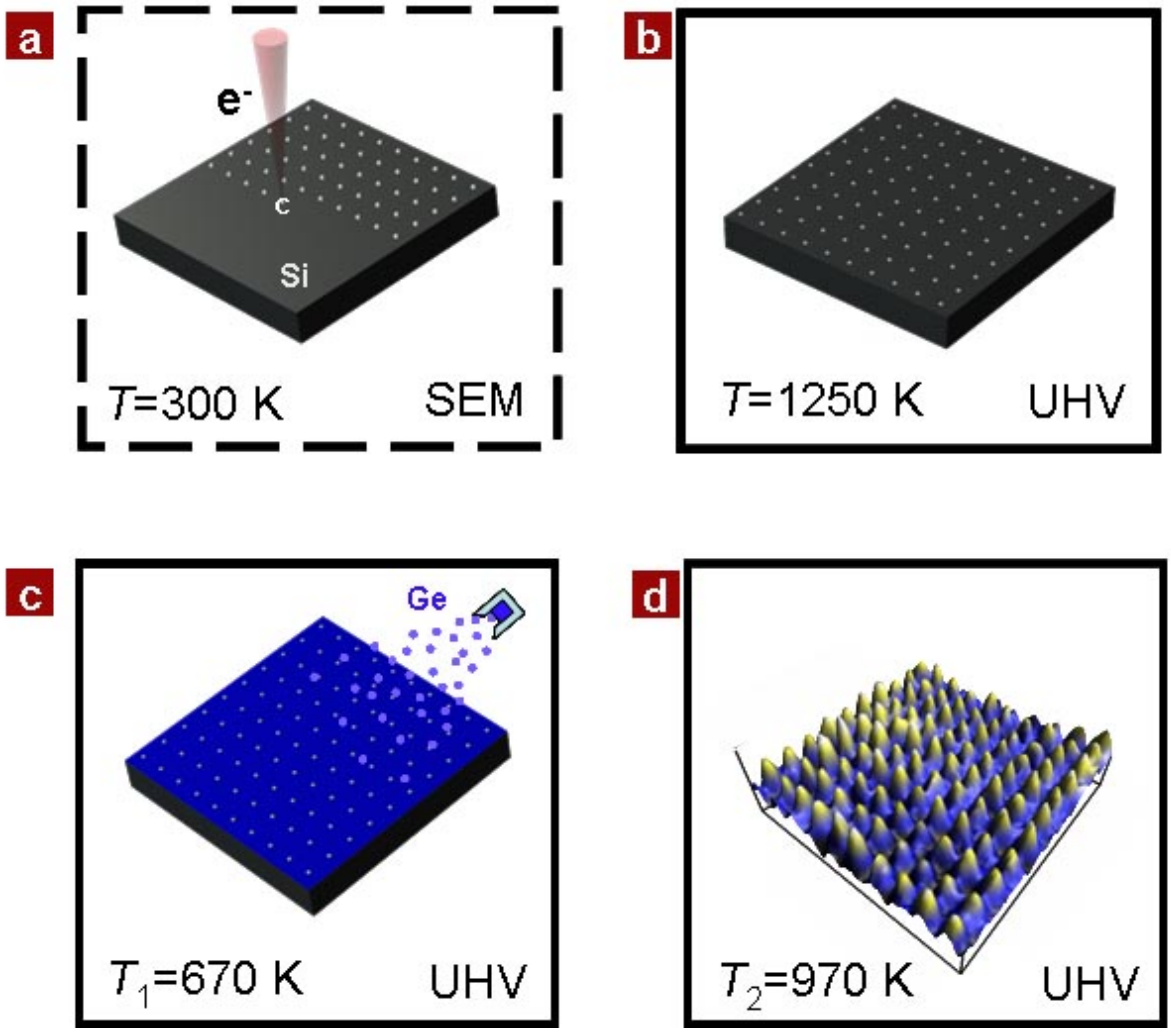

Figure 10-1: Schematic for templated Ge island growth. (a) Electron-beam induced deposition of carbon dot template; (b) Annealing in ultra-high vacuum to form SiC nucleation sites; (c) Deposition of Ge at temperature T_1; (d) AFM image (350 nm x 350 nm x 2 nm) of Ge islands that form after annealing at temperature T_2.

The patterned Si wafer is transferred to a UHV molecular-beam epitaxy (MBE) system and resistively heated to T_0=1250 K for ~5 minutes (Figure 10-1b). This step removes the protective oxide layer, and causes the carbon islands to react with Si to form highly stable SiC nucleation sites [240]. The sample temperature is then reduced to T_1 (typically 670 K) over 30 minutes, and N_{Ge} ~1-2 ML of Ge (where 1 ML = 678 atoms/100 nm^2) are deposited from an effusion cell onto the substrate at a rate R=0.06 Å/s (Figure 10-1c). The base pressure in the MBE chamber is typically 1-2 x 10^{-9} mbar, and no higher than 5 x 10^{-9} mbar during Ge growth. After Ge deposition, the sample is usually post-annealed at T_2 (typically 970 K) for a time t_2 (typically 30 minutes) to produce patterned islands. This last step greatly increases the surface mobility of Ge adatoms and is responsible for the formation of islands. Figure 10-1d shows an AFM image of a pattern of Ge islands created using this method (details are discussed below with Figure 10-4).

Throughout the MBE growth process (annealing, Ge deposition, post-deposition annealing), the quality of the surface is monitored by reflection high-energy electron diffraction (RHEED) to ensure complete removal of the oxide layer prior to Ge-deposition. Because of the small number of patterned carbon dots created in a typical experiment (~10^6), neither the SiC nor the surface roughness due to templated Ge growth are detectable by RHEED.

Figure 10-2 provides direct evidence that the SiC dots form attractive sites for mobile Ge adatoms. In this experiment, a 25 x 25 square array of SiC dots is prepared (t_{el}=100 ms, corresponding to a dot diameter ~30 nm, height ~10 nm before ozone treatment and annealing[226]). The AFM image shows one corner of the array; the rest of the region is unpatterned. Deposition of 4 ML of Ge at R=0.06 Å/s and T_1=T_2= 850 K (i.e., no distinct post-deposition annealing step) produces both self-assembled and patterned Ge islands. Two

relatively large Ge islands have formed over neighbouring pairs of SiC dots, demonstrating wetting of Ge on the patterned areas. Near the array boundary, the density of self-assembled islands falls significantly, indicating that the wetting layer thickness is locally reduced. An analysis of the spatial distribution of self-assembled Ge islands (Figure 10-3) confirms that this depletion region begins ~2 μm from the edge of the array. These diffusion lengths are consistent with other reported values for the annealing conditions used here [249]. No self-assembled islands are observed between the patterned islands, indicating that the Ge wetting layer thickness is reduced in that area.

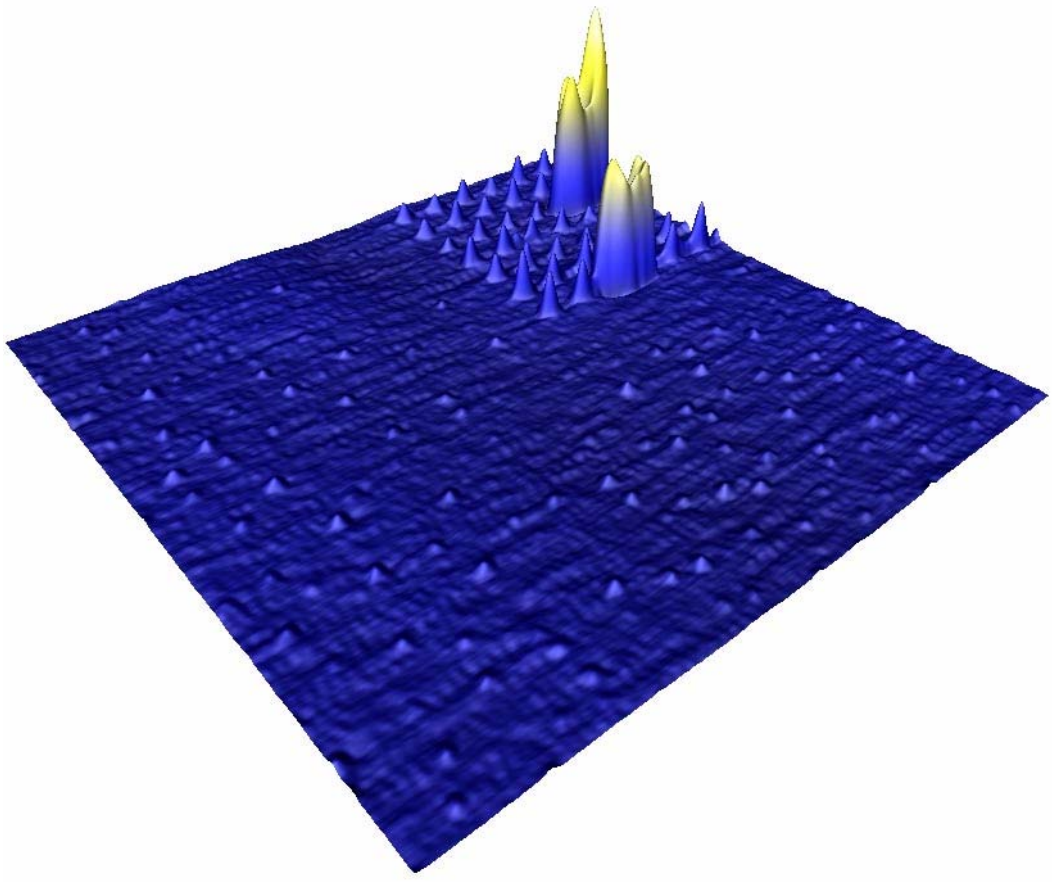

Figure 10-2: AFM image (5μm x 5 μm x 35 nm) showing co-existence of self-assembled and templated Ge islands.

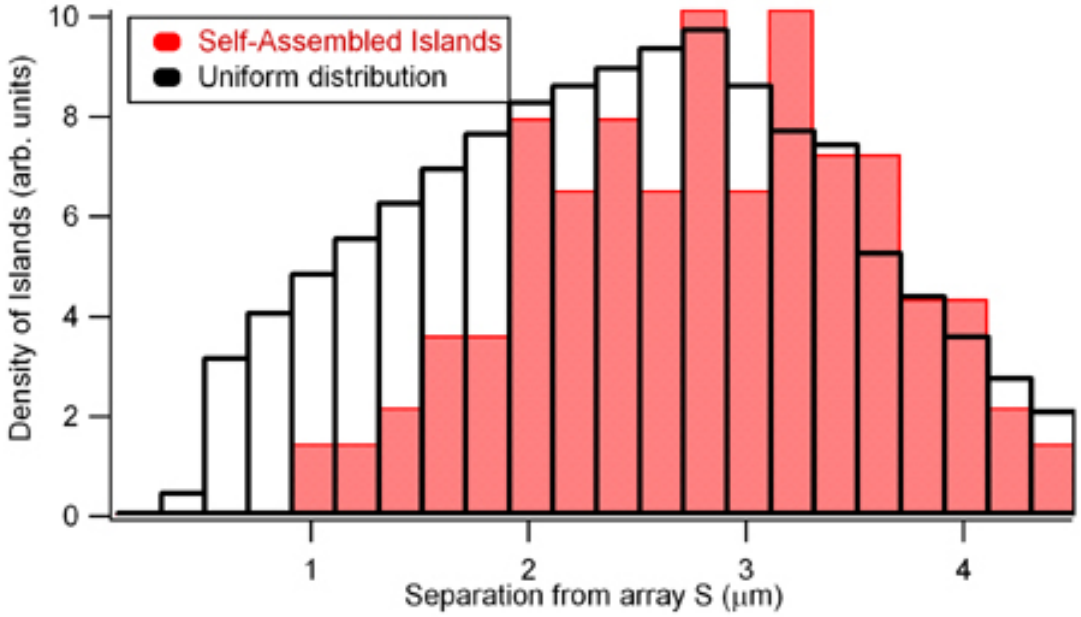

Figure 10-3: Distribution of self-assembled Ge island locations versus separation from SiC template boundary.

Further experiments are performed to determine the influence of various growth parameters such as the electron-beam exposure time t_{el}, ozone-treatment duration prior to UHV-transfer, amount of Ge deposited, Ge deposition rate and temperature, and post-deposition annealing conditions. Figure 10-4 shows the result of a pattern formed with t_{el}=18 ms exposures, followed by deposition of 2 ML of Ge at a rate R=0.06 Å/s, at a temperature where the Ge is highly mobile (T_1=T_2=830 K). The AFM image (Figure 10-4a) shows an irregular distribution of volumes; 99% of the observed islands exist on lattice sites defined by the SiC pattern, as evidenced by a Fourier transform of the AFM image (Figure 10-4b). The distribution of island volumes resembles those reported for self-assembled Ge islands on untemplated surfaces

[54,70,83,248]. Correlations between the sizes of the Ge islands are revealed by comparing the volume of a given island with that of its four nearest neighbors (Figure 10-4c). Larger islands exhibit a clear tendency to have smaller (and fewer) neighbors.

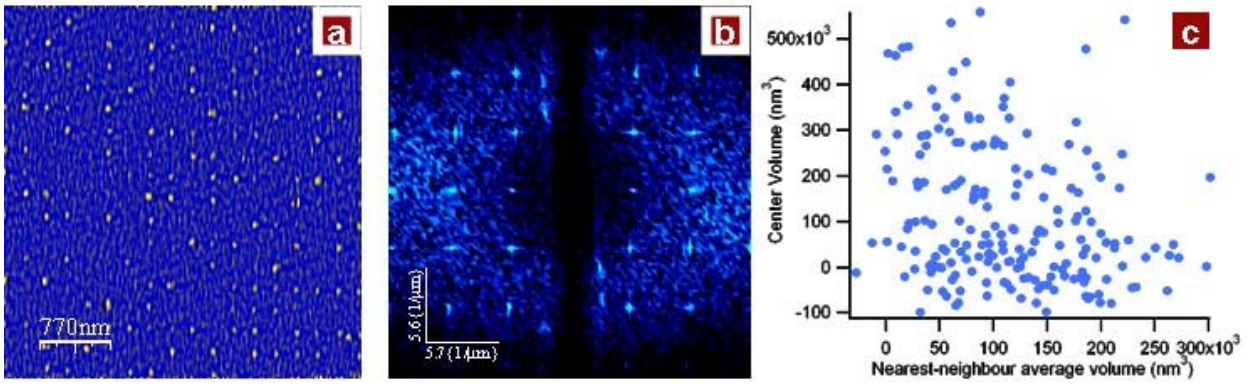

Figure 10-4: Templated Ge islands grown at T_1=T_2=830 K. a, AFM image of templated region. b, Fourier transform of AFM image, showing expected periodicity. c, Scatter plot of island volume versus average nearest neighbor volume, illustrating that larger islands tend to have smaller neighbors.

Separating the Ge deposition and annealing steps greatly sharpens the distribution of island sizes. Figure 10-5a shows a 20x20 array of carbon dots spaced by 35 nm (t_{el}=1 ms) and the resulting Ge islands (Figure 10-5b) grown under the following conditions: N_{Ge}=1 ML at R=0.06 Å/s, T_1=670 K; annealed at T_2=970 K for t_2=30 min. Except for isolated defects, no islands are observed in untemplated areas, i.e., outside the array or in interstitial regions. The averaged profile of the 400 islands (Fig. 4c) is Gaussian: $z(x) = h\exp(-(x/\sigma)^2)$, with h=9.2Å and σ=12.4 nm. Assuming a 4 nm radius of curvature for the non-contact Si probe [226], one obtains $\sigma' \approx 8$ nm for the islands. Each island contains ~2000 Ge atoms (Figure 10-6). Fluctuations are large (500 Ge atoms), the result of unavoidable statistical fluctuations as well as competition for Ge by nearest neighbors, i.e., Oswald ripening. The dot volume autocorrelation

shows that the small size variations are uncorrelated for the SiC dots (Figure 10-7a), but that slight anticorrelations exist for nearest and next-nearest neighbour Ge islands (Figure 10-7b). An analysis of the spatial location of the patterned islands shows that the islands form within 2 nm of their intended location.

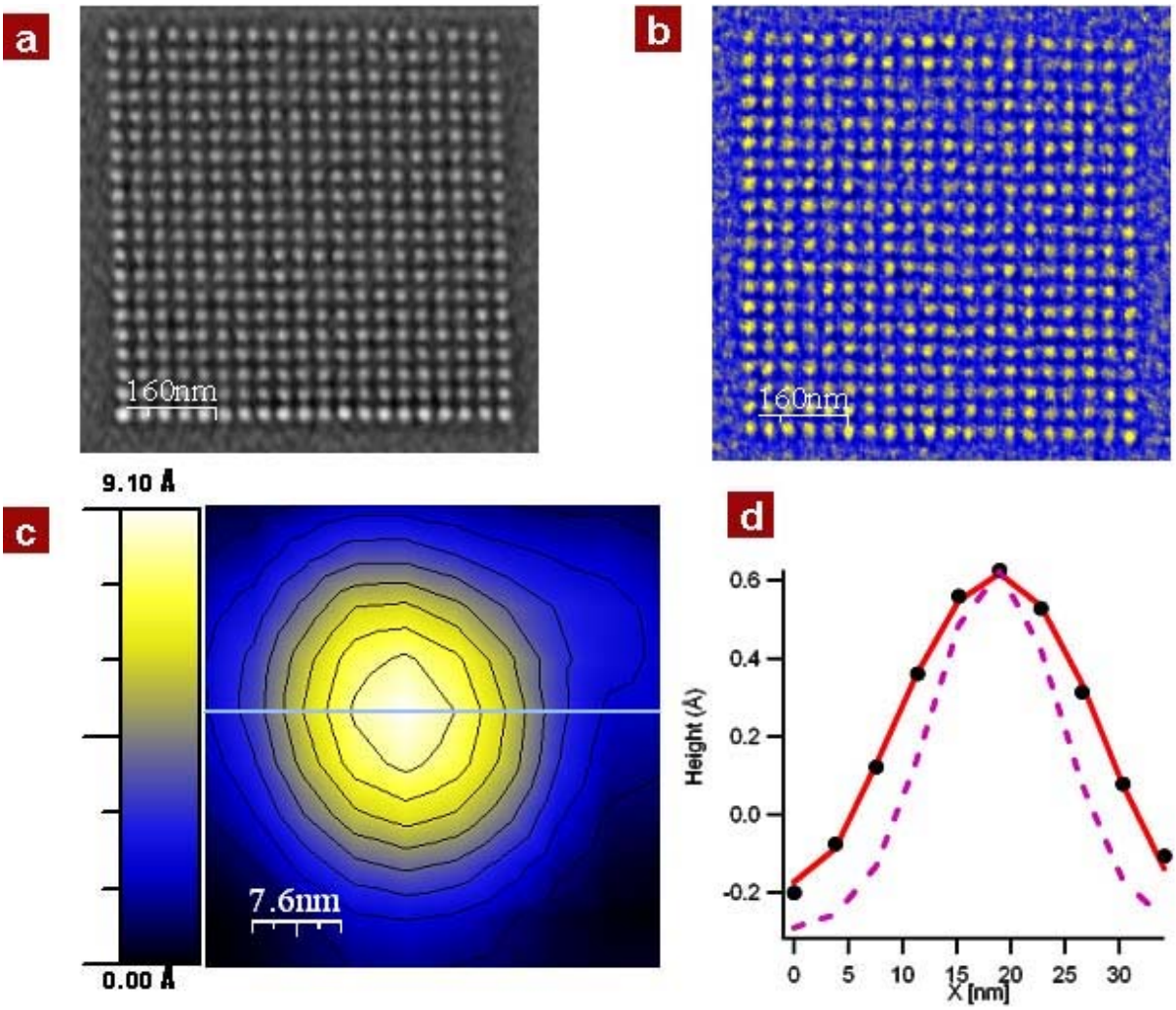

Figure 10-5: (a) AFM image of 20x20 array of SiC dots; (b) AFM image of 20x20 array of Ge islands on SiC template; (c) Average topographic profile of 400 Ge islands. Contours are separated by 1 Å; (d) Cross section of average profile, showing data (points), and a Gaussian fit (σ =12 nm). Dashed line shows deconvoluted profile (σ=8 nm).

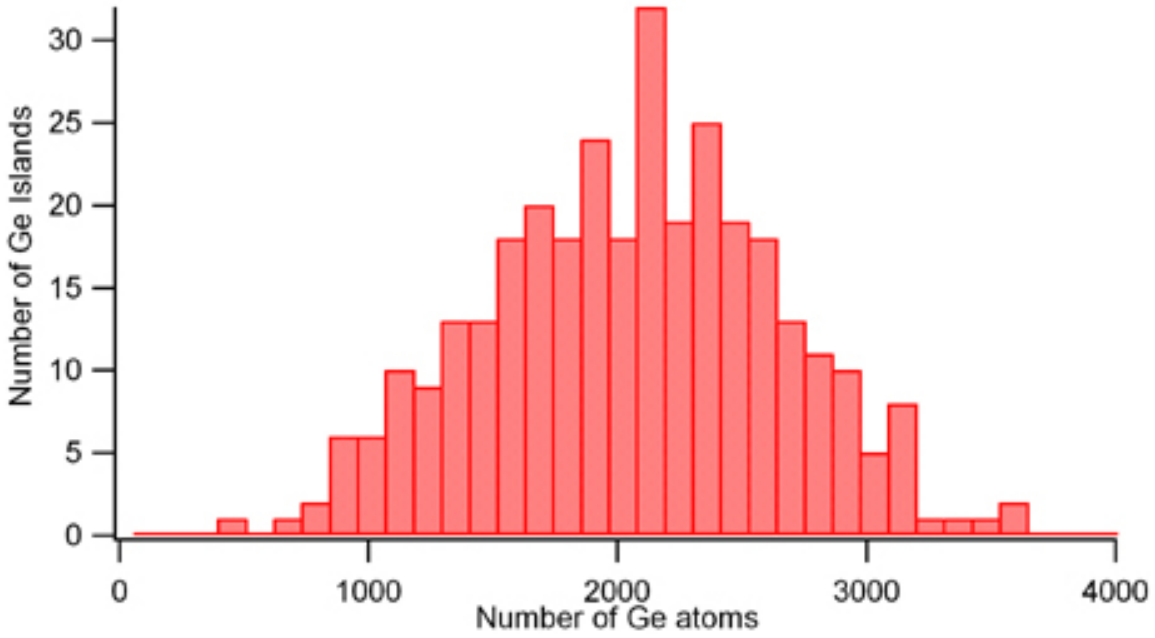

Figure 10-6: Histogram of number of Ge atoms per island for the 20x20 array shown in Figure 10-5.

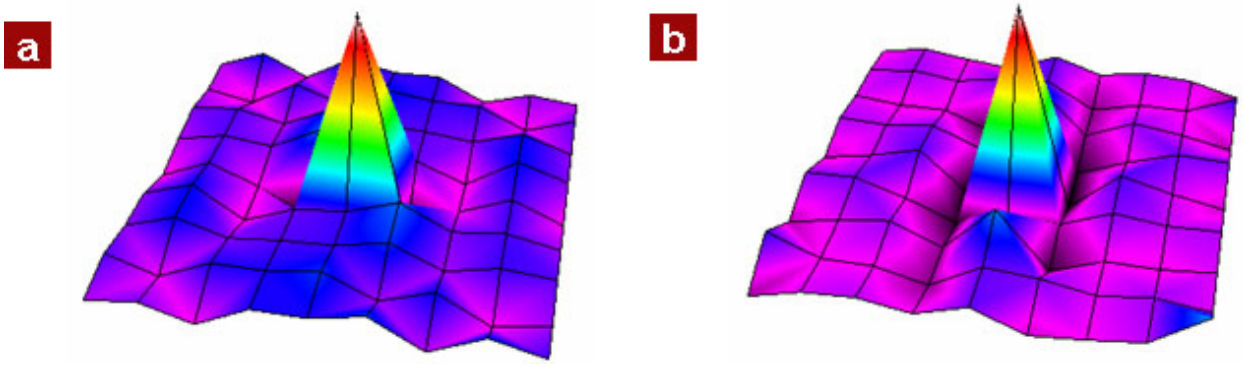

Figure 10-7: Autocorrelation of SiC dot and Ge island volumes. Graphs are normalized to unity, and each vertex represents a displacement by one lattice constant (35 nm). a, SiC dot autocorrelation. b, Ge island autocorrelation.

More experimental and theoretical work is required to understand the ultimate level of control with which Ge nanostructures can be created on Si(100) using the methods presented here. To become useful for quantum device architectures, it will be important to understand how Ge adatoms bond with the SiC sites, how the kinetic history of the Ge can be tailored to reduce island size fluctuations, and how their structure relates to electronic and optical properties. The sub-10 nm Ge islands demonstrated here are already interesting for quantum devices that work with single electrons and holes. Single-electron charging energies for sub-10-nm Ge islands are comparable to thermal energies [245], raising the prospect for single-electron devices that can operate at room temperature. The high precision with which the islands can be placed is critical for the engineering of dipolar and tunnel couplings for quantum cellular automata and quantum computing device architectures.

CONCLUSION

The work presented in this dissertation is a summary of the research conducted at the Surface Science Center, Department of Chemistry at the University of Pittsburgh.

As was shown, I contributed to the conception, design and development of a unique multiple probe scanning tunneling microscope combined with a scanning electron microscope. This instrument - the Nanoworkbench - operating under ultra-high vacuum conditions was experimentally tested in two ways which utilize the Z-direction resolution and also the X- and Y-direction resolution capabilities of the instrument:

1. We performed direct electrical measurements of the Z-direction motion of the interface in the oxidation of a metal (Al(111)) and a covalent solid (Si(100)) at room temperature with both molecular oxygen and nitrous oxide. The measurements agree with widely accepted models of metal and semiconductor oxidation with are based on kinetic measurements of the rate of oxidation. Kinetic measurements made by others provide only indirect evidence about the direction of the interface motion during oxidation.
2. We performed direct electrical measurements in the X- and Y- directions of the I/V properties of a SiO_2 surface on Si(100) in which a sub-micrometer dimension field-effect transistor action was demonstrated.

In addition, various surface preparation and surface analysis functions were demonstrated in the attached molecular beam epitaxy and analytical / preparation chambers.

The second part of this dissertation focused on Si/C/Ge systems. For optoelectronics and quantum computing architecture, it is desirable to be able to grow dense arrays of Ge islands on Si(100) with a very narrow size distribution and high control over the island spacing. We developed a new approach based on the formation of a template of ultra-small carbon dots patterned by electron-beam-induced deposition (EBID) in a high-resolution SEM. AES, XPS and TPD studies of carbon thin films deposited by EBID showed that upon UHV-annealing, the amorphous carbon thin film on Si(100) converts into SiC. These SiC arrays of dots are extremely sturdy and can be used as nucleation centers for subsequent Ge deposition, leading to the formation of Ge islands. The size and spacing of these Ge islands as well as the level of control we achieved in tailoring them is currently unmatched. These Ge islands arrays will be used for quantum computing architecture, in combination with a ferroelectric capping layer.

Following is a description of potential experiments that could be performed as a continuation of these research projects:

A very interesting experiment combining the multiple-probe capability of the NWB and our ability to pattern sub-10nm Ge dots would be the realization of a single-electron transistor device (SET) on an SOI substrate. One could investigate the influence of the Ge dot on the electrical conduction from source to drain. Ge will have weak scattering for electrons, and strong scattering for holes. So depending on the bias, we should see strong differences in the I-V characteristic depending on whether we have a Ge dot there or not. There is also the possibility of seeing conductance oscillations due to charging of the dot (i.e., Coulomb blockade). The experimental set-up is shown in Figure C-0-1. Ultra-small carbon dots can be patterned in the substrate, as well as carbon electrodes (see Figure C-0-2). The carbon electrodes will have sub-

micrometer dimensions and are required to precisely address the Ge dot in the center. Due to the sub-10nm size of the dot, it seems extremely challenging to address it directly with the four probes. After Ge deposition in UHV, a sub-10nm Ge dot is formed. Probes can be approached to make contact with the electrodes surrounding the Ge dot. The isolated dot is then coupled through tunneling to two probes while the third probe acts as a gate. The applied voltage V_{SD} between the source probe and the drain probe causes direct current, I, to flow, with electrons tunneling into and out of the Ge island. Since V=RI, the main contribution to the value of R arises from the process of electron tunneling from the source to the Ge island and from the Ge island to the drain.

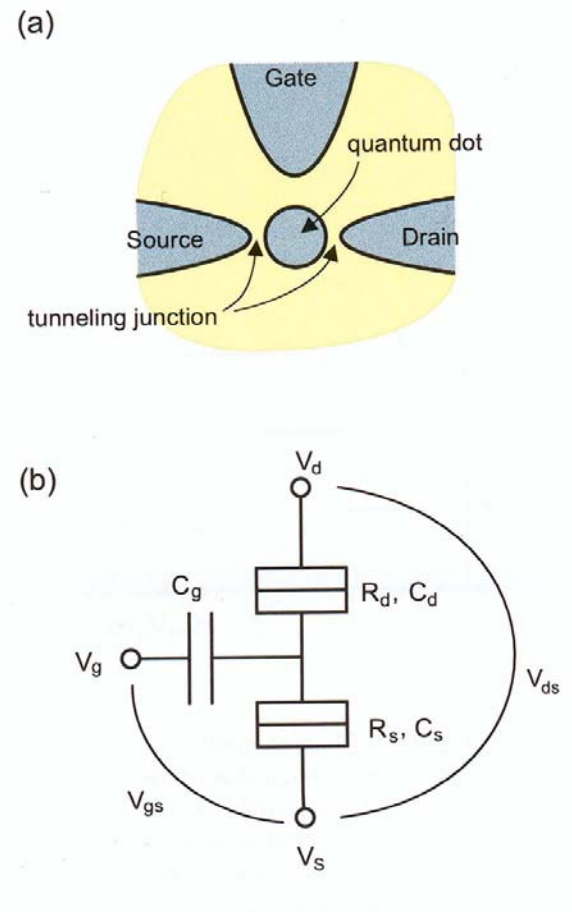

Figure C-0-1: (a) Schematic structure of single-electron transistor. (b) Equivalent circuit of single-electron transistor.

If we assume a Ge island of spherical shape and radius r, the capacitance is given by:

$$C = 4 \times \pi \times \varepsilon \times r \qquad \textbf{C-0-1}$$

where $\varepsilon/\varepsilon_0$ is the dimensionless dielectric constant of Ge, and $\varepsilon_0 = 8.8542 \times 10^{-12}$ F/m is the dielectric constant of the free space. For Ge, $\varepsilon/\varepsilon_0 = 16$ [250], which gives the value of $C = 1.78 \times 10^{-9} r$ with the radius r in meter. When a single electron is added or removed, the electrostatic energy E of the spherical capacitor of charge Q is changed by $\Delta E = eQ/C$, which corresponds to a change in potential $\Delta V = \Delta E/Q$. Therefore:

$$\Delta V = e/C \cong 0.09/r \quad \text{Volts} \qquad \text{(with r in nanometers)} \qquad \textbf{C-0-2}$$

.

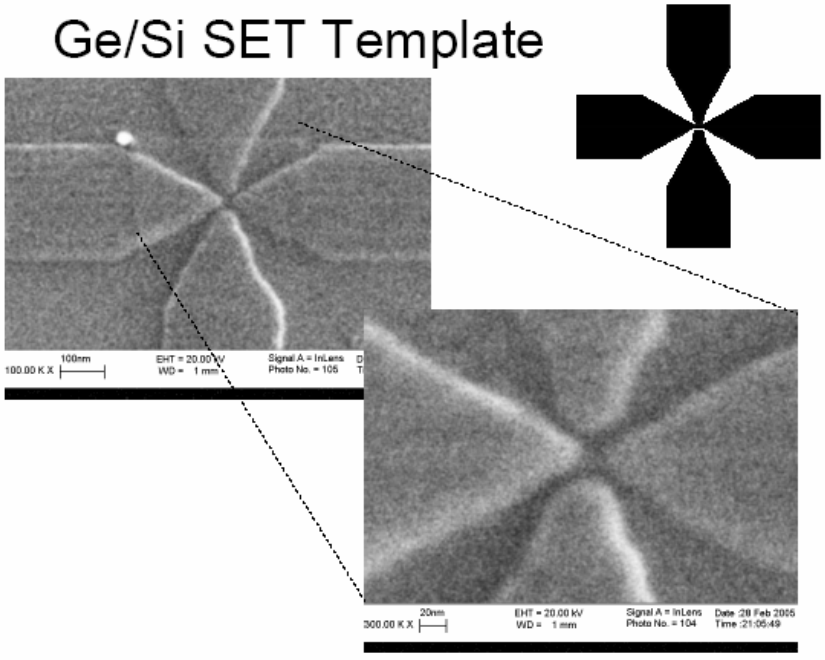

Figure C-0-2: SEM images of a preliminary SET structure patterned by EBID on a silicon-on-insulator sample. The spacing between the patterned electrodes is about 20nm. A dot – not visible on the SEM image – is patterned in the center of the four electrodes.

As shown in section 10, our Ge islands have sub-10nm dimension. Assuming a Ge island radius of 5nm, the equation gives a change in potential of 18mV.

One condition must be satisfied for the observation of the discrete nature of the single-electron charge transfer. The capacitor single-electron charging energy $e^2/2C$ (Coulomb energy) must exceed the thermal energy k_BT arising from the random vibrations of the atoms in the solid. This is the case for our system since $e^2/2C = 1.4 \times 10^{-13}$ J >> $k_BT = 4.14 \times 10^{-21}$ J (assuming a 5nm-radius Ge dot). Since this condition is met, the current will jump in increments every time the voltage value changes by the value defined in equation C-0-2. This can be seen in an I/V plot.

Additional experiments should also be performed to demonstrate the quantum nature of the Ge islands. These experiments include photoluminescence measurements and capacitance measurements.

The next step of development of the Ge/Si quantum dot structure will involve integration of the Ge island array with the ferroelectric material. It should be mentioned that the ferroelectric material has already been developed by the Schlom group at Pennsylvania State University and that integration experiments are under way.

APPENDIX

A1. Reproducible Electrochemical Etching of Tungsten Probe Tips

As was shown in section 5, the Nanoworkbench is based on a multiple-probe STM system. Sharp tips are required in order to perform STM and conductivity measurements at the smallest possible scales. In addition, one needs to be able to prepare fresh tips quickly and reproducibly.

A1.1 Abstract

An electrochemical procedure in KOH electrolyte has been developed to reproducibly produce ~5 nm radius tungsten probe tips. It has been found that a spurious electrochemical etching process, driven by the natural potential difference between an Ir electrode and the W tip, causes rapid tip blunting at the end of the electrochemical etching period. By electrically reversing this potential difference within 500 ns following tip separation, the blunting process is eliminated yielding sharp tips with varying cone angles.

A1.2 Introduction

The preparation of ultra sharp tips is essential for nanometer probe techniques, including STM. Many tip preparation techniques have been developed over the years such as mechanical cutting or electrochemical etching. Here, we report the discovery of a post-etching phenomenon

during electrochemical etching, which causes tip blunting. We have studied this effect and developed a procedure to prevent such tip blunting. This technique allows the reliable and reproducible fabrication of ultra sharp tips, with a probe radius of 5 nm or less.

A1.3 Experimental Part

Tips are prepared from tungsten wire (Goodfellow, 0.38 mm diameter, 99.95%) and electrochemically etched using the standard "drop off" technique [251-257]. As shown in Figure A1-0-1, the tungsten wire is immersed in a droplet of KOH solution (etchant) held by an iridium loop (Alfa Aesar, 99.8%). A voltage is applied between the tip and the loop, so that the tip is the anode and the loop is the cathode. The electrochemical etching reaction then takes place [258].

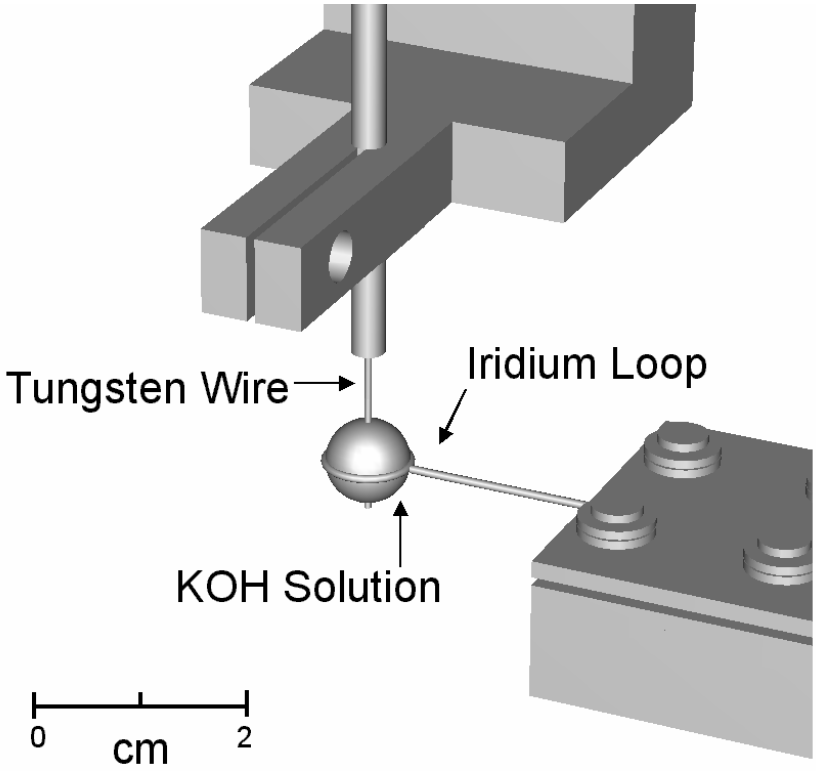

Figure A1-0-1: Electrochemical apparatus for tungsten tip etching.

The tungsten wire is etched in 2 steps. In the first step (coarse etching), a DC voltage (typically 3 V) is applied between the electrodes using a 2 M KOH etchant solution. In the second step (fine etching), a DC voltage of 0.5 V is applied using a 0.1 M KOH solution as the etchant. We use a special power supply for fine etching. As shown in Figure A1-0-2, the current steadily decreases during fine etching. At the end of the etching, a discontinuity of current occurs as the lower part of the wire drops away. The fine etching power supply records this discontinuity and automatically switches off the applied voltage in 500 ns. We added a feature to this power supply. Instead of simply switching off at the end of the etching period, the power supply may also reverse the potential applied between the electrodes. The user can set up the power supply to select between these two options. During etching, the potential V_1 is applied between the electrodes. At the end of etching, the potential V_2 is either the reverse potential or the natural potential, which exists between tungsten and iridium in the KOH electrolyte.

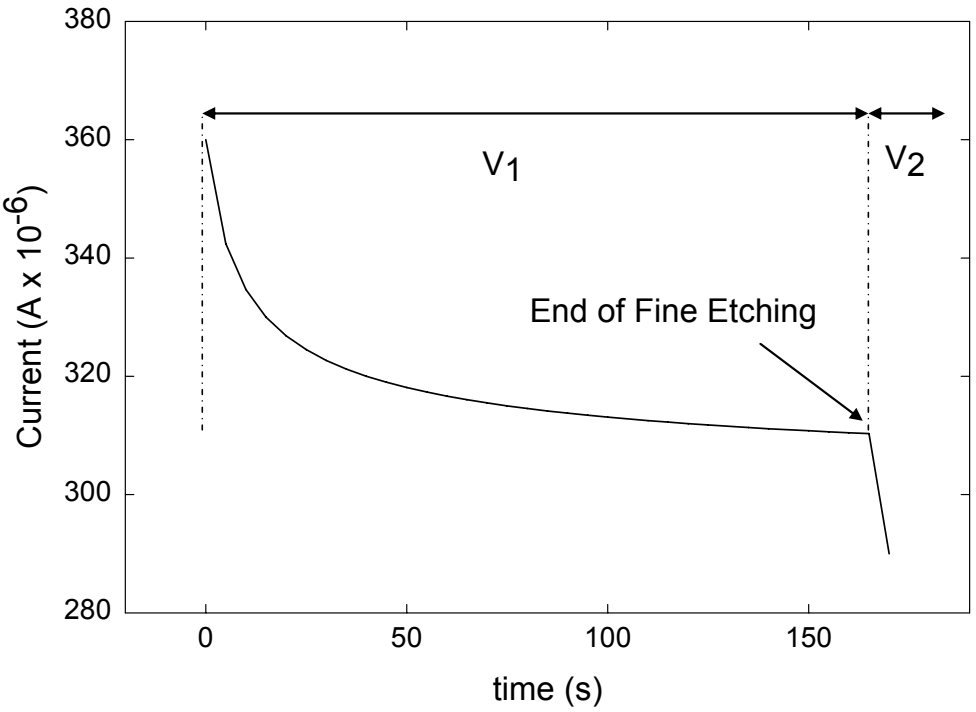

Figure A1-0-2: Evolution of the cell current during fine etching. The discontinuity in current corresponds to the drop of the lower part of the wire as the etching ends, and activates the automatic power supply switch-off.

After proper cleaning (tips are rinsed with deionized water and methanol after each etching step), tips are characterized by SEM (Cambridge S-90) and by TEM (Hitachi H-800). SEM and TEM images are transferred to a computer and analyzed. We define two parameters to describe a tip, as shown in the inset of Figure A1-0-3: the tip radius and the tip cone angle. We approximate the tip end as a sphere whose diameter can be precisely determined by computer image analysis.

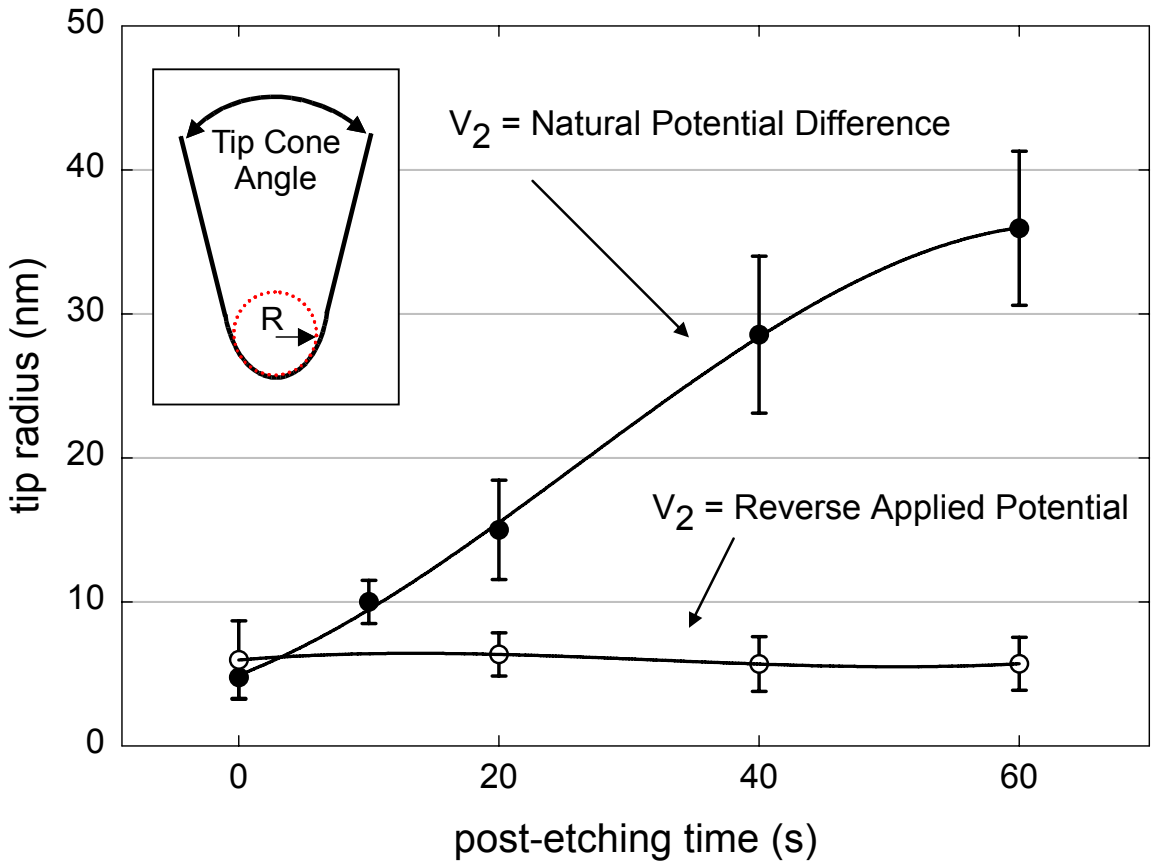

Figure A1-0-3: Comparison of tip radius evolution for tips prepared with potential V_2 as natural bias or reverse bias. Tips have a cone angle of 5°. Inset: Definition of tip radius and tip cone angle.

In Figure A1-0-3, we present measurements of the radius of the tips as a function of the time spent in the etching solution at potential V_2. In the first case (flat curve), V_2 corresponds to the reverse applied potential, and in the second case V_2 corresponds to the natural potential difference between the two electrodes. Time $t = 0$ corresponds to the end of the fine etching. At each etching time, the tip was immediately rinsed with deionized water and withdrawn from the solution. The tips are then characterized by TEM and the tip radius measured. Each data point corresponds to an average of at least 5 tips. The tip cone angle is about 5° for each tip in Figure A1-0-3. A rapid increase of the tip radius with time of "post-etching" under natural bias is

observed. This increase cannot be solely attributed to the formation in air of an oxide layer since the oxide layer grows by only about 2 nm during two days of atmospheric exposure[255] after the tip preparation, whereas the tip radius increases by more than 30 nm for a tip after 60 s of post-etching under the natural potential difference in our case. We believe that this effect is due to electrochemical action under the natural bias occurring between the tungsten wire and the iridium loop when the power supply is switched off. The literature difference between the work function of tungsten and the work function of iridium is 800 mV [259] (for reasonably clean surfaces). The measured open circuit potential difference during an experiment is 420 mV, with the W tip being positive with respect to the Ir electrode.

In Figure A1-0-3, we note that the use of the reverse applied potential, V_2, following the tip separation, results in complete retardation of the increase of the tip radius which occurs when the natural open circuit potential exists.

In Table A1-0-1 we provide data for a number of post-etching experiments under the natural bias for tips with various cone angles, ranging from 5° to 35°. The same effect is observed: a rapid increase of the tip radius occurs for all cone angles. It is interesting to notice that the magnitude of the blunting effect increases for increasing tip cone angles.

These experiments demonstrate that the electronic shutoff of the power supply upon tip separation is not by itself a sufficient condition for the production of very sharp tips. If the power supply switches off but the tip is left immersed at the natural potential difference in the solution, the tip radius will then increase with time and the tip will have a blunted-end shape. These observations provide an explanation for a remark by Mendez et al. stating that the lower tip, which falls away, is always sharper than the upper one[254]. The lower tip does not spend as much

time as the upper part in the solution after the completion of the etching since after it falls out of the droplet it is not subject to further etching due to the natural bias between W and Ir in KOH solution.

Table A1-0-1: Effect of cone angle on the rate of tip blunting at the natural potential difference.

Post-etching time (s)	Tip radius (nm)			
	cone angle 5º	cone angle 10º	cone angle 25º	cone angle 35º
0	5	5	5	5
10	10	15	25	30
20	20	25	36	40
40	39	43	48	50
60	46	55	55	59

In Figure A1-0-4, we present TEM images showing the effect of post-etching. Figure A1-0-4a shows first the image of a sharp tip, prepared by applying a reverse potential at the end of Figure A1-0-2. The discontinuity in current corresponds to the drop of the lower part of the wire as the etching ends, and activates the automatic power supply switch-off. The tip radius is determined to be 3.5 nm. After TEM characterization, the tip was dipped again in the etching solution for 20 s with potential V_2 corresponding to the natural electrodes bias. A second TEM image shows that the radius increases to 13 nm. The same operation is repeated for an additional 20 s. The tip radius jumps to 27 nm. Figure A1-0-4b shows a typical example of a tip prepared

by applying a reverse potential at the end of the etching. This very sharp tip has a radius less than 4 nm.

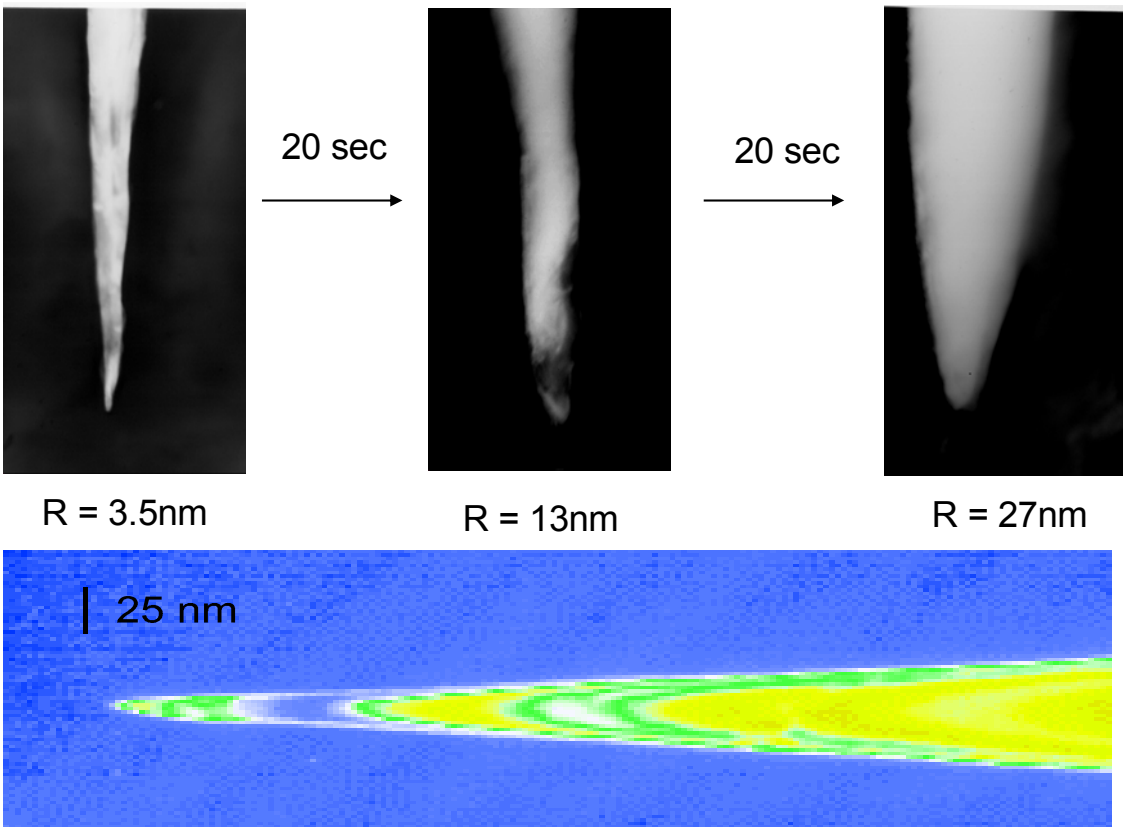

Figure A1-0-4: (a) Images showing a sharp tip, the same tip after 20 s post-etching, and the same tip after 40 s post-etching. Radius increases from 3.5 nm to 13 nm to 27 nm. (b) TEM image of a typical tip prepared by reverse bias technique. Tip radius is less than 4nm.

It is important to notice that applying a reverse potential does not eliminate the need for cleaning a tip before use. Cleaning remains a necessary step to remove the contaminants. Instead, the reverse bias freezes any further electrochemical reaction caused by the natural electrode bias in KOH solution.

Figure A1-0-5 presents a schematic of the post-etching process. After fine etching, if the reverse bias is applied, a sharp tip can be produced. This corresponds to position 1 on the schematic and a tip radius of about 5 nm. As the tip is dipped again in the solution (power supply off, potential V_2 is the natural cell potential) the tungsten wire is etched down moving from condition 1 to condition 5, depending on the time of storage in the electrolyte at the natural potential difference. The electrical current flowing between the W tip and the Ir electrode under the natural bias condition was measured using an electrometer and found to be in the range 10^{-8} to 10^{-7} A. For the geometrical blunting process shown in Figure A1-0-5, the calculated average current to etch from a 3.5 nm radius to a 35 nm radius in 60 s (cone angle 5°) is only of the order of 10^{-12} A, assuming a redox process producing W^{6+} as $WO4^{2-}$. On the basis of this 4-5 order of magnitude ratio of currents, the schematic etching process shown in Figure A1-0-5 must be accompanied by electrochemical etching along the shank of the tip.

Additionally, on the basis of these studies, we developed a second technique for preventing further etching due to the natural bias: we added an electrically actuated valve connected to a reservoir of deionized water. When the power supply switches off, the valve opens quickly, releasing the water. The tip is then automatically rinsed and no further etching occurs. This system is not as efficient as the automated bias reverse, since the time required for the automated rinsing is about 2 s compared to 500 ns for freezing the electrochemical reaction by reversing the electrical bias.

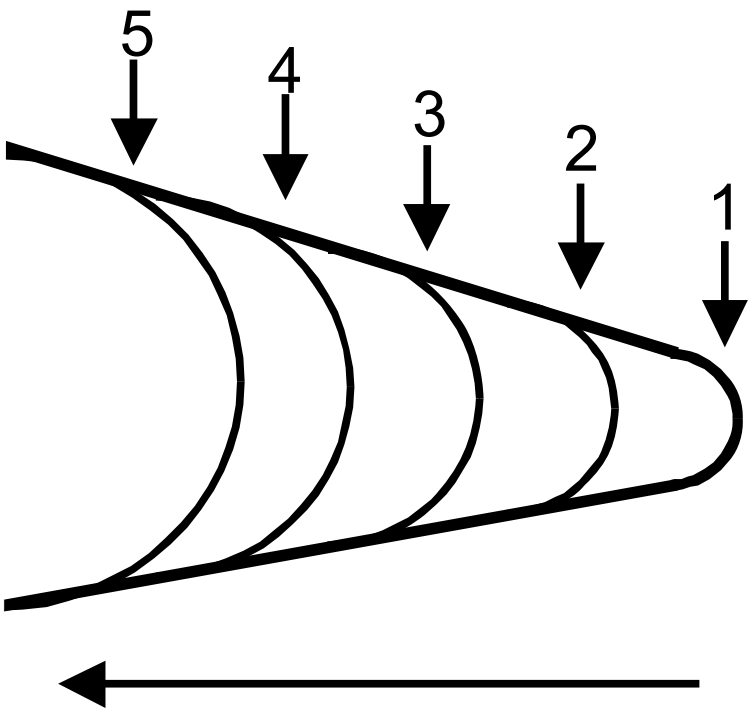

Figure A1-0-5: Schematic of tip blunting under the natural bias due to post-etching after tip separation. In the case of a tip with a cone angle of 5°, position 1 corresponds to the etched tip with a tip radius of ~5 nm, position 2 corresponds to the tip radius after 10 s post-etching (tip radius ~10 nm), position 3 corresponds to the tip radius after 20 s post-etching, and so on.

A1.4 Conclusion

In conclusion, we have developed a simple procedure for the preparation of very sharp tungsten tips with radius of 5 nm or less. This method produces tips in a very controlled and reproducible manner. These tips are useful for STM and other probe applications.

A2. Measuring the Temperature of a Sample with a Pyrometer

Emissivity is defined as the ratio of the energy radiated by an object at a given temperature to the energy emitted by a perfect radiator, or blackbody, at the same temperature. The emissivity of a black body is 1.0. All values of emissivity fall between 0.0 and 1.0.

The temperature of a hot object can be estimated by measuring its radiant power at a specific wavelength λ. When an object is a perfect blackbody, its radiant power per unit area, $W_b(\lambda, T)$ is described by Planck's law:

$$W_b(\lambda,T) = \frac{2\pi hc^2}{\lambda^5} \times \left[\frac{1}{\exp\left(hc/\lambda kT\right) - 1}\right] \qquad \textbf{A2-0-1}$$

where λ is the wavelength, T is the temperature, c is the speed of light, k is Boltzmann's constant, and h is Planck's constant. When $hc/\lambda kT >> 1$, this equation can be simplified:

$$W_b(\lambda,T) = \frac{2\pi hc^2}{\lambda^5} \times \exp\left(-hc/\lambda kT\right) \qquad \textbf{A2-0-2}$$

The radiant power from a non-blackbody object is smaller than that from a blackbody. The ratio of the radiant power of the non-blackbody, $W_n(\lambda, T)$ to that of a blackbody, $W_b(\lambda, T)$, is termed the emissivity $\varepsilon(\lambda, T)$:

$$W_n(\lambda,T) = W_b(\lambda,T) \bullet \varepsilon(\lambda,T) \qquad \textbf{A2-0-3}$$

The temperature is measured by collecting radiance in a narrow band (50nm) at the same wavelength (865nm) where also the emissivity is measured with the help of a laser. In a first step, this measured radiance is corrected with the measured emissivity ε to a black body radiance as shown in equation A2-0-3.

From this black body radiance the instrument calculates then according to Planck's law the true temperature T of the target as seen in equation A2-0-1

Once the radiance is corrected to a black body radiance all temperature calculations use the same above temperature formula.

A3. Quartz Crystal Microbalance

A3. 1 Experimental

A quartz crystal microbalance is an ultra-sensitive mass sensor. As seen in the schematic of Figure A3-0-1, it is composed of a piezoelectric quartz crystal material sandwiched between a pair of gold electrodes. When the electrodes are connected to an oscillator and an AC voltage is applied over the electrodes the quartz crystal starts to oscillate at its resonance frequency due to the piezoelectric effect.

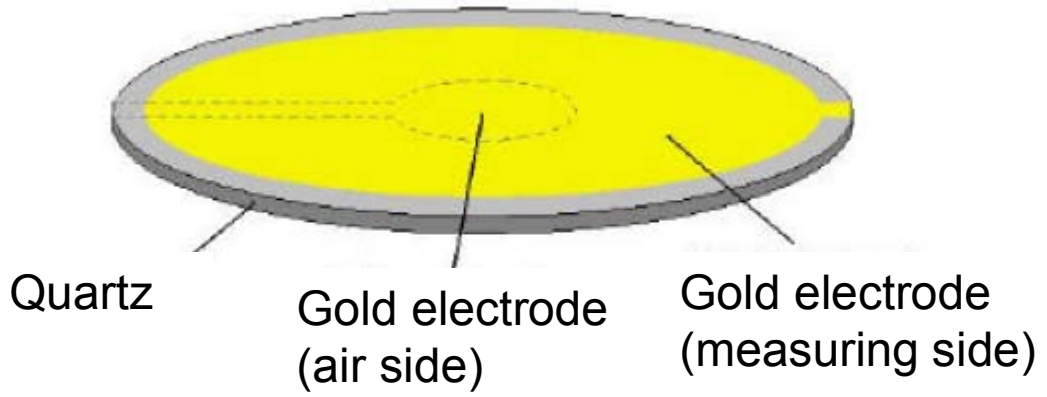

Figure A3-0-1: Schematic of a quartz crystal oscillator.

A3. 2 Theory

The quartz crystal microbalance uses the resonant frequency of an exposed quartz crystal to sense the mass of deposited films attached to its surface. In 1959 Sauerbrey showed that the

frequency shift of a quartz crystal resonator is directly proportional to the added mass[260]. If a rigid layer is evenly deposited on one or both of the electrodes the resonant frequency will decrease proportionally to the mass of the adsorbed layer according to the Sauerbrey equation:

$$\Delta f = -\left[2 \times f_o^2 \times \Delta m\right] \div \left[A \times \left(\rho_q \mu_q\right)^{1/2}\right] \qquad \textbf{A3-0-1}$$

Where the terms used in the equation are defined as:

Δf = measured frequency shift

f_0 = resonant frequency of the fundamental mode of the crystal

Δm = mass change per unit area (g/cm^2)

A = piezo-electrically active area

ρ_q = density of quartz, 2.648 g/cm^3

μ_q = shear modulus of quartz, 2.947 x 10^{11} $g/cm.s^2$

By measuring the period of ~ 1.2 million oscillations of the sensor signal and using a stable reference clock, an extremely accurate frequency shift value is derived. Four times per second, a new value of frequency is determined and used to update the above equation. Typically the accuracy of a quartz crystal microbalance is 0.1Å/s or about 1ng.

A4. Calculation of the Hertzian Contact Between a Pt/Ir Tip and Al(111)

The models used for the calculation are shown in Figure A4-0-1. The end of the PtIr tip is modeled as a sphere of radius R (left side) held by a lever with a bending force constant, k, and this sphere creates an indentation of depth i upon contact with the Al(111) surface (right side).

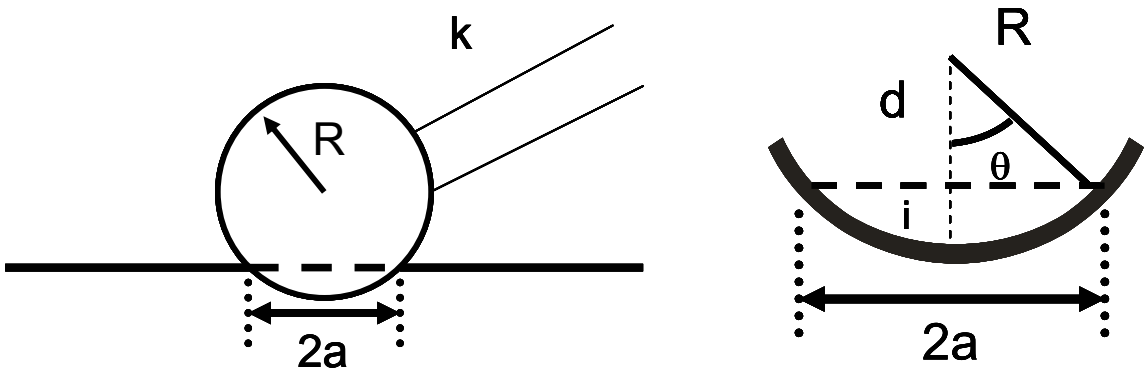

Figure A4-0-1: Schematic of indentation configurations used for the calculation of the hertzian contact between a Pt/Ir tip and A(111) crystal. Left: the end of the tip is modeled as a sphere of radius R. Right: the sphere of radius R makes an indentation of depth i in the Al(111) surface.

For a sphere of radius R, assuming a Hertzian contact[261]:

$a = \left(\frac{3FR}{2\gamma_{Al}} \right)^{1/3}$ = radius of indentation, with γ_{Al} being Aluminum's Young's modulus. **A4-0-1**

Using Figure A4-0-1 left, we can write that:

$d + i = R$, and $\frac{a}{d} = \tan\theta$ and $\frac{a}{R} = \sin\theta$

Therefore:

$$i = R - d = R - a/\tan\theta = R - a\cos\theta/\sin\theta = R - R\cos\theta = R(1-\cos\theta) \qquad \textbf{A4-0-2}$$

For small values of θ, $\cos\theta = \left(1 - \theta^2/2 + ...\right)$

Therefore $i \cong \frac{R\theta^2}{2}$

But since for small values of θ, $\theta = \frac{a}{R} \rightarrow \theta^2 = \frac{a^2}{R^2}$

$i \cong \frac{R\theta^2}{2} \cong \frac{Ra^2}{2R^2} \cong \frac{a^2}{2R}$, and using the value of a defined earlier (see equation A4-0-1):

$$i \cong \frac{1}{2R}\left(\frac{3FR}{2\gamma_{Al}}\right)^{2/3} \cong \frac{1}{2}\left(\frac{3F}{2\gamma_{Al}}\right)^{2/3}\left(\frac{1}{R}\right)^{1/3} \qquad \textbf{A4-0-3}$$

We now let ΔZ be the vertical deflection of the tip as shown in Figure A4-0-2.

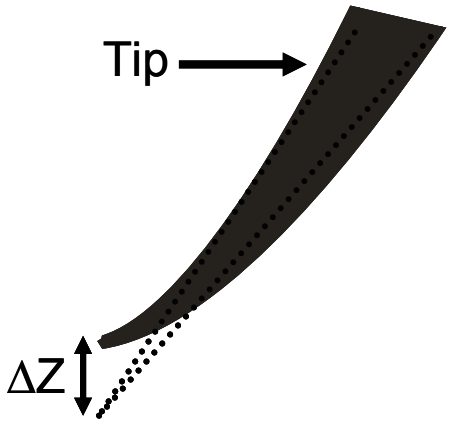

Figure A4-0-2: Definition of ΔZ: the vertical deflection of the tip upon bending.

Since ΔZ=F/k, with k the force constant for the lever holding the sphere,

$F^{2/3} = (k\Delta Z)^{2/3}$

And finally: $i = \frac{1}{2}(k\Delta Z)^{2/3} \bullet \left(\frac{1}{R}\right)^{1/3} \bullet \left(\frac{3}{2\gamma_{Al}}\right)^{2/3}$ **A4-0-4**

Equation A4-0-4 can be investigated by parametrization as shown in Table A4-0-1. The value of i/ΔZ is calculated over a wide range of values of k (see Table A4-0-1).

Therefore this parametrized calculation shows that for a large range of the force constant, k, the ratio i/ΔZ is always less than 10^{-3} for k < 10Nm^{-1}.

We therefore conclude that the bending of the STM tip upon interaction with the surface at a 45º angle prevents significant indentation of the Al(111) surface.

Table A4-0-1: Deflection ΔZ and penetration i

k (N.m^{-1})	ΔZ (m)	i(m)	i/ΔZ
0.05	10^{-10}	5.27 x 10^{-15}	5 x 10^{-5}
0.01	10^{-10}	1.80 x 10^{-15}	2 x 10^{-5}
0.01	100 x 10^{-10}	3.88 x 10^{-14}	3 x 10^{-6}
0.01	1000 x 10^{-10}	1.80 x 10^{-13}	2 x 10^{-6}
0.01	10^{4} x 10^{-10}	8.37 x 10^{-13}	8 x 10^{-7}
1	10^{-10}	3.88 x 10^{-14}	4 x 10^{-4}
10	10^{-10}	1.80 x 10^{-13}	1.8 x 10^{-3}
10	100 x 10^{-10}	3.88 x 10^{-12}	4 x 10^{-4}
1000	10^{-10}	3.88 x 10^{-12}	4 x 10^{-2}
1000	1000 x 10^{-10}	3.88 x 10^{-10}	4 x 10^{-3}

A5. Details for Mott's Calculation of the Growth Rate of an Oxide Film in the Logarithmic Limit

$$\frac{dx}{dt} = Ae^{\beta/x}$$

$$dt = \frac{1}{A}e^{-\beta/x}dx$$

$$\int_0^t dt = t = \frac{1}{A}\int_0^x e^{-\beta/x}dx$$

$$At = \int_0^x e^{-\beta/x}dx$$

The approximation solution for x << β:

$At \cong \frac{x^2}{\beta}e^{-\beta/x}$ from reference [10].

$$\frac{x^2}{\beta}e^{-\beta/x} \cong \int_0^x e^{-\beta/x}dx$$

$$\frac{d}{dx}\left(\frac{x^2}{\beta}e^{-\beta/x}\right) = \frac{x^2}{\beta}\cdot\frac{\beta}{x^2}e^{-\beta/x} + \frac{2x}{\beta}e^{-\beta/x} = e^{-\beta/x}$$

Since x << β we can neglect $\frac{2x}{\beta}e^{-\beta/x}$,

and therefore $e^{-\beta/x} \cong e^{-\beta/x}$.

For the growth equation,

$At \cong \frac{x^2}{\beta}e^{-\beta/x}$;

$$\ln A + \ln t = \ln\frac{x^2}{\beta} - \frac{\beta}{x}$$

$$\frac{\ln A}{\beta} + \frac{\ln t}{\beta} = \frac{1}{\beta}\ln\frac{x^2}{\beta} - \frac{1}{x}$$

And therefore:

$$\frac{1}{x} = \frac{-\ln A}{\beta} - \frac{\ln t}{\beta} + \frac{1}{\beta}\ln\frac{x^2}{\beta}.$$

If we set $x^2 \rightarrow x_L^2$ when t is near saturation time, then in this limit, near saturation oxide film thickness, x_L,

$$\frac{1}{x} = C_1 - C_2 \ln t + \frac{1}{\beta}\ln\frac{x_L^2}{\beta}$$

Since $\frac{1}{\beta}\ln\frac{x^2}{\beta}$ is nearly a constant for $x \rightarrow x_L$,

Therefore:

$$\frac{1}{x_{near x_L}} \cong C_3 - C_2 \ln t$$

The growth equation applies near the saturation level of the oxide thickness.

CURRICULUM

Education

- Aug. 1998 - Present University of Pittsburgh, Pittsburgh, PA – USA

Department of Chemistry – Surface Science Center - Advisor: Professor John T. Yates, Jr.

Thesis: "Production and Characterization of Novel Nanostructure Materials".

- Sept. 1995 – Jul. 1998 Ecole Supérieure de Chimie, Physique, Electronique de Lyon (CPE Lyon – Institute for Chemistry, Physics and Electronics) - FRANCE

  Bachelor of Science in Chemistry

  Bachelor of Science in Chemical Engineering

  Elective : Catalysis

- Sept. 1992 – Jul. 1995 Classes Préparatoires aux Grandes Ecoles, Lycée Claude Fauriel, St-Etienne - FRANCE

Publications from this work:

- O. Guise, J. Ahner, J.T. Yates, Jr., V. Vaithyanathan, D.G. Schlom and J. Levy: Patterning of sub-10nm Ge Islands on Si(100) by Directed Self-Assembly, to be submitted.
- O. Guise, J. Levy and J.T. Yates, Jr.: Direct Measurement of Atom Transport Directions at the Interface in the Oxidation of Metals and Covalent Solids- Al(111) and Si(100) Oxidation with O_2 at 300K, Submitted to Thin Solid Films, March 2005.

- O. Guise, H. Marbach, M.-C. Jung, J. Levy, J. Ahner, and J. T. Yates, Jr. : Development and Performance of the Nanoworkbench: a Novel Toolset for Electrical Conductivity Measurements down to sub-micrometer Scales, , Rev. Sci. Instrum. 76 pp 045107-1 – 045107-8, 2005
- O. Guise, H. Marbach, J. Ahner, J. Levy and J. T. Yates, Jr.: Electron-beam Induced Deposition of Carbon Films on Si(100) using Chemisorbed Ethylene as a Precursor Molecule. Surface Science 571 (1-3) pp 128-138, 2004.
- O. Guise, J. Levy, J. Ahner and J. T. Yates, Jr.: Formation and Thermal Stability of sub-10nm Carbon Templates on Si(100). Applied Physics Letters 85(12) 2004.
- O. Guise, J. Ahner, J. Levy and J. T. Yates, Jr.: Imaging, Manipulating and Analyzing with Nanometer Precision: Applications of the Nanoworkbench. MRS Proceedings GG3.3.1 Vol. 803, 2004.
- O. Guise, J. Ahner, M.-C. Jung, P. Goughnour and J. T. Yates, Jr.: Reproducible Electrochemical Etching of Tungsten Probe Tips. Nanoletters. 2(3): 191-193, 2002

Conference Presentations

- "Oxide-Semiconductor Materials for Quantum Computation", O. Guise, J. Ahner, J.T. Yates, Jr., V. Vaithyanathan, D. Schlom, M. Flatte, S. Hellberg and J. Levy, DARPA QUIST 2005 – St Augustine, FL - Oral
- "Directed Self-Assembly of Ultra-Small Ge Quantum dots on Si(100)", O. Guise, J. Ahner, J.T. Yates, Jr., V. Vaithyanathan, D. Schlom and J. Levy, DARPA QUIST 2005 - St Augustine, FL - Poster

- "UHV Nanoworkbench and the 'Roaming' Field Effect Transistor", O. Guise, J. Levy, J. Ahner and J.T. Yates, Jr. – APS 2005 – Los Angeles, CA - Oral
- "Directed Assembly of Ultra-Small Ge Quantum Dots on Si(100)", O. Guise, J. Ahner, H. Marbach, J. Levy, and J.T. Yates, Jr. – APS March 2004 – Montreal, Canada – Oral
- "Imaging, Manipulation, and Analyzing with Nanometer Precision: Application of the Nanoworkbench", O. Guise, J. Ahner, H. Marbach, J. Levy, and J.T. Yates, Jr. – MRS Dec. 2003 – Boston, MA – Oral
- "Ultra-small Carbon Dot Patterns for directed Ge quantum dot Growth", O. Guise, J. Ahner, H. Marbach, J. Levy, and J.T. Yates, Jr. – ACS Regional Oct. 2003 – Pittsburgh, PA – Poster
- "Imaging, Manipulation, and Analyzing with Nanometer Precision: Application of the Nanoworkbench", O. Guise, J. Ahner, H. Marbach, J. Levy, and J.T. Yates, Jr. – Rutgers University, NJ - Oct. 2003 – Oral
- "Ultra-small Carbon Dot Pattern for directed Ge quantum dot Growth", O. Guise, J. Ahner, H. Marbach, J. Levy and J.T. Yates, Jr. – DARPA QUIST June 2003– Beverly Hills, CA – Poster
- "Ultra-small Carbon Dot Patterns for directed Ge quantum dot Growth", O. Guise, J. Ahner, H. Marbach, J. Levy, and J.T. Yates, Jr. – APS March 2003 – Austin TX – Oral
- "The Nanoworkbench", O. Guise, J. Ahner, M.C. Jung, H. Marbach, J. Levy, and J.T. Yates, Jr. – APS March 2003 – Austin TX – Oral
- "Germanium Quantum Dots – Growth and Investigation Using the Nanoworkbench", O. Guise, J. Ahner, H. Marbach, J. Levy and J.T. Yates, Jr. – Pitt Symposium Dec. 2002– Pittsburgh, PA – Poster

- "Germanium Quantum Dots – Growth and Investigation Using the Nanoworkbench", O. Guise, J. Ahner, H. Marbach, J. Levy and J.T. Yates, Jr. – SPINS Meeting - Oct. 2002– Delray Beach, FL – Poster
- "The Nanoworkbench", O. Guise, M.-C. Jung, J. Ahner, and J.T. Yates, Jr. – NAS Colloquium - May 2001– Washington, DC – Poster

Awards

- Materials Research Society (MRS) Graduate Student Award – Dec. 2003
- University of Pittsburgh Science Fair Award – Sept. 2001
- Wallace Prize for Outstanding Poster Presentation, Pittsburgh - Dec. 2000
- Student Honoree of the University of Pittsburgh – Feb. 2000
- Safford Award for Excellence as a Graduate Student Teacher – Aug. 1999

BIBLIOGRAPHY

1 S.A. Morton, J. Turton, and D. Greig, Rev. Sci Instrum. **66**, 3917 (1995).

2 C.G. Wiegenstein and K.H. Schulz, Rev. Sci Instrum. **68**, 1812 (1997).

3 L.J. Swartzendruber, F.H. Ulmer, and J.A. Coleman, Rev. Sci Instrum. **39** (12), 1858 (1968).

4 B.W. Pfalzgraf, H. Spreckels, and H. Muscher, Rev. Sci Instrum. **57** (5), 941 (1986).

5 H.W. Postma, T. Teepen, Z. Yao, M. Grifoni, and C. Dekker, Science **293**, 76 (2001).

6 R.B. Marcus and W.N. Carr, Microprobe - United States Patent 5475318 (1995).

7 S. Hasegawa and F. Grey, Surf. Sci. **500** (1-3), 84 (2002).

8 I. Shiraki, F. Tanabe, R. Hobara, T. Nagao, and S. Hasegawa, Surf. Sci. **493** (1-3), 633 (2001).

9 A.S. Khanna, *Introduction to high temperature oxidation and corrosion*. (ASM International, Materials Park, 2002).

10 N. Cabrera and N. F. Mott, Rep. Prog. Phys. **12**, 163-184 (1949).

11 M. W. Roberts and C. S. McKee, *Chemistry of the Metal-Gas Interface* (Oxford Univ. Press, Fair Lawn - NJ, 1979).

12 N. Cabrera and J. Hamon, C.R. Acad. Sci. **224**, 1713 (1947).

13 N. Cabrera, J. Terrien, and J. Hamon, C.R. Acad. Sci. **224**, 1558 (1947).

14 Francis P. Fehlner and Nevill F. Mott, Oxid. Met. **2** (1), 59-99 (1970).

15 I.M. Ritchie and R.K. Tandon, Surf. Sci. **22**, 99 (1970).

16 G.L. Hunt and I.M. Ritchie, Surf. Sci. **30**, 475 (1972).

17 I. Popova, V. Zhukov, and J. T. Yates, Jr., Phys. Rev. Lett. **89** (27), 276101-276104 (2002).

18 B. Voitglander, Surf. Sci. Rep. **43**, 127-254 (2001).

19 E. Bauer, Z. Kristallogr. **110**, 372 (1958).

20 J.A. Venables, G.D.T. Spiller, and M. Hanbucken, Rep. Prog. Phys. **47**, 399 (1984).

21 M.A. Herman and H. Sitter, *Molecular Beam Epitaxy - Fundamentals and Current Status*. (Springer, Berlin, 1996).

22 H. Luth, *Surface and Interfaces of Solids*. (Springer, Berlin, 1993).

23 F.C. Frank and J.H. van der Merwe, Proc. Roy. Soc. London A **198**, 205 (1949).

24 *The Chemical Physics of Solid Surfaces, Vol. 8 Growth and Properties of Ultrathin Epitaxial Layers*. (Elsevier Science, B.V., Amsterdam, 1997).

25 M. Volmer and A. Weber, Z. Phys. Chem. **119**, 277 (1926).

26 J.A. Venables and G.I. Price, *Epitaxial Growth - Part A*. (Academic Press, New York, 1975).

27 I.N. Stranski and L. Krastanow, Akad. Wiss. Lit. Mainz Math.-Natur. Kl. **146**, 797 (1938).

28 J.W. Orton and C.T. Foxon, Rep. Prog. Phys. **61**, 1 (1998).

29 S. Strite and H. Morkoc, J. Vac. Sci. Technol. B **10**, 1237 (1992).

30 D. Leonard, M. Krishnamurty, C.M. Reaves, S.P. Denbaar, and P. M. Petroff, Appl. Phys. Lett. **63**, 3203 (1993).

31 J.M. Moison, F. Houzay, F. Barthe, L. Leprince, E. Andre, and O. Vatel, Appl. Phys. Lett. **64**, 196 (1994).

[32] L. Goldstein, F. Glas, J.Y. Marzin, M.N. Charasse, and G. Le Roux, Appl. Phys. Lett. **47**, 1099 (1985).
[33] M. Strassburg, V. Kutzer, U. W. Pohl, A. Hoffmann, I. Broser, N. N. Ledentsov, D. Bimberg, A. Rosenauer, U. Fischer, D. Gerthsen, I. L. Krestnikov, M. V. Maximov, P. S. Kop'ev, and Zh I. Alferov, Appl. Phys. Lett. **72** (8), 942-944 (1998).
[34] F. Flack, N. Samarth, V. Nikitin, P. A. Crowell, J. Shi, J. Levy, and D. D. Awschalom, Phys. Rev. B **54** (24), R17 312-R317 315 (1996).
[35] S. H. Xin, P. D. Wang, Aie Yin, C. Kim, M. Dobrowolska, J. L. Merz, and J. K. Furdyna, Appl. Phys. Lett. **69** (25), 3884-3886 (1996).
[36] K. Brunner, Rep. Prog. Phys. **65** (1), 27-72 (2002).
[37] I. Berbezier, A. Ronda, and A. Portavoce, J. Phys. **14** (35), 8283-8331 (2002).
[38] V. A. Egorov, G. E. Cirlin, A. A. Tonkikh, V. G. Talalaev, A. G. Makarov, N. N. Ledentsov, V. M. Ustinov, N. D. Zakharov, and P. Werner, Phys. Sol. State **46** (1), 49-55 (2004).
[39] R. S. Williams, G. Medeiros-Ribeiro, T. I. Kamins, and D. A. A. Ohlberg, Ann. Rev. Phys. Chem. **51**, 527 (2000).
[40] J. Drucker, IEEE J. Quant. Elec. **38** (8), 975-987 (2002).
[41] V. Le Thanh, Surf. Sci. **492** (3), 255-269 (2001).
[42] O. P. Pchelyakov, Y. B. Bolkhovityanov, A. V. Dvurechenskii, L. V. Sokolov, A. I. Nikiforov, A. I. Yakimov, and B. Voigtlander, Semiconductors **34** (11), 1229-1247 (2000).
[43] O. P. Pchelyakov, Y. B. Bolkhovityanova, A. V. Dvurechenskii, A. I. Nikiforov, A. I. Yakimov, and B. Voigtlander, Thin Solid Films **367** (1-2), 75-84 (2000).
[44] F. Patella, A. Sgarlata, F. Arciprete, S. Nufris, P. D. Szkutnik, E. Placidi, M. Fanfoni, N. Motta, and A. Balzarotti, J. Phys. **16** (17), S1503-S1534 (2004).
[45] F. Wu and M. G. Lagally, Phys. Rev. Lett. **75** (2534) (1992).
[46] K. Iwawaki, M. Tomitori, and O. Nishikawa, Ultramicroscopy **42-44**, 832 (1992).
[47] M. Tomitori, K. Watanabe, M. Kobayashi, and O. Nishikawa, Appl. Surf. Sci. **76** (1-4), 322-328 (1994).
[48] I. Goldfarb and G. A. D. Briggs, Surf. Sci. **435**, 449-454 (1999).
[49] X. R. Qin and M. G. Lagally, Science **278** (5342), 1444-1447 (1997).
[50] K. Iwawaki, M. Tomitori, and O. Nishikawa, Surf. Sci. Lett. **253**, L411 (1991).
[51] V. Cimalla and K. Zekentes, Appl. Phys. Lett. **77** (10), 1452-1454 (2000).
[52] H. J. Kim and Y. H. Xie, Appl. Phys. Lett. **79** (2), 263-265 (2001).
[53] T. Suzuki, J. Levy, and J.T. Yates, Jr., unpublished (2005).
[54] Y.-W. Mo, D.E. Savage, B.S. Swartzentruber, and M. G. Lagally, Phys. Rev. Lett. **65** (8), 1020 (1990).
[55] D.J. Eaglesham and M. Cerullo, Phys. Rev. Lett. **64**, 1943 (1990).
[56] B. Gallas, I. Berbezier, A. Ronda, and J. Derrien, Thin Solid Films **294** (1-2), 22-26 (1997).
[57] I. Davoli, R. Gunnella, P. Castrucci, N. Pinto, R. Bernardini, and M. DeCrescenzi, Appl. Surf. Sci. **102**, 102-106 (1996).
[58] L. DiGaspare, G. Capellini, M. Sebastiani, C. Chudoba, and F. Evangelisti, Appl. Surf. Sci. **102**, 94-97 (1996).
[59] E. Palange, G. Capellini, L. DiGaspare, and F. Evangelisti, Appl. Phys. Lett. **68** (21), 2982-2984 (1996).

[60] A. J. Steinfort, Pmlo Scholte, A. Ettema, F. Tuinstra, M. Nielsen, E. Landemark, D. M. Smilgies, R. Feidenhansl, G. Falkenberg, L. Seehofer, and R. L. Johnson, Phys. Rev. Lett. **77** (10), 2009-2012 (1996).
[61] J. Tersoff, C. Teichert, and M. G. Lagally, Phys. Rev. Lett. **76** (10), 1675-1678 (1996).
[62] T. I. Kamins and R. S. Williams, Surf. Sci. **405** (2-3), L580-L586 (1998).
[63] J. Y. Kim and J. H. Seok, Mat. Sci. Eng. B **89** (1-3), 176-179 (2002).
[64] J. Tersoff and F.K. LeGoues, Phys. Rev. Lett. **72** (22), 3570 (1994).
[65] V. Le Thanh, P. Boucaud, D. Debarre, Y. Zheng, D. Bouchier, and J. M. Lourtioz, phys. Rev. B **58** (19), 13115-13120 (1998).
[66] X. Wang, Z. M. Jiang, H. J. Zhu, F. Lu, D. M. Huang, X. H. Liu, C. W. Hu, Y. F. Chen, Z. Q. Zhu, and T. Yao, Appl. Phys. Lett. **71** (24), 3543-3545 (1997).
[67] V. A. Markov, H. H. Cheng, C. T. Chia, A. I. Nikiforov, V. A. Cherepanov, O. P. Pchelyakov, K. S. Zhuravlev, A. B. Talochkin, E. McGlynn, and M. O. Henry, Thin Solid Films **369** (1-2), 79-83 (2000).
[68] V. Yam, V. Le Thanh, U. Compagnon, U. Gennser, P. Boucaud, D. Debarre, and D. Bouchier, Thin Solid Films **380** (1-2), 78-81 (2000).
[69] V. Yam, V. Le Thanh, Y. Zheng, P. Boucaud, and D. Bouchier, Phys. Rev. B **63** (3), 033313 (2001).
[70] G. Medeiros-Ribeiro, A. M. Bratkovski, T. I. Kamins, D. A. A. Ohlberg, and R. S. Williams, Science **279**, 353 (1998).
[71] A. Rastelli and H. von Kanel, Surf. Sci. **515** (2-3), L493-L498 (2002).
[72] A. Vailionis, B. Cho, G. Glass, P. Desjardins, D. G. Cahill, and J. E. Greene, Phys. Rev. Lett. **85** (17), 3672-3675 (2000).
[73] E. Palange, L. Ragni, L. Di Gaspare, G. Capellini, and F. Evangelisti, J. Appl. Phys. **83** (11), 5840-5844 (1998).
[74] Z. M. Jiang, H. J. Zhu, F. Lu, J. Qin, D. M. Huang, X. Wang, C. W. Hu, Y. F. Chen, Z. Q. Zhu, and T. Yao, Thin Solid Films **321**, 60-64 (1998).
[75] G. Medeiros-Ribeiro, T. I. Kamins, D. A. A. Ohlberg, and R. S. Williams, phys. Rev. B **58** (7), 3533-3536 (1998).
[76] C. Schollhorn, M. Oehme, M. Bauer, and E. Kasper, Thin Solid Films **336** (1-2), 109-111 (1998).
[77] U. Denker, O. G. Schmidt, N.Y. Jin-Phillipp, and K. Eberl, Appl. Phys. Lett. **78** (23), 3723 (2001).
[78] M. Schleberger, A. C. Simonsen, S. Tougaard, J. L. Hansen, and A. N. Larsen, J. Vac. Sci. Technol. A **15** (6), 3032-3035 (1997).
[79] P. Schittenhelm, G. Abstreiter, A. Darhuber, G. Bauer, P. Werner, and A. Kosogov, Thin Solid Films **294** (1-2), 291-295 (1997).
[80] A. C. Simonsen, S. Tougaard, J. L. Hansen, and A. N. Larsen, Surf. and Interf. Anal. **31** (4), 328-337 (2001).
[81] G. Capellini, M. De Seta, and F. Evangelisti, Mat. Sci. Eng. B **89** (1-3), 184-187 (2002).
[82] B. Liu, C. L. Berrie, T. Kitajima, J. Bright, and S. R. Leone, J. vac. Sci. & Technol. B **20** (2), 678-684 (2002).
[83] F. M. Ross, R. M. Tromp, and M. C. Reuter, Science **286** (5446), 1931-1934 (1999).
[84] G. Wohl, C. Schollhorn, O. G. Schmidt, K. Brunner, K. Eberl, O. Kienzle, and F. Ernst, Thin Solid Films **321**, 86-91 (1998).

[85] A. C. Simonsen, M. Schleberger, S. Tougaard, J. L. Hansen, and A. N. Larsen, Thin Solid Films **338** (1-2), 165-171 (1999).
[86] A. Dunbar, U. Bangert, P. Dawson, M. Halsall, Y. Shiraki, M. Miura, I. Berbezier, B. A. Joyce, and J. Zhang, Phys. Stat. Sol. B **224** (1), 265-269 (2001).
[87] S. Chaparro, J. Drucker, Y. Zhang, D. Chandrasekhar, M.R. McCartney, and C.G. Smith, Phys. Rev. Lett. **83** (6), 1199 (1999).
[88] F. M. Ross, J. Tersoff, and R. M. Tromp, Phys. Rev. Lett. **80** (5), 984-987 (1998).
[89] A. A. Darhuber, J. Stangl, G. Bauer, P. Schittenhelm, and G. Abstreiter, Thin Solid Films **294** (1-2), 296-299 (1997).
[90] K. Sumitomo, K. Shiraishi, Y. Kobayashi, T. Ito, and T. Ogino, Thin Solid Films **369** (1-2), 112-115 (2000).
[91] O. Guise, unpublished.
[92] O.G. Schmidt, C. Lange, K. Eberl, O. Kienzle, and F. Ernst, Thin Solid Films **321**, 70 (1998).
[93] O. G. Schmidt, C. Lange, K. Eberl, O. Kienzle, and F. Ernst, Appl. Phys. Lett. **71** (16), 2340-2342 (1997).
[94] O. G. Schmidt, C. Lange, K. Eberl, O. Kienzle, and F. Ernst, Thin Solid Films **336** (1-2), 248-251 (1998).
[95] O. Leifeld, PhD Thesis - Ecole Polytechnique Federale de Lausanne, 2002.
[96] P. C. Kelires and E. Kaxiras, Phys. Rev. Lett. **78** (18), 3479 (1998).
[97] O. Leifeld, D. Grutzmacher, B. Muller, K. Kern, E. Kaxiras, and P. C. Kelires, Phys. Rev. Lett. **82** (5), 972 (1999).
[98] O. Leifeld, R. Hartmann, E. Muller, E. Kaxiras, K. Kern, and D. Grutzmacher, Nanotechnology **10** (2), 122-126 (1999).
[99] O. Leifeld, A. Beyer, E. Muller, K. Kern, and D. Grutzmacher, Mat. Sci. Eng. B **74** (1-3), 222-228 (2000).
[100] O. Leifeld, A. Beyer, E. Muller, D. Grutzmacher, and K. Kern, Thin Solid Films **380** (1-2), 176-179 (2000).
[101] O. G. Schmidt and K. Eberl, Semicond. Sci. Technol. **15** (4), 399-402 (2000).
[102] K. Eberl, O. G. Schmidt, O. Kienzle, and F. Ernst, Thin Solid Films **373** (1-2), 164-169 (2000).
[103] J. Y. Kim, S. H. Ihm, J. H. Seok, C. H. Lee, Y. H. Lee, E. K. Suh, and H. J. Lee, Thin Solid Films **369** (1-2), 96-99 (2000).
[104] A. Beyer, E. Muller, H. Sigg, S. Stutz, D. Grutzmacher, O. Leifeld, and K. Ensslin, Appl. Phys. Lett. **77** (20), 3218-3220 (2000).
[105] A. Beyer, O. Leifeld, E. Muller, S. Stutz, H. Sigg, and D. Grutzmacher, Thin Solid Films **380** (1-2), 246-248 (2000).
[106] A. Beyer, O. Leifeld, S. Stutz, E. Muller, and D. Grutzmacher, Nanotechnology **11** (4), 298-304 (2000).
[107] M. Stoffel, L. Simon, J. L. Bischoff, D. Aubel, L. Kubler, and G. Castelein, Thin Solid Films **380** (1-2), 32-35 (2000).
[108] J. Stangl, V. Holy, P. Mikulik, G. Bauer, I. Kegel, T. H. Metzger, O. G. Schmidt, C. Lange, and K. Eberl, Appl. Phys. Lett. **74** (25), 3785-3787 (1999).
[109] S. J. Tans, A. R. M. Verschueren, and C. Dekker, Nature **393** (6680), 49-52 (1998).
[110] M. Field, C. G. Smith, M. Pepper, D. A. Ritchie, J. E. F. Frost, G. A. C. Jones, and D. G. Hasko, Phys. Rev. Lett. **70** (9), 1311-1314 (1993).

[111] R. J. Schoelkopf, P. Wahlgren, A. A. Kozhevnikov, P. Delsing, and D. E. Prober, Science **280** (5367), 1238-1242 (1998).
[112] R. Vrijen, E. Yablonovitch, K. Wang, H. W. Jiang, A. Balandin, V. Roychowdhury, T. Mor, and D. DiVincenzo, Phys. Rev. A **62** (1), 012306 (2000).
[113] J. Levy, Phys. Rev. A **64**, 52306 (2001).
[114] M. Friesen, P. Rugheimer, D. E. Savage, M. G. Lagally, D. W. van der Weide, R. Joynt, and M. A. Eriksson, Phys. Rev. B **67** (12), 121301 (2003).
[115] C. S. Lent, P. D. Tougaw, and W. Porod, Appl. Phys. Lett. **62** (7), 714-716 (1993).
[116] R.S. Service, Science **271**, 920 (1996).
[117] D. S. L. Mui, D. Leonard, L. A. Coldren, and P. M. Petroff, Appl. Phys. Lett. **66** (13), 1620-1622 (1995).
[118] T. I. Kamins and R. S. Williams, Appl. Phys. Lett. **71** (9), 1201-1203 (1997).
[119] T. I. Kamins, R. S. Williams, and D. P. Basile, Nanotechnology **10** (2), 117-121 (1999).
[120] L. Vescan, T. Stoica, and B. Hollander, Mat. Sci. Eng. B **89** (1-3), 49-53 (2002).
[121] L. Vescan, K. Grimm, M. Goryll, and B. Hollander, Mat. Sci. Eng. B **69-70**, 324 (2000).
[122] G. Jin, J. L. Liu, S. G. Thomas, Y. H. Luo, K. L. Wang, and B. Y. Nguyen, Appl. Phys. A **70** (5), 551-554 (2000).
[123] G. Jin, J. L. Liu, Y. H. Luo, and K. L. Wang, Thin Solid Films **369** (1-2), 49-54 (2000).
[124] T. Kitajima, B. Liu, and S. R. Leone, Appl. Phys. Lett. **80** (3), 497-499 (2002).
[125] G. Jin, J. L. Liu, Y. H. Luo, and K. L. Wang, Thin Solid Films **380** (1-2), 169-172 (2000).
[126] K. Sakamoto, H. Matsuhata, M. O. Tanner, D. W. Wang, and K. L. Wang, Thin Solid Films **321**, 55-59 (1998).
[127] M. Kasu and N. Kobayashi, Appl. Phys. Lett. **62**, 1262 (1993).
[128] M. Kitamura, M. Nishioka, J. Oshinowo, and Y. Arakawa, Appl. Phys. Lett. **66** (26), 3663-3665 (1995).
[129] K. Brunner, J. Zhu, G. Abstreiter, O. Kienzle, and F. Ernst, Phys. Stat. Sol. B **224** (2), 531-535 (2001).
[130] J. Stangl, T. Roch, V. Holy, M. Pinczolits, G. Springholz, G. Bauer, I. Kegel, T. H. Metzger, J. Zhu, K. Brunner, G. Abstreiter, and D. Smilgies, J. Vac. Sci. & Technol. B **18** (4), 2187-2192 (2000).
[131] A. Ronda and I. Berbezier, Phys. E **23** (3-4), 370-376 (2004).
[132] I. Berbezier, M. Abdallah, A. Ronda, and G. Bremond, Mat. Sci. Eng. B **69**, 367-373 (2000).
[133] J. H. Zhu, K. Brunner, and G. Abstreiter, Appl. Phys. Lett. **73** (5), 620-622 (1998).
[134] S. Y. Shiryaev, F. Jensen, J. W. Petersen, J. L. Hansen, and A. N. Larsen, J. Crystal Growth **157** (1-4), 132-136 (1995).
[135] S. Y. Shiryaev, E. V. Pedersen, F. Jensen, J. W. Petersen, J. L. Hansen, and A. N. Larsen, Thin Solid Films **294** (1-2), 311-314 (1997).
[136] Y. H. Xie, S. B. Samavedam, M. Bulsara, T. A. Langdo, and E. A. Fitzgerald, Appl. Phys. Lett. **71** (24), 3567-3568 (1997).
[137] E. A. Fitzgerald, Y. H. Xie, D. Monroe, P.J. Silverman, J.M. Kuo, A.R. Kortan, F.A. Thiel, and B.E. Weir, J. Vac. Sci. & Technol. B **10**, 1807 (1992).
[138] C. Lee and A. L. Barabasi, Appl. Phys. Lett. **73** (18), 2651-2653 (1998).
[139] L. H. Nguyen, V. Le Thanh, V. Yam, D. Debarre, M. Halbwax, and D. Bouchier, Phys. Stat. Sol. A **201** (2), 353-356 (2004).

[140] E. S. Kim, N. Usami, and Y. Shiraki, Appl. Phys. Lett. **72** (13), 1617-1619 (1998).
[141] L. H. Nguyen, V. LeThanh, D. Debarre, V. Yam, M. Halbwax, M. El Kurdi, D. Bouchier, P. Rosner, M. Becker, M. Benamara, and H. P. Strunk, Appl. Surf. Sci. **224** (1-4), 134-138 (2004).
[142] L. Vescan, T. Stoica, B. Hollander, A. Nassiopoulou, A. Olzierski, I. Raptis, and E. Sutter, Appl. Phys. Lett. **82** (20), 3517-3519 (2003).
[143] M. Kammler, R. Hull, M. C. Reuter, and F. M. Ross, Appl. Phys. Lett. **82** (7), 1093-1095 (2003).
[144] A. Karmous, A. Cuenat, A. Ronda, I. Berbezier, S. Atha, and R. Hull, Appl. Phys. Lett. **85** (26), 6401 (2004).
[145] R.J. Culbertson and S.J. Pennycook, Nucl. Instrum. Methods Phys. Res. B **13**, 490 (1986).
[146] S. Maruno, S. Fujita, H. Watanabe, Y. Kusumi, and M. Ichikawa, J. Appl. Phys. **83**, 205 (1998).
[147] Y. Nitta, M. Shibata, K. Fujita, and M. Ichikawa, Surf. Sci. **431**, L565 (1999).
[148] Z. Y. Zhong, A. Halilovic, M. Muhlberger, F. Schaffler, and G. Bauer, Appl. Phys. Lett. **82** (3), 445-447 (2003).
[149] Z. Y. Zhong, A. Halilovic, M. Muhlberger, F. Schaffler, and G. Bauer, J. Appl. Phys. **93** (10), 6258-6264 (2003).
[150] T. I. Kamins, D. A. A. Ohlberg, R. S. Williams, W. Zhang, and S. Y. Chou, Appl. Phys. Lett. **74** (12), 1773-1775 (1999).
[151] L.J. Van der Pauw, Philips Res. Rep. **13**, 1 (1958).
[152] H.C. Montgomery, J. Appl. Phys. **42**, 2971 (1971).
[153] S. Tsukamoto, B. Siu, and N. Nakagiri, Rev. Sci Instrum. **62** (7), 1767 (1991).
[154] J. M. Byers and M. E. Flatte, Phys. Rev. Lett. **74** (2), 306 (1995).
[155] H. Grube, B. C. Harrison, J. F. Jia, and J. J. Boland, Rev. Sci Instrum. **72** (12), 4388 (2001).
[156] Q. Niu, M. C. Chang, and C. K. Shih, Phys. Rev. B **51** (8), 5502 (1995).
[157] S. Hasegawa, I. Shiraki, F. Tanabe, and R. Hobara, Cur. Appl. Phys. **2** (6), 465 (2002).
[158] S. Hasegawa, N. Sato, I. Shiraki, C. L. Petersen, P. Boggild, T. M. Hansen, T. Nagao, and F. Grey, Jap. J. Appl. Phys. **39** (6B), 3815 (2000).
[159] T. M. Hansen, K. Stokbro, O. Hansen, T. Hassenkam, I. Shiraki, S. Hasegawa, and P. Boggild, Rev. Sci Instrum. **74** (8), 3701 (2003).
[160] C. L. Petersen, F. Grey, I. Shiraki, and S. Hasegawa, Appl. Phys. Lett. **77** (23), 3782 (2000).
[161] C. L. Petersen, T. M. Hansen, P. Boggild, A. Boisen, O. Hansen, T. Hassenkam, and F. Grey, Sensors and Actuators A **96** (1), 53 (2002).
[162] S. Hasegawa, I. Shiraki, T. Tanikawa, C. L. Petersen, T. M. Hansen, P. Boggild, and F. Grey, J. Phys. - Cond. Matt. **14** (35), 8379 (2002).
[163] H. Nishino, W. Yang, Z. Dohnalek, V. A. Ukraintsev, W. J. Choyke, and J. T. Yates, Jr., J. Vac. Sci. Technol. A **15** (1), 182 (1997).
[164] J. T. Yates, Jr., *Experimental Innovations in Surface Science*. (Springer-Verlag-AIP, New York, NY, 1997), pp.508-511.
[165] www.nanotechnik.com.
[166] S. Kleindiek, H. S. Kim, E. Kratschmer, and T. H. P. Chang, J. Vac. Sci. Technol. B **13** (6), 2653 (1995).

[167] S. Kleindiek and K. H. Herrmann, Rev. Sci Instrum. **64** (3), 692 (1993).
[168] H. Seiler, J. Appl. Phys. **54** (11), R1 (1983).
[169] Gibbs Wire and Steel Co Inc. -P.O. Box 520, Southington,CT 06489.
[170] D.C. Burkman, Semicond. Internat. **4** (7), 103-114 (1981).
[171] W. Kern, RCA Rev. **31**, 207-233 (1970).
[172] W. Kern, *Handbook of Semiconductor Wafer Cleaning Technology - Science, Technology and Applications*. (Noyes/William Andrew Publishing, 1993).
[173] S.C. Street and D.W. Goodman, *The Chemical Physics of Solid Surfaces, Volume 8: Growth and Properties of Ultrathin Epitaxial Layers*. (Elsevier, Amsterdam, 1997).
[174] J. C. Yang, B. Kolasa, J. M. Gibson, and M. Yeadon, Appl. Phys. Lett. **73** (19), 2841-2843 (1998).
[175] A. T. Fromhold, Jr., *Defects in Crystalline Solids, Vol. 9: Theory of Metal Oxidation, Vol. 1: Fundamentals*. (North Holland Publishing Co., Amsterdam, 1976).
[176] Hugh P. Godard, Walter B. Jepson, M. R. Bothewell, and Robert L. Kane, *The Corrosion of Light Metals*. (Wiley, New York, 1967).
[177] J. G. Ekerdt, Y. M. Sun, A. Szabo, G. J. Szulczewski, and J. M. White, Chem. Rev. **96** (4), 1499-1517 (1996).
[178] H.N. Waltenburg and J. T. Yates, Jr., Chem. Rev. **95**, 1589-1673 (1995).
[179] V. P. Zhdanov and P. R. Norton, Surf. Rev. Lett. **7** (1 & 2), 135-139 (2000).
[180] A. Atkinson, Rev. Mod. Phys. **57** (2), 437-470 (1985).
[181] H. Brune, J. Wintterlin, J. Trost, G. Ertl, J. Wiechers, and R. J. Behm, J. Chem. Phys. **99** (3), 2128-2148 (1993).
[182] J. Trost, H. Brune, J. Wintterlin, R. J. Behm, and G. Ertl, J. Chem. Phys. **108** (4), 1740-1747 (1998).
[183] I. Popova, V. Zhukov, and J. T. Yates, Jr., Langmuir **16** (26), 10309-10314 (2000).
[184] I. Popova, V. Zhukov, and J. T. Yates, Jr., J. Appl. Phys. **87** (11), 8143-8147 (2000).
[185] L. Osterlund, I. Zoric, and B. Kasemo, Phys. Rev. B **55** (23), 15452-15455 (1997).
[186] V. Zhukov, I. Popova, and J. T. Yates, Jr., Surf. Sci. **441** (2-3), 251-264 (1999).
[187] E. G. Keim, L. Wolterbeek, and A. Van Silfhout, Surf. Sci. **180** (2-3), 565-598 (1987).
[188] R. Chakarova, D. E. Oner, I. Zoric, and B. Kasemo, Surf. Sci. **472** (1-2), 63-79 (2001).
[189] L. Verdi, A. Miotello, and R. Kelly, Thin Solid Films **241**, 383-387 (1994).
[190] Y. Widjaja and C. Musgrave, J. Chem. Phys. **116** (13), 5774-5780 (2002).
[191] J. Westermann, H. Nienhaus, and W. Moench, Surf. Sci. **311** (1-2), 101-106 (1994).
[192] Albert T. Fromhold, Jr. and Earl L. Cook, III, Phys. Rev. **158** (3), 600-612 (1967).
[193] Carl Wagner and Karl Grunewald, Z. Physik. Chem. **B40**, 455-475 (1938).
[194] I. Popova, V. Zhukov, and J. T. Yates, Jr., Phys. Rev. Lett. **89** (27), 276101/276101-276101/276104 (2002).
[195] T. Do, S. J. Splinter, C. Chen, and N. S. McIntyre, Surf. Sci. **387** (1-3), 192-198 (1997).
[196] O. Guise, H. Marbach, M.-C. Jung, J. Levy, J. Ahner, and J. T. Yates, Jr., Rev. Sci. Instrum. Accepted for publication (2005).
[197] Quantitative considerations of the Hertzian contact between a hemispherical (~10nm radius) Pt/Ir tip and Al metal indicate that indentation will only be 10^{-3} or less of the bending displacement of an STM tip as gentle tip-surface contact is made at a 45º angle from the tunneling position. This assures that the observed low resistance contact during oxide film formation on Al(111) is not due to tip penetration into the solid.

[198] J. T. Yates, Jr., *Experimental Innovations in Surface Science*. (Springer-Verlag-AIP, New York, NY, 1997).
[199] K. Wefers and C. Misra, Alcoa Technical Paper **19** (1987).
[200] D. Gruetmacher, R. Hartmann, and O. Leifeld, Appl. Phys. Lett. **72**, 3344 (1998).
[201] C.S. Peng, Q. Huang, and W.Q. Cheng, Phys. Rev. B **57**, 8805 (1998).
[202] R. J. Hamers and Y. J. Wang, Chem Rev **96** (4), 1261-1290 (1996).
[203] C. C. Cheng, R. M. Wallace, P. A. Taylor, W. J. Choyke, and J. T. Yates, Jr., J. Appl. Phys. **67** (8), 3693 (1990).
[204] H. N. Waltenburg and J. T. Yates, Jr., Chem Rev **95** (5), 1589-1673 (1995).
[205] L. Clemen, R. M. Wallace, P. A. Taylor, M. J. Dresser, W. J. Choyke, W. H. Weinberg, and J. T. Yates, Jr., Surf. Sci. **268** (1-3), 205-216 (1992).
[206] J. Yoshinobu, H. Tsuda, M. Onchi, and M. Nishijima, J. Chem. Phys. **87** (12), 7332 (1987).
[207] Y. Bu, L. Ma, and M. C. Lin, J. Phys. Chem. **97** (45), 11797-11801 (1993).
[208] M. Toscano, Surf. Sci. **251-252**, 894 (1991).
[209] B. I. Craig and P. V. Smith, Surf. Sci. **276** (1-3), 174-183 (1992).
[210] C. C. Cheng, P. A. Taylor, R. M. Wallace, H. Gutleben, L. Clemen, M. L. Colianni, P. J. Chen, W. H. Weinberg, W. J. Choyke, and J. T. Yates, Jr., Thin Solid Films **225** (1-2), 196-202 (1993).
[211] S. Matsui, T. Ichihashi, and M. Mito, J. Vac. Sci. Technol. B **7** (5), 1182-1190 (1989).
[212] H.W.P. Koops, R. Weiel, D.P. Kern, and T.H. Baum, J. Vac. Sci. Technol. B **6** (1), 477-481 (1988).
[213] K.L. Lee and M. Hatzakis, J. Vac. Sci. Technol. B **7** (6), 1941-1946 (1989).
[214] C. Bater, M. Sanders, and J. H. Craig, Surf. and Interf. Anal. **29** (3), 188-193 (2000).
[215] F. Bozso and Ph. Avouris, Phys. Rev. B **38** (6), 3943 (1988).
[216] M.-L. Shek, S.P. Withrow, and W. H. Weinberg, Surf. Sci. **72**, 678 (1978).
[217] R.D. Ramsier and J. T. Yates, Jr., Surf. Sci. Rep. **12** (6-8), 243-378 (1991).
[218] B.A. Joyce and J.H. Neave, Surf. Sci. **34**, 401 (1973).
[219] C. Klauber, M.D. Alvey, and J. T. Yates, Jr., Surf. Sci. **154**, 139-167 (1985).
[220] H.H. Madden, J. Vac. Sci. Technol. **18** (3), 677-689 (1981).
[221] C. Scheuerlein and M. Taborelli, J. Vac. Sci. Technol. A **20** (1), 93-101 (2002).
[222] W. Kern and D. Puotinen, RCA Rev. **31**, 87-206 (1970).
[223] L.E. Davis, *Handbook of Auger Electron Spectroscopy, 3rd edition*. (Springer-Verlag, Newark, NJ, 1985).
[224] F. Bozso, W. J. Choyke, L. Muehlhoff, and J. T. Yates, Jr., J. Appl. Phys. **57** (8), 2771 (1985).
[225] I. Kusunoki and Y. Igari, Appl. Surf. Sci. **59**, 95-104 (1992).
[226] O. Guise, J. Ahner, J. T. Yates, Jr., and J. Levy, Appl. Phys. Lett. **85** (12), 2352 (2004).
[227] J. Z. Xu, W. J. Choyke, and J. T. Yates, Jr., Appl. Surf. Sci. **120** (3-4), 279-286 (1997).
[228] T. Fuller and F. Banhart, Chem. Phys. Lett. **254** (5-6), 372-378 (1996).
[229] A. Nagase, S. Horiguchi, A. Fujiwara, Y. Ono, K. Yamazaki, H. Namatsu, and Y. Takahashi, Appl. Surf. Sci. **190** (1-4), 144-150 (2002).
[230] M. Nagase, S. Horiguchi, A. Fujiwara, and Y. Takahashi, Jap. J. Appl. Phys. **42** (4B), 2438-2443 (2003).
[231] R.P. Andres, T. Bein, M. Dorogi, S. Feng, J.I. Henderson, C.P. Kubiak, W. Mahoney, R.G. Osifchin, and R. Reifenberger, Science **272**, 1323 (1996).

[232] T. C. Shen, C. Wang, G. C. Abeln, J. R. Tucker, J. W. Lyding, P. Avouris, and R. E. Walkup, Science **268** (5217), 1590-1592 (1995).
[233] R. Bennewitz, J. N. Crain, A. Kirakosian, J. L. Lin, J. L. McChesney, D. Y. Petrovykh, and F. J. Himpsel, Nanotechnology **13** (4), 499-502 (2002).
[234] A.N. Broers, W.W. Molzen, J.J. Cuomo, and N.D. Wittels, Appl. Phys. Lett. **29** (9), 596 (1976).
[235] A.N. Broers, Journal of Vac. Sci. & Technol. **8** (5), 50 (1971).
[236] T. Djenizian, L. Santinacci, and P. Schmuki, Appl. Phys. Lett. **78** (19), 2940-2942 (2001).
[237] N. Miura, H. Ishii, J. Shirakashi, A. Yamada, and M. Konagai, Appl. Surf. Sci. **113/114**, 269-273 (1997).
[238] N. Miura, A. Yamada, and M. Konagai, Jap. J. Appl. Phys. **36** (9AB), L1275-L1278 (1997).
[239] J.R. Vig, J. Vac. Sci. Technol. A **3**, 1027 (1985).
[240] O. Guise, H. Marbach, J. Levy, J. Ahner, and J.T. Yates Jr., Surf. Sci. **571**, 128-138 (2004).
[241] P. C. Kelires and E. Kaxiras, J. Vac. Sci. & Technol. B **16** (3), 1687-1691 (1998).
[242] Meikei Ieong, Bruce Doris, Jakub Kedzierski, Ken Rim, and Min Yang, Science **306** (5704), 2047-2060 (2004).
[243] L. Guo, E. Leobandung, and S. Y. Chou, Science **275**, 649 (1997).
[244] P. W. Li, W. M. Liao, D. M. T. Kuo, S. W. Lin, P. S. Chen, S. C. Lu, and M. J. Tsai, Appl. Phys. Lett. **85** (9), 1532-1534 (2004).
[245] S. Y. Huang, S. Banerjee, R. T. Tung, and S. Oda, J. Appl. Phys. **94** (11), 7261-7265 (2003).
[246] B. E. Kane, Nature **393** (6681), 133-137 (1998).
[247] T. D. Ladd, J. R. Goldman, F. Yamaguchi, Y. Yamamoto, E. Abe, and K. M. Itoh, Phys. Rev. Lett. **89** (1) (2002).
[248] J. Drucker and S. Chaparro, Appl. Phys. Lett. **71** (5), 614-616 (1997).
[249] Y. Suda, S. Kaechi, D. Kitayama, and T. Yoshizawa, Thin Solid Films **464-65**, 190 (2004).
[250] D.R. Lide, *CRC Handbook of Chemistry and Physics - 84th Edition*. (CRC Press, Boca Raton, 2003).
[251] L. Anwei, H. Xiaotang, L. Wenhui, and J. Guijun, Rev. Sci. Instrum. **68**, 3811 (1997).
[252] H. Bourque and R.M. Leblanc, Rev. Sci. Instrum. **66**, 2695 (1995).
[253] M. Klein and G. Schwitzgebel, Rev. Sci. Instrum. **68**, 3099 (1997).
[254] J. Méndez, M. Luna, and A.M. Baró, Surf. Sci. **266**, 294 (1992).
[255] A.-D. Müller, F. Müller, M. Hietschold, F. Demming, J. Jersch, and K. Dickmann, Rev. Sci. Instrum. **70**, 3970 (1999).
[256] J. Nakamura, Y. Mera, and K. Maeda, Rev. Sci. Instrum. **70**, 3373 (1999).
[257] A.I. Oliva, A. Romero, J.L. Peña, E. Anguiano, and M. Aguilar, Rev. Sci. Instrum. **67**, 1917 (1996).
[258] C. Chen, *Introduction to Scanning Tunneling Microscopy*. (Oxford University Press, New York, 1993).
[259] V.S. Fomenko, *Handbook of Thermionic Properties - Electronic Work Functions and Richardson Constants of Elements and Compounds*. (Plenum Press, New York, 1966).
[260] G. Sauerbrey, Zeitschrift fűr Physik **155**, 206-222 (1959).

[261] H. Hertz, Zeitschrift fűr die Reine und Angewandte Mathematik **92**, 156-171 (1881).